# On the Generation of Lift Force in Random, Soft Porous Media; Its Application to An Airborne Jet Train

by

**Parisa Mirbod**

Dissertation submitted to the Faculty in Engineering in partial fulfillment of the

requirements for the degree of Doctor of Philosophy,

The City University of New York

2010

This manuscript has been read and accepted for the
Graduate Faculty in Engineering in satisfaction of the
dissertation requirement for the degree of Doctor of Philosophy.

| | |
|---|---|
| | Prof. Sheldon Weinbaum |
| Date | Chair of Examining Committee |
| | Prof. Mumtaz Kassir |
| Date | Executive Officer |

Prof. Yiannis Andreopoulos, Co-Advisor

Prof. Howard Stone, Supervision Committee 1

Prof. Latif M. Jiji, Supervision Committee 2

Prof. Peter Ganatos, Supervision Committee 3

Supervision Committee

THE CITY UNIVERSITY OF NEW YORK

# Abstract

ON THE GENERATION OF LIFT FORCE IN RANDOM, SOFT POROUS MEDIA; ITS APPLICATION TO AN AIRBORNE JET TRAIN

by

Parisa Mirbod

Mentor: Professor Sheldon Weinbaum,

Co-mentor: Professor Yiannis Andreopoulos

Feng and Weinbaum (2000) developed a theory which demonstrated that highly compressible soft porous materials could transiently support very large loads beneath a planing surface for short duration if the trapped fluid within the fibrous medium could not escape on the time scale of the passage of the planing surface. They also showed that there is a remarkable hydrodynamic similarity between the motion of the red blood cells and a human skier or snowboarder skiing on soft snow powder even though they differ in mass by $10^{15}$. Thus, the lift forces in each case can be four or more orders of magnitude greater than classical lubrication theory. In more recent papers, Wu et al. (2005) utilizes a porous cylinder apparatus to measure for the first time the dynamic pressures that develop on the time scale of skiing or snowboarding. Using this novel apparatus, Wu et al. (2006) predicted that fully 50 percent of the total lift on a snowboard traveling at 10 m/s arose from the excess pore pressure that developed due to the transiently trapped air beneath the snowboard and the increased hydraulic resistance of the compressed snow.

In this dissertation, the generalized Reynolds equation derived in Feng and Weinbaum (2000) to random porous media is extended using the Carman-Kozeny equation for a random fiber array. This extended analysis is then applied to planning surfaces moving in a channel in which the loss of pressure at the lateral edges is eliminated by using impermeable sidewalls. We show that dramatically different behavior is obtained depending on whether the porous medium is attached to a stationary horizontal lower boundary or to a moving inclined upper boundary. We then explore the quantitative feasibility, performance and stability of an airborne jet train (AJT) that flies on a soft porous track within centimeters of the earth's surface. We first show that it is possible to support a 70 metric ton jet train carrying 200 passengers on a confined porous material if its Kp is approximately $5x10^{-9}$ $m^2$. Using random porous media theory, we predict that one can achieve lift-off at only 5 m/s if the porous material has a fiber radius of 5μm and a solid fraction of 0.005. Furthermore, we predict that by using jet engines of 10,000 lbf thrust, about 1/5 that of a jet aircraft, one can accelerate to a cruising velocity of 700 km/hr in less than 2 minutes. Since energy expenditure is thrust times distance, fuel consumption should be less than 1/5 that of commercial jets. In addition, combustion products are not released high in the atmosphere where global warming effects are greatest.

# Dedication

*To my parents, my husband, and all others who believe in curiosity, patience, and a desire to learn*

# Acknowledgements

Most of all I would like to express my sincere gratitude to my advisors Prof. Sheldon Weinbaum and Professor Yiannis Andreopoulos for their continuous support, suggestions and encouragement. It was a privilege for me to study and do my research in their care.

I would like to thank Professor Weinbaum for his valuable guidance and his warm support during my graduate studies. I sincerely appreciate his patience, understanding and encouragement. He has been an excellent mentor and role model which will forever inspire me to do good quality work.

I am especially thankful to Prof. Yiannis Andreopoulos for his excellent advice and guidance during my research and graduate studies. I am grateful to him for his goodwill, care and support toward me and my family and his patience in listening to my problems.

I especially want to thank my advisors for training me comprehensively not only in research but also in other crucial aspects of academic activities such as writing, proposal preparation and teaching.

I would like to thank Prof. Latif M. Jiji who has often advised me kindly and helped me in my research and career. I enjoyed his classes as well as collaborating with him in research.

I would like to thank Prof. Peter Ganatos for his help in my research and his valuable comments.

I would like to acknowledge Professor Feridun Delale, Professor Taehun Lee and Professor Masahiro Kawaji, who have advised me in my career on several occasions.

Furthermore, I should acknowledge great efforts of the entire Ph.D. examining committee: Professor Latif M. Jiji, Professor Peter Ganatos and Professor Howard A. Stone for their review of this thesis, discussions, and constructive comments.

Financial support from the National Science Foundation, NSF Grant CTS #0432229 is acknowledged.

I would like to extend my appreciation to all my friends in Iran, New York City and The City College of New York with whom I shared great memories.

I am especially willing to pay tribute to the brave Iranian “Green” protesters who have taken to the dangerous streets of Iran and who fight for their rights and freedom.

My special thanks go to my husband Mohammad Hossein Azadfar who has been a great support and lifeline over the years. I thank him for all his patience, support and confidence in me during my graduate study.

I cannot end without thanking my lovely family, my mother Zahra Tavousi, father Mehdi Mirbod, brother Dr. Ali Mirbod and sister Mahsa Mirbod, on whose constant encouragement, support, and love, I have relied throughout my life. Without their intense care and compassionate support, I would have never been able to come this far.

# Table of Contents

# List of Tables

# List of Figures

# Chapter 1 Introduction and background

## 1.1 Background and motivation

The initial motivation for the study of the generation of lift force in random, soft porous media grew out of several fundamental biological questions relating to the role of the fiber matrix layers that surround cells in an *in vivo* fluid environment, Weinbaum (1998). One of the most important of these layers, which is located on the luminal surface of vascular cells is the endothelial glycocalyx. It is composed of a negatively charged layer of endothelial proteoglycans, glycosaminoglycans, glycoproteins and lycolipids and harbors a wide array of enzymes that contribute in the regulation of leukocyte-thrombocyte adherence, with a principal role in plasma and vessel wall homeostasis. While the existence of the surface glycocalyx had been known for several decades, Luft (1966), it is only the past few years that it has been increasingly appreciated as an important factor in vascular physiology and pathology, as described by Pries *et al.* (2000) and in other, more recent reviews (Ballinger *et al.* 2004; Nieuwdorp *et al.* 2005; Weinbaum *et al.* 2007) and also in capillary hemodynamics and cell motion (Vink & Duling 1996; Damiano 1998; Secomb, Hsu & Pries 1998).

This layer has been estimated to vary from 0.1 μm in *in vitro* studies of frog mesentery capillaries, Adamson & Clough (1992), to 0.4 μm in *in vivo* studies of hamster cremaster microvessles, Vink & Duling (1996). More recent studies indicate that glycocalyx thickness increases with vascular diameter, at least in the arterial system, ranging from 2 to 3 μm in small arteries, van Haaren *et al.* (2003), to 4.5 μm in carotid arteries (Megens *et al.* 2007).

The surface glycocalyx provides a protective lubricating layer which prevents adhesive molecular interaction between proteins in the red cell membrane and their ligands in the plasmalemma membrane of the endothelial cell. The 8μm red cell is able to survive $10^5$ passages through the microcirculation during a typical lifetime of 120 days. This highly flexible cell is able to deform and squeeze through capillaries which are 5 to 6 μm diameter without rupturing either the membrane of the endothelial cells or its own plasmalemma.

Squire *et al.* (2001) proposed a quasi-periodic ultra-structural model for the 3D organization of the endothelial surface layer and its linkage to the sub-membranous cortical cytoskeleton. A schematic of this model is shown in Weinbaum *et al.* (2003), see Figure 1.1, where the bush like structure of the glycocalyx with its 20nm bi-directional periodicity for the core proteins and 100nm periodicity for the spacing of the core protein clusters is presented. They provided an overview of the various roles of the endothelial surface layer in the microcirculation from a new perspective. They showed that the flexural rigidity EI of the core proteins in the bush-like structures comprising the endothelial glycocalyx is sufficiently stiff for these structures to serve as a molecular sieve and a mechanical transducer of fluid shearing stresses. On the other hand, they showed that the buckling forces for the core proteins are one to two orders of magnitude smaller than the hydrodynamic forces generated during the arrest of motion of red blood cells. The properties, composition and visualization of the endothelial glycocalyx and its various functions have been reviewed in van den Berg *et al.* (2006); Weinbaum, Tarbell & Damiano (2007) and Reitsma *et al.* (2007).

Weinbaum, Tarbell and Damiano (2007) reviewed the structure of the glycocalyx and experiments that demonstrated its role in mechanotransduction and vascular remodeling. Using experiments with enzymes that degrade specific glycosaminoglycan components, they showed that the glycocalyx mediates the shear-induced production of nitric oxide, a central process in cardiovascular control, whereas the same enzyme treatments do not affect shear-induced production of prostacyclin, another hallmark of endothelial cell mechanotransduction. Van den Berg *et al.* (2006) showed that the endothelial glycocalyx exerts a wide array of functions to ensure maintenance of interstitial fluid balance and facilitating an anti-atherogenic vascular wall surface. An overview of the various ways in which the endothelial glycocalyx has been visualized, including first data from two-photon microscopic imaging was presented by Reitsma *et al.* (2007). Figure 1.2a, b shows (a) the visualization of the endothelial glycocalyx and (b) the surface glycocalyx coating the interior surface of a capillary in which the functional diameter of the capillary is significantly reduced by this surface matrix.

The glycocalyx was recognized as a red blood cell “exclusion zone” or “gap” between the flowing red blood cells and the endothelial membrane. In addition, the plasma was labeled by a fluorescent dextran, and the glycocalyx then appeared as a plasma exclusion zone as shown in Fig. 1.2b (Vink and Duling 1996). Interestingly, no exclusion zone was found for stiffer white blood cells, suggesting that they have the ability to compress the glycocalyx in these capillaries, which complies with the estimated low stiffness of the glycocalyx (Han *et al.* 2006; Secomb *et al.* 1998; Weinbaum *et al.* 2003). Zhao *et al.* (2001) proposed that rolling white blood cells can tip-toe across the endothelial glycocalyx surface layer in larger blood vessels.

The reason is that the major resistance to microvilli tip penetration arises from the viscous resistance of the glycocalyx, instead of the buckling force on core proteins, since the latter is weak in supporting normal compression.

One of the most striking observations in Vink & Duling (1996) was the so-called "pop out" phenomenon in which a red cell starting from rest would rise out of the layer as its velocity increased and at a velocity > 20 μm/s enter the central lumen of the vessel where upon it would move above the glycocalyx edge on a thin lubricating film. This was explained in Feng and Weinbaum (2000), using a lubrication theory for soft porous media in which the authors predicted that greatly enhanced lift forces could be produced in the glycocalyx layer at velocities less than 20 μm/s due to the large increase in pressure in the trapped porous layer between the red cell and the endothelial cell membrane. Detailed calculations in Secomb, Hsu & Pries (2001) clearly confirmed this prediction for a flexible red cell moving axisymmetrically along the axis of a cylindrical tube lined with a compressible matrix layer satisfiying the Brinkman equation.

Feng and Weinbaum (2000), hereafter referred to as F&W, developed a generalized lubrication theory based on an effective-medium approach (Brinkman equation) that is applicable to highly deformable porous layers. This theory is valid in the limit where the structure is so compressible that the normal forces generated by elastic compression of the fibers comprising the solid phase are negligible compared to the pressure forces generated within the porous layer. The simplified model that they constructed for the compression of the fibrous network in F&W, where the structure of the endothelial glycocalyx had not yet been identified, was that the fibers in the matrix form a periodic two-dimensional, diamond-shaped,

parallel array perpendicular to the flow direction. They found the local hydrodynamic resistance, or Darcy permeability, by using creeping flow theory. F&W predicted that the excess pore pressure generated by a planing surface moving on any compressible porous media scales as $\alpha^2 = h^2/Kp$, for $\alpha >> 1$, where h is the layer thickness and Kp is the Darcy permeability. $\alpha$ is of order $10^2$ or larger for both red blood cells gliding on the endothelial glycocalyx and humans skiing. Thus, the lift forces generated can be four or more orders of magnitude greater than classical lubrication theory.

Nearly every skier will tell you that skiing on fresh powder is like riding on air. Expert skiers achieve velocities in excess of ten times their body height per second due to gravitational forcing. However, this relative velocity is small compared to that which the red cell experiences in navigating through the microcirculation due to blood pressure. A red cell can achieve a velocity that approaches 100 times its diameter per second. Both fresh snow powder and the endothelial glycocalyx share a common property that they are highly porous and easily compressed. In contrast to snow, the glycocalyx appears to be completely resilient and returns to its equilibrium position in a fraction of a second after the passage of the cell. This restoration is due to a finite bending rigidity of the core proteins of the endothelial glycocalyx. Weinbaum *et al.* (2003) and Han *et al.* (2006) have predicted the flexural rigidity EI of the corproteins using linear and non-linear "elastica" theory, respectively, and have used this to estimate the recoil time for the restoration of glycocalyx after the passage of a white cell.

F&W suggested that there might be a striking similarity between a human skier or snowboarder gliding on fresh snow powder and the red cell skimmimg along the surface of the endothelial glycocalyx although they differ in mass by $10^{15}$.

In the case of snow, the lift forces generated by the porous media protect the bottom of our skis from the roughness of the surface beneath the powder and in the case of the red cell, the endothelial surface glycocalyx prevents molecular–level adhesive interactions between the endothelial and red cell membranes. In both cases, F&W showed that the pressure forces generated within the compressed porous layer are approximately four orders of magnitude greater than that predicted by classical lubrication theory where the gap is filled with a pure fluid. However, the red cell is far more efficient since for the human skier or snowboarder much of the excess pressure that is built up beneath the planing surface leaks out at the lateral edges of the ski or snowboard as shown in Fig. 1.3 and the pressure and lift forces decrease as $(W/L)^2$.

More recently, Wu *et al.* (2005) theoretically and experimentally explored the large $\alpha$ behavior for snow using a novel piston-porous cylinder apparatus where the escape of air from the compressed snow layer was examined on the time scale of skiing or snowboarding for the first time. Wu *et al.* (2006), then used these results to develop a more general theory for skiing and snowboarding wherein the forces and moments due to both the trapped air and compressed solid phase of the ice crystals were taken into account and empirically determined values of the Darcy permeability of snow were employed for different snow conditions. These results were then applied to theoretically predict the fraction of the total lift force provided by the air that was transiently trapped beneath a ski or snowboard, and the stability

that is achieved by shifting the center of gravity of the snowboarder. Typically, one finds that for fine powder about one half of the total lift for a snowboard comes from the air and about 40% for a ski when traveling at 10 m/s. However, in either skiing or snowboarding there is a large loss of pore pressure at the lateral edges of the ski or snowboard and the pressure and lift force decrease as $(L/W)^{-2}$ for large $\alpha$. Wu *et al.* (2004) applied the lesson learned from red cell motion in a capillary and human skiing on compressed snow powder to design a high speed vehicle with a giant ski which could ride on a track made of highly compressible porous media. They proposed a novel soft porous track wherein the fiber layer is attached to the bottom boundary of a channel with impermeable sidewalls, the porous material was not identified or characterized, the stability of the vehicle and its performance were not examined or was a possible propulsion system discussed.

## 1.2 Thesis outline

In chapter 2 of the present study, the generation of pressure and lift forces in a random, soft fibrous media layer that is confined between two planar surfaces, an infinite horizontal lower boundary and a horizontal inclined upper boundary, in the lubrication limit where the characteristic thickness of the fiber layer, $H \ll L$, the length of the inclined surface is examined. The model for the fiber layer is a Brinkman equation and the Darcy permeability, $K_p$, is described by the widely used Carman-Kozeny equation for a random porous media. Two cases are considered, (a) an inclined upper boundary which slides freely on top of a stationary fiber layer which is firmly attached to the lower boundary and (b) an inclined stationary upper boundary with an attached fiber layer in which the horizontal lower boundary slides

freely in its own plane beneath it. Superficially, the problems appear equivalent to the classical problem for a slider bearing where the solution for the pressure distribution and lift force are independent of which boundary is moving and there is an optimum compression ratio, $k=h_1/h_2=2.2$, where $h_1$and $h_2$ are the heights at the leading and trailing edges, for maximum lift force. However, this symmetry is lost if the intervening space is filled with a soft porous, fibrous material since the Brinkman equation is not invariant under a transformation of coordinates in which the inherently unsteady problem in case (a) is transformed to a steady reference frame in which the inclined upper boundary is stationary and the horizontal boundary with the adhered fiber layer moves below it. Although in the steady reference frame case (a) now appears to resemble case (b), the solutions are strikingly different and depend critically on the value of the dimensionless fiber interaction layer thickness $\alpha = H/\sqrt{K_p}$ . For $\alpha<<1$ the solutions for both cases approach the classical solution for a slider bearing. For $\alpha>>1$ I show, using asymptotic analysis, that the solutions diverge dramatically. In case (a) the pressure and lift force increase as $\alpha^2$ and asymptotically approach a limiting behavior for large values of $\alpha$, as first predicted in Feng and Weinbaum (2000), while in case (b) the pressure and lift force decay as $\alpha^{-2}$ since the inclined upper boundary is screened by the fiber layer and the amount of fluid dragged through the fluid gap decreases as $\alpha$ increases and vanishes for $\alpha>>1$ . The solution in case (a), where the inclined upper boundary moves, is of particular interest since it reveals the potential to generate enormous lift forces using commercially available, inexpensive, soft porous materials provided the lateral leakage at the edge of the planform can be eliminated through the use of a channel with impermeable

sidewalls as first proposed in Wu et al (2004). The behavior is illustrated for both a toboggan sliding in such a channel and a larger planform that might be useful in commercial transportation.

In chapter 3, the quantitative feasibility and performance of an airborne jet train that flies on a soft porous track within centimeters of the earth's surface at speeds approaching current commercial jet aircraft is explored. The jet train employs a lift mechanism first described for red cells gliding on the endothelial glycocalyx and subsequently used to predict the lift forces generated in skiing and snowboarding by the transiently trapped air beneath their planing surfaces. Using an asymptotic analysis for large values of the permeability parameter, $H/\sqrt{K_p}$, where H is the porous layer thickness and $K_p$ the Darcy permeability, I first show that it is possible to support a 70 metric ton jet train carrying 200 passengers on a confined porous material if its $K_p$ is approximately $5 \times 10^{-9}$ $m^2$. For this $K_p$ one finds that the tilt of the planform is < 0.1 degrees and the lift-off velocity is < 5 m/s. This value of $K_p$ can be satisfied by a random fiber matrix with a fiber radius of 5 μm and a void fraction of 0.995. Compression tests on a fiber-fill material with these properties show that the fibers contribute < 0.2 percent of the total lift and hence the friction force of the fiber phase is negligible. Using jet engines of 10,000 lbf thrust, about 1/5 that of a 200 passenger jet aircraft, one is able to obtain a cruising velocity approaching 700 km/hr. This would allow for huge fuel savings, especially on short flights where much of the energy expenditure is used to climb to altitude and overcoming lift induced drag.

Chapter 4, concludes the thesis, highlights the contributions and suggests future applications.

In Appendix I, an experiment has been designed to examine the generation of dynamic lift forces during compaction of soft highly compressible fibrous materials in a piston/cylinder apparatus. Novel experimental techniques have been developed to simultaneously measure and separate out the dynamic forces acting on the compressing piston by the air and solid phases respectively. The measurements clearly demonstrate that the excess pore pressure builds up inside the porous material and reaches its maximum before there is any significant rise in the solid phase force. The air pressure subsequently decays due to air venting into the ambient environment at the edges of the testing apparatus as the solid phase force rapidly rises.

In Appendix II, an initial laboratory scale model of the airborne jet train (AJT) and its track has been designed to measure the pressure signals as the planfrom passes over a particular location. A lift weight W of 1 kg fully supported when airborne by a planform that is 65 cm long and 10 cm wide symmetrically positioned beneath the model is considered. The prototype model used the same porous media, described in Mirbod *et al.* (2009a) for the full scale AJT, where the Darcy permeability, $Kp=3.4x10^{-9}$ $m^2$. The basic design parameters of the laboratory scale model, such as its velocity and tilt angle, are predicted using the theory presented in Mirbod *et al.* (2009b).

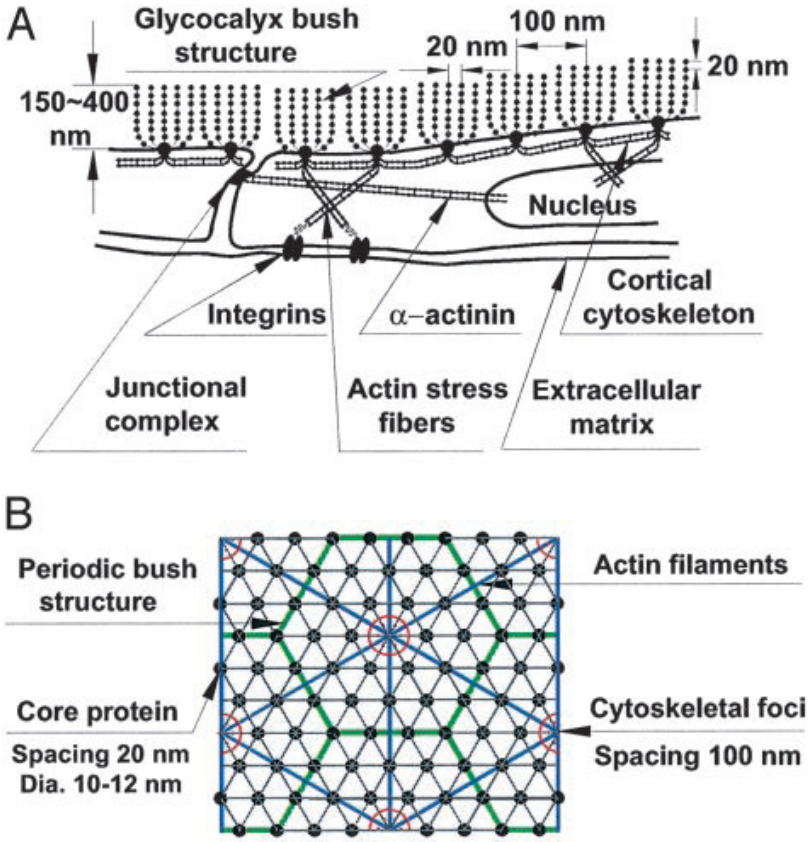


Figure 1.1 (A) Sketch of Endothelial surface glycocalyx (not to scale) showing core protein arrangement and spacing of scattering centers along core proteins and their releationship to actin cortical cytoskeleton as proposed in Squire *et al.* (2001). (B) En face view of idealized model for core protein clusters and cluster foci and their relationship to hexagonal actin lattice in cortical cytoskeleton. (Adapted from Fig. 1 in Weinbaum *et al.* 2003)

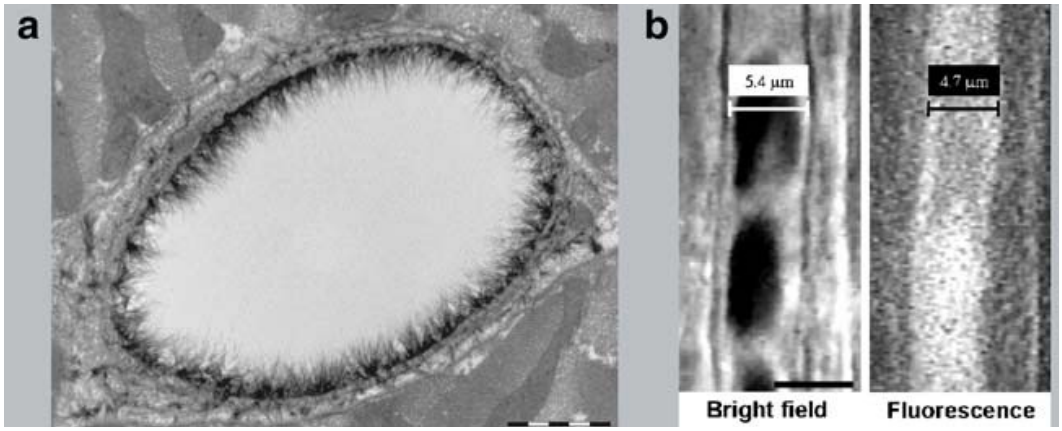


Figure 1.2 Visualization of the endothelial glycocalyx with different microscopic techniques. (a) Endothelial glycocalyx of a rat left ventricular myocardial capillary stained with Alcian blue 8GX and visualized using electron microscopy. Bar represents 1 µm. Reproduced from van den Berg *et al.* (2003) (b) Intravital microscopic recording of the endothelial glycocalyx of a hamster cremaster muscle capillary. The anatomical diameter of 5.4 µm is larger than the red blood cell column width (left pane) or the plasma column width (right pane) labeled with fluorescent dextran (70 kD). This difference is caused by the presence of the endothelial glycocalyx. The bar in the left pane represents 5 µm. Reproduced from Vink and Duling (1996). (Adapted from Fig. 2 in Reitsma *et al.* 2007)

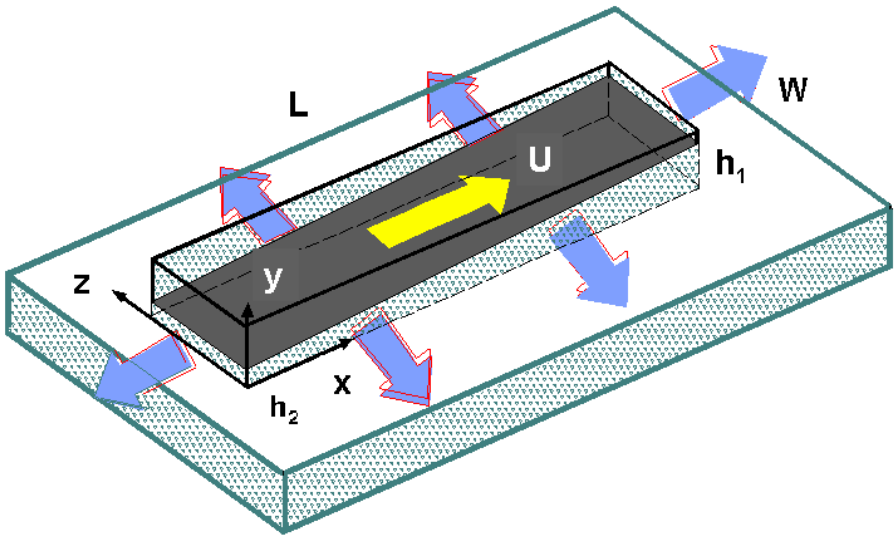


Figure 1.3 Schematic illustration of a snowboard or ski compressing a thin layer of fresh powder. Note the escape of air at lateral edges. (Adapted from Fig. 11 in Feng and Weinbaum 2000)

# Chapter 2 On the generation of lift force in random, soft porous media

## 2.1 Introduction

In this chapter we examine the generation of pressure and lift forces in a random, soft fibrous media layer that is confined between two planar surfaces, an infinite horizontal lower boundary and a horizontal inclined upper boundary, in the lubrication limit where the characteristic thickness of the fiber layer, H << L, the length of the inclined surface. This type of flow has arisen in a number of important flow applications in which unexplained or unusual behavior has either been observed or theoretically predicted. These include: (i) the anomalous behavior observed in the single file motion of red cells *in vivo* and in small glass tubes of comparable diameter (Pries *et al.* 1994; Pries, Secomb & Gaehtgens 2000), (ii) the striking similarity between a red cell gliding on the endothelial glycocalyx (0.2 to 0.5 μm thick fiber matrix layer coating the inner lining of all our blood vessels) and a human being snow boarding on fresh snow powder (Feng and Weinbaum, 2000; Wu *et al.*, 2006), and (iii) the possibility of generating vastly enhanced lift forces using a novel track in which an inclined planar surface rides on a soft porous fiber layer in a channel with impermeable side walls (Wu, Andreopoulos & Weinbaum 2004).

The studies in (i) describe a fundamental paradox that attracted considerable attention in the biorheology community in the 1980s and 1990s. Numerous experimental studies summarized in Pries *et al.* (1994, 2000) had clearly shown that the flow resistance of red cells moving single file in true capillaries had several

times the resistance of red cells moving in narrow glass tubes of comparable diameter, reviewed in Chien, Usami & Skalak (1984). This was particularly evident in capillaries of 5-6 μm diameter where the 8 μm red cell underwent large deformations from its biconcave disc shape and assumed the shape of a moving bolus. Superficially, the flow problems appeared to be identical, but Vink and Duling (1996) demonstrated *in vivo* that the inner lining of our capillaries was lined with a ubiquitous endothelial glycocalyx layer of 0.4 to 0.5 μm thickness. The properties of this layer and its various functions have recently been reviewed in Weinbaum, Tarbell & Damiano (2007). One of the most striking observations in Vink and Duling was a so called "pop out" phenomena in which a red cell starting from rest would rise out of the layer as its velocity increased and at a velocity greater than 20 μm/s enter the central lumen of the vessel where upon it would move above the glycocalyx edge on a thin lubricating film. This was explained in Feng and Weinbaum (2000), hereafter referred as F&W, using a lubrication theory for soft porous medium in which the authors predicted that greatly enhanced lift forces could be produced in the glycocalyx layer at velocities less than 20 μm/s due to the large increase in pressure in the trapped porous layer between the red cell and endothelial cell membranes. Detailed calculations in Secomb, Hsu & Pries (2001) clearly confirmed this prediction for a flexible red cell moving axisymmetrically along the axis of a cylindrical tube lined with a compressible matrix layer satisfying the Brinkman equation. In marked contrast, red cells in glass tubes appear to fill nearly the entire lumen of the tube when moving at both high and low speeds suggesting that if there was an adhered layer of macromolecules coating the red cell membrane these lift forces were either absent or greatly diminished.

The red cells moving in narrow glass tubes and in capillaries illustrate the two superficially similar flow geometries that will be examined in this chapter. In the case of the red cells moving in capillaries, case (a) in Fig. 2.1a, a planing surface is moving with a small tilt angle relative to a horizontal rigid boundary with an attached matrix layer. This is an inherently unsteady problem in which the lower boundary and its attached fiber layer are stationary and the latter is being compressed by the tilt of the moving upper boundary which drives the fluid through the attached porous layer. The theories of Weinbaum *et al.* (2003) and Han *et al.* (2006) show that if the fibres have the flexural rigidity $EI$ of ~500 pN nm$^2$, this would be sufficient to prevent any significant change in thickness of the glycocalyx layer when it is exposed to fluid shear stresses in the physiological range at its top surface. However, this flexural rigidity is insufficient to prevent the layer from collapsing when the motion of the red cell is arrested. Weinbaum *et al.* propose that the major function of the small flexural rigidity of the glycocalyx fibers is the transmission of fluid shear stresses to the internal actin cytoskeleton of the cell in mechanotransduction. This was clearly demonstrated in Thi *et al.* (2004) where cytoskeletal responses were abrogated when the glycocalyx was enzymatically compromised. The resistance to compression of the glycocalyx has also been attributed to oncotic forces arising from trapped proteins in the layer (Secomb, Hsu & Pries 2001) or electro-chemical repulsive forces (Damiano and Stace 2002). In the case of red cells moving in glass tubes, where a matrix layer is also believed to be attached to the red cell membrane, case (b) in Fig. 2.1b, one has a steady problem. Here both the red cell and its attached matrix layer are stationary and the horizontal lower boundary moves beneath it without any compression of the matrix.

The mechanical properties of the glycocalyx have been largely deduced from the non-linear elastic recoil of the glycocalyx layer after the passage of a tightly fitting white cell. This recoil is described using large deformation 'elastica' theory for the fibers and a Brinkman equation for the fluid motion in Han *et al.* (2006). A more general small deformation theory for the deformation of the fibers when subject to oscillating fluid shear stress is presented in Han, Ganatos and Weinbaum (2005). In the present analysis the shear deformation of the fibers is neglected but the variation in permeability $K_p$ due to the local compression of the layer is considered. It is assumed that the fibers compress easily and contribute negligibly to the lift forces exerted on the inclined upper boundary. In the absence of this elastic restoring force there is little friction between the fibers and inclined upper boundary. Similarly, for the soft fiber-fill used in the applications in section 2.6 one observes only minor shear deformations of the matrix.

The enhanced pressure and lift forces generated in the matrix by the motion of the inclined upper boundary in Fig. 2.1a was first treated in Feng & Weinbaum (2000), who developed a generalized two-dimensional lubrication theory for highly compressible porous media using effective medium theory based on the use of the Brinkman equation. Prior analyses by Damiano (1998) and Secomb, Hsu & Pries (1998) also used a Brinkman equation to describe the flow in the glycocalyx layer, but the red cells did not invade the layer and a thin layer of fluid was assumed to exist between the edge of the layer and the red cell membrane. In Feng &Weinbaum (2000) the authors also treat the Darcy permeability parameter, $\alpha = H/\sqrt{K_p}$, as a spatially varying parameter that takes account of the local elastic compression of the fibers. The two most striking predictions of this analysis were that: (i) greatly

enhanced lift forces could be generated that scaled as $\alpha^2$ for large $\alpha$ as the compression of the fiber matrix increased, and (ii) as unexpected as it might seem at first glance, the value of $\alpha$ for a red cell gliding on the glycocalyx layer, which was estimated as 160, was nearly the same as a human snowboarding on fresh snow powder, although the red cell and human differ in mass by 15 orders of magnitude. In this initial study the Darcy permeability $K_p$ was computed for a deformed periodic array of parallel cylindrical fibers using an extension of the theory in Sangani and Acrivos (1982) for Stokes flow transverse to the fiber array.

One of the unexpected predictions of the analysis in Feng & Weinbaum (2000) was that, there was no optimum compression ratio, $k = h_1/h_2$, where the lift force could be maximized when $h_1$ is fixed. Here the subscripts 1 and 2 refer to the leading and trailing edges, respectively, of the planar surface. In marked contrast, for classical lubrication theory, $\alpha = 0$ (no fibers present), one of the best known results for a slider bearing is that for $k = 2.2$, one obtains maximum lift when the height of the trailing edge $h_2$ is held fixed. Another well-known result of classical lubrication theory for the slider bearing is that the pressure distribution in the fluid gap is identical whether the inclined upper boundary or the flat lower boundary is moving. This does not hold true when the intervening layer is a confined porous media where a dramatic difference in behavior emerges as $\alpha$ increases for $\alpha > 1$ depending on whether the matrix is attached to the horizontal lower or inclined upper boundary. We shall show herein that the pressure distribution decays to zero in case (b) where the lower boundary moves and the inclined boundary and matrix are stationary, whereas in case (a) where the inclined upper boundary moves and the lower boundary and matrix are stationary, one obtains the huge increase in lift

described in Feng &Weinbaum (2000) as $\alpha$ increases. These paradoxical behaviors are analyzed in the present chapter both numerically and using asymptotic analysis for small and large values of $\alpha$.

Subsequent to Feng &Weinbaum (2000), Wu et al (2005) theoretically and experimentally explored the large $\alpha$ behavior for snow using a novel piston-porous cylinder apparatus where the escape of air from the compressed snow layer was examined on the time scale of skiing or snowboarding for the first time. These results were then used to develop a more general theory for skiing and snowboarding wherein the forces and moments due to both the trapped air and the compressed solid phase of the ice crystals were taken into account and empirically determined values of the Darcy permeability of snow were employed for different snow conditions, (Wu *et al.* 2006). However, in either skiing or snowboarding there is a large loss of pore pressure at the lateral edges of the ski or snowboard and the pressure and lift force decrease as $(W/L)^2$ for large $\alpha$ where W is the width of the planning surface. This observation led the authors in Wu *et al.* (2004) to propose a novel soft porous track wherein the fiber layer is attached to the bottom boundary of a channel with impermeable sidewalls. This would enable one to exploit the full effect of the huge increase in lift for $\alpha >> 1$ by eliminating the loss of pressure at the lateral edges. For this case, the two-dimensional analysis in Feng &Weinbaum (2000) for a ski or snowboard reduces to the much simpler unidirectional flow geometry in Fig. 2.1a. Wu *et al.* (2004) also show that this new track had the potential to support the weight of a train car moving at relatively modest speeds on synthetic porous materials which had the permeability properties of down feathers. This prediction led to a search for a soft, durable, inexpensive porous material with

similar permeability properties and the discovery that the polyester fibers used in inexpensive body pillows were ideal for this application (Mirbod, Andreopoulos & Weinbaum 2009b). This fiber-fill material is more adequately described by the widely used empirical Carman-Kozeny equation for random porous media. The calculations in the present study are performed using this empirical relation and the results applied to both a toboggan riding on a soft porous track and a jet train that is described in much greater detail in Mirbod *et al.* (2009b).

In F&W and all previous studies of the glycocalyx layer, the flow in the matrix has been described using a Brinkman equation. As pointed out by the reviewers, the Darcy term in the Brinkman equation is not frame invariant under a Galilean transformation in which the flow geometry in case (a), Fig. 2.1a, is transformed to a steady coordinate system in which the observer rides on the inclined upper boundary and the lower boundary with its attached matrix moves with uniform velocity U to the left. Although cases (a) and (b) now look similar, they differ in that in (a) the matrix is attached to the lower boundary and in (b) to the upper boundary. This difference leads to a new $\alpha^2$ term in the generalized dimensionless Brinkman equation which is related to the flow that is generated by the tilt of the moving upper boundary in the original unsteady coordinate system in Fig. 2.1a. This generalized equation, which is based on binary mixture theory for a dilute solid constituent takes account of the relative motion of the fluid and solid phases in the description of the Darcy term (Roy & Damiano 2008). The pressure and lift force are unaffected since they are independent of the velocity transformation.

The chapter is organized into six sections. In section 2.2, the governing equations for cases (a) and (b) are derived. In section 2.3, we examine the behavior of the Carman-Kozeny equation for a random array of cylindrical fibers of uniform radius. In section 2.4, we numerically solve the governing equations for both cases (a) and (b) and perform an asymptotic analysis for small and large values of $\alpha$ for both flow geometries. In section 2.5, we present the results and in section 2.6, we briefly describe the applications.

## 2.2 Lubrication theory for the fibrous layer

Classical lubrication theory was initially developed by Reynolds for an incompressible, Newtonian fluid (Schlichting 1979). This was subsequently generalized for Newtonian fluids with variable properties and non-Newtonian fluids. The theory has been applied to both impermeable and porous walled journal-bearing systems. A more recent application of lubrication theory has been to biological systems where the walls are not porous, but the lubricating layer itself is a soft porous medium. As first proposed by Damiano (1998) and Secomb *et al.* (1998), this layer has been described by a Brinkman equation (Brinkman 1947) in nearly all subsequent theoretical analyses. Shortly thereafter, F&W demonstrated that if the red cell entered the glyccocalyx layer its compression could be large leading to significant variations in the Darcy permeability $K_p$ and dramatic changes in the pressure distribution in the layer for large compressions.

The inherently unsteady-flow problem in Fig. 2.1a can be readily converted to a steady flow in which a fixed observer sits on the inclined upper boundary and the lower boundary with its attached matrix moves with velocity $\bar{u}_s = -Ui$ to the left

beneath it. In this new steady $(x', z')$ coordinate system the absolute velocity of the fluid in the $x'$-direction is $\bar{u} = u'i$ and the relative velocity between the fluid and solid constituents which appears in the Darcy term is $\bar{u} - \bar{u}_s = (u' + U)i$. The generalized Brinkman equation for the motion of the fluid in the steady coordinate system is given by Roy and Damiano (2008) as

$$\frac{\partial^2 \bar{u}}{\partial z'^2} - \frac{\bar{u} - \bar{u}_s}{K_p} = \frac{1}{\mu}\frac{dp'}{dx'}, \tag{2.1}$$

Here μ is the fluid viscosity, p′ is the fluid pressure and primes indicate dimensional quantities. Equation (2.1) can be written in dimensionless form by introducing the dimensionless quantities

$$x = \frac{x'}{L},\ z = \frac{z'}{h'},\ h = \frac{h'}{H},\ p = \frac{p'H^2}{\mu LU},\ u = \frac{u'}{U} \tag{2.2}$$

Here L is the length of the planing surface, h(x,t) is a local dimensionless height scaled by H, a convenient reference height and U is the magnitude of the velocity of the lower boundary and solid phase. The dimensionless form of equation (2.1) is

$$\frac{\partial^2 u}{\partial z^2} - \alpha^2 (u + 1) = \frac{dp}{dx}. \tag{2.3}$$

The solution to (2.3) which satisfies the no-slip boundary conditions $u(x,0) = -1$ at $z = 0$ and $u(x,h) = 0$ at $z = h$ is given by

$$u(x,z) = \frac{\sinh \alpha z}{\sinh \alpha h} + \frac{1}{\alpha^2}\frac{\partial p}{\partial x}\left[\cosh \alpha z - 1 - \frac{\sinh \alpha z}{\sinh \alpha h}(\cosh \alpha h - 1)\right] - 1. \tag{2.4}$$

The corresponding flux in the x-direction, is computed by integrating over the local dimensionless channel height

$$\hat{Q} = \int_0^h \hat{u} d\hat{z} = f + \frac{1}{\alpha^2}\frac{\partial p}{\partial \hat{x}}(2f - h) - h, \tag{2.5}$$

where,

$$f = \frac{\cosh \alpha h - 1}{\alpha \sinh \alpha h},\ \alpha = \frac{H}{\sqrt{K_p}}, \tag{2.6}$$

Here $\alpha$ is a dimensionless permeability parameter defined in terms of $K_p$, the dimensional Darcy permeability.

In the transformed steady coordinate system the flux, $\hat{Q}$, is a constant from continuity and thus,

$$\frac{d\hat{Q}}{d\hat{x}} = 0. \tag{2.7}$$

Combining (2.5) and (2.7) one has,

$$\frac{d}{\partial \hat{x}}\left[ f + \frac{1}{\alpha^2}\frac{dp}{d\hat{x}}(2f - h)\right] = \frac{dh}{d\hat{x}}. \tag{2.8}$$

This last result is the same as equation (2.25) in F&W, which was derived without using this coordinate transformation. The results for the velocity profiles and streamlines are also plotted in the moving unsteady coordinate system in F&W. The pressure profiles and lift forces are independent of coordinate system.

For case (b), figure 2.1(b), there is no need to transform coordinates since the matrix is attached to the stationary inclined upper boundary and the horizontal

lower boundary moves in its own plane to the right. Thus $\bar{u}_s = 0$, the $\alpha^2$ term in (2.3) is missing, and the second term reduces to $-\alpha^2 u$. There is no compression of the porous media as in case (a). The solution of equation (2.3) with the $\alpha^2$ term missing which satisfies the no-slip boundary conditions *u(x,0)=+1* at *z=0* and *u(x,h)=0* at *z=h* is given by

$$u(x,z) = -\cosh \alpha h \frac{\sinh \alpha z}{\sinh \alpha h} + \cosh \alpha z + \frac{1}{\alpha^2}\frac{\partial p}{\partial x}\left[\cosh \alpha z - 1 - \frac{\sinh \alpha z}{\sinh \alpha h}(\cosh \alpha h - 1)\right]. \tag{2.9}$$

The corresponding flux in the x-direction, is given by

$$Q = \int_0^h u dz = f + \frac{1}{\alpha^2}\frac{\partial p}{\partial x}(2f - h), \tag{2.10}$$

Again continuity requires that Q is constant or

$$\frac{dQ}{dx} = 0. \tag{2.11}$$

Combining (2.10) and (2.11), in case (b) one has,

$$\frac{d}{\partial x}\left[f + \frac{1}{\alpha^2}\frac{dp}{dx}(2f - h)\right] = 0. \tag{2.12}$$

In both cases (a) and (b) $h_2$ is fixed and chosen as the reference height H. The term on the right hand side of (2.8) is due to the forward motion of the upper inclined plane in figure 2.1(a), which compresses the stationary matrix layer, whereas this term vanishes in equation (2.12) because the inclined upper boundary and its attached matrix are stationary. In classical lubrication theory it does not make any difference which plane is moving since the starting momentum equation without the

second term on the L.H.S in equation (2.1) is invariant under a Galilean coordinate transformation.

The Reynolds equations (2.8) and (2.12) can be solved for the pressure distribution using appropriate boundary conditions. Once the pressure field is determined, the velocity profiles and the lift force are readily obtained. These results are presented and discussed in sections 2.4 and 2.5, respectively.

## 2.3 Permeability of the fibrous media

In F&W the variation of $K_p$ with x is determined by solving the Stokes creeping motion equations for the flow perpendicular to the axis of an array of circular cylindrical fibers whose vertical spacing changes proportionally with the local dimensionless height h. In the present application we shall consider a random array of cylindrical fibers of uniform diameter. This is a very good representation for the inexpensive polyester fiber-fill that is extensively used in commercially available pillows. This material has been chosen because of the applications that are discussed in section 2.6. A random fiber array of this nature is most conveniently described by the widely used empirical Carman-Kozeny equation (see Happel and Brenner 1983),

$$K_p = \frac{\varepsilon^3}{G s_0^{\,2} (1-\varepsilon)^2} \ , \tag{2.13}$$

where $\varepsilon$ is the void fraction, $(1-\varepsilon)$ is the solid fraction, G is an empirically measured Kozeny constant and $s_0$ is the Carman-specific surface, defined as the area of the surface that is exposed to the fluid per unit volume of the solid phase. For cylindrical fibers of radius $r_f$

$$s_0 = \frac{2\pi r_f L_f}{\pi {r_f}^2 L_f} = \frac{2}{r_f} \ , \tag{2.14}$$

where $L_f$ is the total fiber length per unit volume. For these fibers, equation (2.13) becomes

$$K_p = \frac{{r_f}^2 \varepsilon^3}{4G(1-\varepsilon)^2} \ . \tag{2.15}$$

The value of G depends on the porosity. When the fibers are randomly oriented, Happel and Brenner (1983) give the following expression for G(ε),

$$G(\varepsilon) = \frac{2\varepsilon^3}{3(1-\varepsilon)} \left\{ \frac{1}{-2\ln(1-\varepsilon) - 3 + 4(1-\varepsilon) - (1-\varepsilon)^2} + \frac{2}{-\ln(1-\varepsilon) - \left[1-(1-\varepsilon)^2\right] / \left[1+(1-\varepsilon)^2\right]} \right\}. \tag{2.16a}$$

When $\varepsilon \to 1$, equation (2.16a) is frequently approximated by

$$G(\varepsilon) \to \frac{-5}{3(1-\varepsilon)\ln(1-\varepsilon)} . \tag{2.16b}$$

One observes from (2.15) that $\frac{K_p}{{r_f}^2}$ is only a function of $(1-\varepsilon)$ for both (2.16a) and (2.16b) when $\varepsilon \to 1$. Since $(1-\varepsilon)$ will be less than 0.01 for all values of $\alpha$ considered herein, one concludes from figure 2.2 that $\frac{K_p}{{r_f}^2}$ is closely approximated by

$$\frac{K_p}{{r_f}^2} = -\frac{3}{20} \frac{\ln(1-\varepsilon)}{(1-\varepsilon)} , \tag{2.17}$$

obtained by combining equations (2.15) and (2.16b).

The variation of $\frac{K_p}{{r_f}^2}$ as a function of $h/h_2$ is obtained directly from the curves in figure 2.2. A relatively simple and reasonable assumption is that when the fiber

layer is compressed the increase in fiber density is locally proportional to the decrease in height of the fiber layer as a function of x. Thus, the solid fraction $(1-\varepsilon)$ decreases as $h_2/h$ where $h_2$ is the height of the layer at the leading edge of the planform in case (b) and the trailing edge in case (a). Using equation (2.17) and the foregoing assumptions for the variation of $K_p$ with h, one can define a dimensionless local Darcy permeability $\tilde{K}_p$ by

$$\tilde{K}_p = \frac{K_p(h)}{K_{p2}} = h - \frac{h \ln h}{\ln(1-\varepsilon_2)}, \tag{2.18}$$

where $K_{p2}$ is the minimum value at $h = h_2$. Figure 2.3 shows the variation of $\frac{K_p(h)}{K_{p2}}$ as a function of $h/h_2$ for representative values of $(1-\varepsilon_2)$ in which $\varepsilon_2$ is the void fraction at $h = h_2$. The value of $(1-\varepsilon)$ for the polyester fiber fill in the undeformed state in our applications in section 2.6 is 0.00467.

## 2.4 Solutions to boundary value problem

A general solution to the boundary value problem for equations (2.8) and (2.12) can be obtained by applying boundary conditions at the leading and trailing edges of the planform, x = 0 and 1. This general solution was previously obtained for case (a), inclined upper boundary moving, in F&W, but is included herein for easy comparison with case (b), which is new. We will then examine the behavior of these solutions for both $\alpha << 1$ and $\alpha >> 1$. In the small $\alpha$ limit it is clear that equations (2.1) and (2.3) are identical for $\alpha = 0$, but differ by the $\alpha^2$ term in (2.3) for $\alpha > 0$. We shall use perturbation theory to calculate the lowest order corrections for

the pressure distribution in the two cases. In the large $\alpha$ limit the two solutions dramatically diverge, one solution for pressure and lift force increasing as $\alpha^2$ and the other decaying as $\alpha^{-2}$.

The general solutions to equations (2.8) and (2.12) can be obtained for an arbitrary variation of h(x) assuming that $K_p$, and hence $\alpha$, only vary with x. Note also that the tilt of the inclined boundary has been reversed for the two cases so that the pressure profiles will not lie on top of one another in the small $\alpha$ limit. As discussed in the previous section the compression of the fiber layer is assumed to be locally uniform throughout the height of the layer. The first integrals of (2.8) and (2.12) are

$$f + \frac{1}{\alpha^2}\frac{dp}{dx}(2f - h) = h + C_1, \tag{2.19a}$$

$$f + \frac{1}{\alpha^2}\frac{dp}{dx}(2f - h) = C_2, \tag{2.19b}$$

where $C_i$, i=1,2 are constants of integration. The constants $C_i$ are evaluated by prescribing the leading and trailing edge pressures. The $C_i$ can be expressed as

$$C_1 = -\frac{\int_0^1 \frac{\alpha^2 (h-f)}{(2f-h)} dx}{\int_0^1 \frac{\alpha^2}{(2f-h)} dx}, \tag{2.20a}$$

$$C_2 = \frac{\int_0^1 \frac{\alpha^2 f}{(2f-h)} dx}{\int_0^1 \frac{\alpha^2}{(2f-h)} dx}. \tag{2.20b}$$

The pressure distributions from (2.19a) and (2.19b) are given by

$$p_1 - p_0 = \int_0^x \frac{\alpha^2 (h + C_1 - f)}{2f - h} dx, \tag{2.21a}$$

$$p_2 - p_0 = \int_0^x \frac{\alpha^2 (C_2 - f)}{2f - h} dx \ . \tag{2.21b}$$

in which $p_0$ is the pressure at x=0 and x=1 and the $C_i$ are given by (2.20a) and (2.20b).

The total dimensionless lift force F is obtained by integrating (2.21a) and (2.21b) over the entire surface. This leads to

$$F_1 = \int_0^1 (p_1 - p_0) dx = \int_0^1 (1 - x) \frac{\alpha^2 (h + C_1 - f)}{2f - h} dx, \tag{2.22a}$$

$$F_2 = \int_0^1 (p_2 - p_0) dx = \int_0^1 (1 - x) \frac{\alpha^2 (C_2 - f)}{2f - h} dx, \tag{2.22b}$$

where we have changed the order of integration in evaluating the double integral. Once h(x) is prescribed, equations (2.20)-(2.22) provide a remarkably simple solution for the pressure distribution and lift force in the compressed matrix layer for any h(x).

### 2.4.1 Small $\alpha$ limit

In the limit $\alpha \to 0$, one can expand f in (2.6) as

$$f \to \frac{h}{2} - \frac{\alpha^2 h^3}{24} + \frac{\alpha^4 h^5}{240} + O(\alpha^6). \tag{2.23}$$

If one substitutes the first two terms of (2.23) into (2.20a, b) and retains only the terms which are of order O(1), one finds that $C_1 = -C_2$, see equation (2.26a, b). If these values of the $C_i$ are now put back in (2.19a, b) one obtains

$$\frac{dp}{dx} = \pm\frac{12C_1}{h^3} \pm \frac{6}{h^2}, \tag{2.24}$$

where the minus sign describes case (a) and the plus sign describes case (b). Thus, in the limit $\alpha = 0$ the two cases are identical except that the pressure gradient at x in case (a) is the negative of the pressure gradient at (1-x) in case (b), as noted previously. This is simply a result of the fact that the slopes of the upper boundaries in figures 2.1a, b are reversed and when equation (2.24) is integrated the pressure profiles will be mirror images of one another.

The above symmetry is lost once one retains the third term in (2.23). The common expression $\frac{\alpha^2}{2f-h}$ that appears in (2.20) and (2.21) can be expanded as

$$\frac{\alpha^2}{2f-h} = -\frac{12}{h^3}\left(1 + \frac{\alpha^2 h^2}{10} + O(\alpha^4)\right). \tag{2.25}$$

To $O(\alpha^2)$, one finds from equations (2.20a, b) that $C_1$ and $C_2$ are

$$C_1 = -\frac{\int_0^1 \frac{dx}{h^2}}{2\int_0^1 \frac{dx}{h^3}} - \frac{\alpha^2}{20\int_0^1 \frac{dx}{h^3}}\left[\frac{11}{6} - \frac{\int_0^1 \frac{dx}{h^2}\cdot\int_0^1 \frac{dx}{h}}{\int_0^1 \frac{dx}{h^3}}\right] + O(\alpha^4), \tag{2.26a}$$

$$C_2 = \frac{\int_0^1 \frac{dx}{h^2}}{2\int_0^1 \frac{dx}{h^3}} + \frac{\alpha^2}{20\int_0^1 \frac{dx}{h^3}}\left[\frac{1}{6} - \frac{\int_0^1 \frac{dx}{h^2}\cdot\int_0^1 \frac{dx}{h}}{\int_0^1 \frac{dx}{h^3}}\right] + O(\alpha^4). \tag{2.26b}$$

Using (2.23), (2.24) and simplifying, one obtains

$$p_1 - p_0 = -\int_0^x \frac{6}{h^2}dx - \int_0^x \frac{12C_1}{h^3}dx - \frac{\alpha^2}{10}\left[\int_0^x \frac{12C_1}{h}dx + 11x\right] + O(\alpha^4), \quad (2.27a)$$

$$p_2 - p_0 = \int_0^x \frac{6}{h^2}dx - \int_0^x \frac{12C_2}{h^3}dx - \frac{\alpha^2}{10}\left[\int_0^x \frac{12C_2}{h}dx - x\right] + O(\alpha^4). \quad (2.27b)$$

One can readily show that the term in $\alpha^2$ is positive for case (a) and negative for case (b) indicating that the presence of the fibers increases the pressure in case (a) but decreases it in case (b). The total dimensionless lift force F is obtained by integrating (2.27a) and (2.27b) over the entire surface.

$$F_1 = \int_0^1 (p_1 - p_0)dx = -\int_0^1 (1-x)\left[\frac{6}{h^2} + \frac{12C_1}{h^3} + (\frac{12C_1}{10h} + \frac{11}{10})\alpha^2 + O(\alpha^4)\right]dx, \quad (2.28a)$$

$$F_2 = \int_0^1 (p_2 - p_0)dx = \int_0^1 (1-x)\left[\frac{6}{h^2} - \frac{12C_2}{h^3} - (\frac{12C_2}{10h} - \frac{1}{10})\alpha^2 + O(\alpha^4)\right]dx. \quad (2.28b)$$

These results provide the lowest order correction to $O(\alpha^2)$ for cases (a) and (b), that arise from the difference between equations (2.8) and (2.12).

### 2.4.2 Large α limit

To examine the asymptotic behavior of the pressure distribution in the soft porous layer when $\alpha >> 1$, we notice from (2.8) that, in this limit, $f \approx \alpha^{-1}$. If we consider case (a), we find that equations (2.20a) and (2.21a) reduce to,

$$C_1 = -\frac{\int_0^1 \frac{dx}{\tilde{K}_p}}{\int_0^1 \frac{dx}{h\tilde{K}_p}}, \quad (2.29a)$$

$$p_1 - p_0 \approx -\alpha_2{}^2 \int_0^x \frac{(h + C_1)}{\tilde{K}_p h}dx. \quad (2.30a)$$

If we consider case (b), we find that equations (2.20b) and (2.21b) reduce to,

$$C_2 = \frac{\int_0^1 \frac{dx}{h\sqrt{\tilde{K}_p}}}{\alpha_2 \int_0^1 \frac{dx}{h\tilde{K}_p}} \ , \tag{2.29b}$$

$$p_2 - p_0 \approx -\alpha_2 \int_0^x \left(\frac{-\alpha_2 C_2}{\tilde{K}_p h} + \frac{1}{h\sqrt{\tilde{K}_p}}\right) dx \ . \tag{2.30b}$$

In (2.29)-(2.30) we have rewritten α in a form where we can scale this spatially varying parameter by its reference value at h = $h_2$ as $\alpha_2$. This scaling will permit us to relate both α and $K_p$ to their reference values at h = $h_2$ in plotting our results as described in the opening paragraph of the next section. Using equation (2.18) one can convert the integrals on x in (2.29) and (2.30) to integrals on h that are much easier to evaluate. For case (a)

$$C_1 = -\frac{\ln\left(1 - \frac{\ln(k)}{\ln(1-\varepsilon_2)}\right)}{e^{-\ln(1-\varepsilon_2)}\left[Ei\left[\ln\left(\frac{1-\varepsilon_2}{k}\right)\right] - Ei\left[\ln(1-\varepsilon_2)\right]\right]} \tag{2.31a}$$

in which $$Ei(x) = -\int_{-x}^{\infty} \frac{e^{-t}}{t} dt \ ,$$

and

$$p_1 - p_0 \approx -\alpha_2^{\,2} \int_1^h \frac{h + C_1}{h^2\left(1 - \frac{\ln h}{\ln(1-\varepsilon_2)}\right)} dh \ , \tag{2.32a}$$

whereas for case (b)

$$C_2 = \frac{\int_k^1 \frac{dh}{h^{\frac{3}{2}}\sqrt{1-\frac{\ln h}{\ln(1-\varepsilon_2)}}}}{\int_k^1 \frac{\alpha_2 dh}{h^2(1-\frac{\ln h}{\ln(1-\varepsilon_2)})}}\ , \qquad (2.31b)$$

and

$$p_2 - p_0 \approx -\alpha_2{}^2 \int_k^h \frac{C_2 dh}{h^2(1-k)(1-\frac{\ln h}{\ln(1-\varepsilon_2)})} + \alpha_2 \int_k^h \frac{dh}{h^{\frac{3}{2}}(1-k)\sqrt{1-\frac{\ln h}{\ln(1-\varepsilon_2)}}}\ . \qquad (2.32b)$$

In case (a) the above results are particularly useful for large $\alpha$ where p can be scaled by $\alpha_2{}^2$ and the pressure profiles collapse into a single curve for a given $h_2$ for each value of the compression ratio k as deduced from (2.32a). In case (b) for $\alpha_2 >> 1$ the pressure asymptotically decays to zero as $\alpha_2{}^{-2}$. These results are shown and discussed in the next section.

## 2.5 Results

We shall explore the behavior of both cases (a) and (b) over a wide range of $\alpha_2$ and compression ratio, $k=h_1/h_2$. The length L of the planing surface does not appear explicitly, but appears in the dimensionless expressions for the pressure and force per unit width of planing surface. The characteristic pressure and lift force F per unit width are given by $\mu UL/h_2{}^2$ and $\mu UL^2/h_2{}^2$, respectively. The dimensionless height h is scaled by the height $h_2$ at the trailing edge in case (a) and the leading edge in case (b). If $h_2$ is arbitrarily fixed at 1 cm then a reference $\alpha_2$ can be defined by $h_2/\sqrt{K_{p2}}$ where $K_{p2}$ is the reference Darcy permeability at this reference height.

For h >1, $\alpha$ varies with x since both h and $K_p$ are varying, but $\tilde{K}_p$ is only a function of h for each value of k as shown in Fig. 2.3. Thus, to employ the results in Fig. 2.3 one simply specifies $\alpha_2$, prescribes the fiber radius, and finds $K_{p2}$ from figure 2.2. The fiber radius $r_f$ used in all our calculations, is 5 μm. This is characteristic of the polyester fibers used in the applications in section 2.6.

In classical lubrication theory for a slipper bearing one examines the relative motion of an inclined planar surface and a horizontal planar surface. Figures 2.4a, b show that the solution for the pressure distribution and lift force are independent of which boundary is moving, for reasons already discussed, and there is an optimum compression ratio, $k=h_1/h_2=2.2$ for maximum lift. As already noted, the solution for the pressure distribution in case (a) is the mirror image of that in case (b) because the inclination of the upper boundary is reversed. This symmetry is lost if the intervening space is filled with a soft porous material.

Typical solutions for the pressure distribution beneath the planar surface when the upper boundary moves (case a) and when the lower boundary moves (case b) are shown in figures 2.5a and 2.5b for a compression ratio k=2 for values of $\alpha_2$ in the range of $0 < \alpha_2 < 3$. In figure 2.5a the thickness $h_2$ and $\alpha_2$ at the trailing edge are prescribed. The slope of the plane $(h_1-h_2)/L$ is given in terms of the matrix compression ratio, $k=h_1/h_2$, as $(k-1)h_2/L$, see figure 2.1a. In figure 2.5b the thickness $h_2$ and $\alpha_2$ at the leading edge are prescribed. The slope of the plane $-(h_1-h_2)/L$ is given in terms of the matrix compression ratio, $k=h_1/h_2$, as $(1-k)h_2/L$, see figure 2.1b.

As can be seen in figure 2.5a when the inclined upper boundary moves the dimensionless pressure increases rapidly for $\alpha_2 > 1$ with the peak value of pressure being more than four fold greater for $\alpha_2 = 3$ than at $\alpha = 0$. In contrast, when the horizontal lower boundary moves, the pressure profiles decay slowly for $\alpha_2 > 1$. In figures 2.6a, b the corresponding pressure profiles are shown for a large compression ratio k =10. A qualitatively similar behavior is observed except that in both figures there is a pronounced shift of the pressure maximum toward the trailing edge at x = 0 for case (a) and the leading edge at x = 1 for case (b). Note the five fold difference in scales between figures 2.6a and 2.6b where the results for $\alpha = 0$ are the same, but mirror images of one another. In view of the large pressure gradients near the leading and trailing edges observed for large values of k, one needs to be concerned about the assumption that the pressure is a constant across the porous layer in these regions. The length of these regions is of order H, whereas the length scale of the region with the steep pressure gradient is of order 1/k. Thus, for the vertical pressure gradient to be neglected at the leading and trailing edges, we require L/H > k. The same approximation also applies for the classical lubrication results in figure 2.4.

Figure 2.7 shows the dimensionless force as a function of k. We note that in figure 2.7a there is an optimum compression ratio for the dimensionless force at k=2.2 when $\alpha$=0, but when $\alpha$ increases this maximum increases in magnitude and shifts to values of k > 2.2. In case (b), in figure 2.7b, there is the same maximum at k=2.2 when $\alpha$=0, but the maximum decreases with increasing $\alpha$. To examine the asymptotic behavior for large $\alpha_2$ we have rescaled the dimensionless pressure by $\alpha_2^2$ in equation (2.33a) for case (a), since our asymptotic analysis in section 2.2.4

indicates that for case (a) the pressure and hence the lift force increase as $\alpha_2^2$. The analysis indicates that with this new scaling the new dimensionless pressure and lift force curves collapse into a single curve for large $\alpha_2$. The results shown in figure 2.8a clearly indicate that there is very little difference between the curves for $\alpha_2$ = 20 and 100 and, thus, for most practical purposes the simplified asymptotic solution can be applied for $\alpha_2 > 20$. In contrast, the pressure disturbance and lift force for case (b), lower boundary moving, die out rapidly for $\alpha_2 >> 1$, as shown in figures 2.9a, b.

Figures 2.10a, b show the velocity profiles in the fiber matrix for representative $\alpha_2$ for cases (a) and (b), respectively, for k=4. Three sets of profiles are shown in each panel, which corresponds to the leading and trailing edges and the position where the pressure reaches its maximum. For comparison is the prediction of classical lubrication theory, $\alpha$=0, is also shown. We note that at the position where the pressure gradient is zero in classical lubrication theory the velocity profile is linear, but as the fiber interaction layer parameter $\alpha_2$ increases, thin fiber interaction layers develop near both the upper and lower boundaries provided there is a non-vanishing bulk flow in the matrix. In marked contrast to classical lubrication theory, where there is a uniform shear flow at the pressure maximum, it is the bulk flow that vanishes at the location where dp/dx = 0 for large $\alpha_2$, since the local pressure gradient is the driving force for the flow in the interior of the fiber layer in this limit and this gradient vanishes at the maximum pressure. When there is no bulk flow, u = -1 since this is the velocity at which the fiber layer is moving to the left in the steady frame. In case (b), where the lower boundary is moving, an increasingly smaller amount of fluid is dragged through the leading

edge as $\alpha_2$ is increased since the fiber interaction layer near the lower boundary grows thinner and the bulk motion in the interior dies out for $\alpha_2 >> 1$. In sharp contrast to classical lubrication theory, where the motion of lower boundary is transmitted as a shear force at the upper boundary, the presence of the fiber layer shields the upper boundary and serves as a barrier to greatly retard the flow. In case (a) large pressure gradients are generated in the interior of the fiber layer as $\alpha_2$ increases. Basically, the inclined upper boundary is pushing fluid ahead of it in the unsteady reference frame in figure 2.1a creating a bulk flow in the fiber layer, which would vanish if this plane were not sloped upward. A curious feature for case (a), first pointed out in F&W, is that in the unsteady reference frame this flow is leaving at both the leading and trailing edges and a dividing streamline develops beneath the inclined plane whose location depends on the compression ratio k.

## 2.6 Discussion

It may seem counter-intuitive, at first time, that the solutions for cases (a) and (b) herein should differ so greatly from those of classical lubrication theory for a slider bearing when $\alpha$ increased. However, the presence of the porous medium introduced an additional $\alpha^2$ term in equation (2.3) when a steady-velocity transformation was introduced. The governing equations (2.1) and (2.3) thus differed depending on whether the porous media layer was attached to the lower or upper boundary. In marked contrast, in classical lubrication theory a simple transformation of coordinates leads to the same boundary value problem. Also, the numerical solutions in Feng & Weinbaum (2000) exhibit a lift force that monotonically increased with increasing k and the reason for the loss of the

maximum at k=2.2 were not clear. This result is now clearly explained by the results in figures 2.7a and 2.8b in which $h_2$, the height of the trailing edge in case (a) is fixed rather than $h_1$ at the leading edge. One observes there is an optimum compression ratio for the dimensionless force at k=2.2 when $\alpha$=0, but when $\alpha$ increases this maximum increases in magnitude and shifts to values of k > 2.2. This maximum is also present when the lower boundary is moving, but decays as $\alpha_2^2$ for large $\alpha_2$ as shown in figure 2.9b.

The results in figures 2.8 and 2.9 provide the key insight into the difference in behavior between red cells moving in single file in small capillaries and narrow glass tubes of the same diameter, as described in section 2.1. The value of $\alpha$ has been estimated as 160 for a 0.5 μm thick endothelial glycocalyx layer in F&W. The results in figure 2.8a,b show that for this value of $\alpha$ one has approached the limiting behavior for both the pressure and the lift force exerted on the red cell membrane. Greatly enhanced lift forces separating the red cell and endothelial cell membranes will be present at very low velocities. These forces are more than four orders of magnitude greater than classical lubrication theory without the fiber layer present. Thus, the red cell will be displaced from the capillary wall when it is moving only a few μm/s, a speed which is much less than the 100 μm/s velocity that the red cell typically experiences in single-file flow in skeletal-muscle capillaries. This lift force is very important at arteriolar sphincters which control the distribution of flow in capillary networks. At these sphincters the vessels can narrow to as little as 4-5 μm diameters and the velocity of the red cell will slow to a few μm/s. The lift forces described herein prevent the glycocalyx from being crushed and the formation of adhesive interactions between membrane proteins in the red cell and endothelial

membranes that could lead to the arrest of the microcirculation. The behavior of red cells in class tubes illustrated in figure 2.9 is strikingly different. In this case the glycocalyx layer on the red cell membrane, whose existence has been hypothesized but not yet clearly demonstrated, generates a lift force that is nearly entirely attenuated for $\alpha > 20$. Thus, a very thin fiber layer, which could be an order of magnitude smaller than the endothelial glycocalyx layer, would nearly entirely shield the red cell membrane from its motion relative to the wall of the glass tube. Therefore, tightly fitting red cells fill nearly the entire glass tube and experience much less resistance than red cells moving in capillaries with the same diameter as described by Pries *et al.* (1994, 2000).

The most important new result is the demonstration that the dimensionless lift force per unit width $h_2^2F/\alpha_2^2\mu L^2U$, which can also be written as $K_{p2}F/\mu L^2U$, approaches a simple asymptotic behavior for large $\alpha_2$ as shown in figure 2.8b. This result has important implications for generating lift forces on inclined surfaces moving over a stationary porous media that vastly exceed those of classical lubrication theory provided leakage of pressure at lateral edges can be eliminated. This was realized in F&W and Wu *et al.* (2004), but an inexpensive, soft, durable fibrous material had not yet been identified. The properties of such a material are explored in Mirbod, Andreopoulos & Weinbaum (2009b). This material is a random fiber matrix with nearly uniform 10 μm diameter polyester fibers with a trace of silk. $K_p$ for these fibers is well described by an empirical Carman-Kozeny relation for porous media. The experiments in Mirbod *et al.* (2009b) show that the length of fiber per unit volume is 5950 cm/cm$^3$ in its undeformed state. This corresponds to a solid fraction of 0.0045 and a value of $K_p$ of 3.4 x $10^{-5}$ cm$^2$ using figure 2.2. It is a

simple matter to calculate the lift force on a planing surface for any value of the compression ratio k using figure 2.8b. As a practical matter a light highly porous protective screen rests on top of the porous layer. This is tethered to the impermeable sidewalls of the channel to reduce shear deformation.

To illustrate the above application consider a planform with the typical dimensions of a toboggan, 2 m long and 0.5 m wide or a planning area of 1 $m^2$. Assume that $h_1$ at the leading edge is 10 cm and $h_2$ at the trailing edge is 5 cm or k =2. If the layer compresses in a locally uniform manner the solid fraction at the trailing edge will be doubled or $(1-\varepsilon) = 0.009$. From figure 2.2, $K_{p2} = 1.57\text{x}10^{-9}$ $m^2$ and $\alpha_2 = 1260$. The curve for $K_{p2}F/\mu L^2U$ for $\alpha_2 = 1260$ is nearly indistinguishable from the curve for $\alpha_2 = 100$ in figure 2.8b. For k=2, $K_{p2}F/\mu L^2U$ is 0.037. All the parameters in the dimensionless expression for the lift force are now known except for U, but the latter scaling is linear. Using the value of μ for air at 20 $^0$C, which is $1.73\text{x}10^{-5}$ $Ns/m^2$, one finds that F = 815U in Nm/s. At a velocity of 10 m/s this toboggan can support 8150 N or 0.83 metric tons. This force due to the trapped air in the porous material is many times the lift force of the solid phase because the material has the softness of cotton. It is hard to imagine that so much weight can be supported by a material with the properties of a common pillow with relatively little compression.

As first proposed in Wu *et al.* (2004) such large lift forces could potentially be used in commercial transportation. In Mirbod, Andreopoulos & Weinbaum (2009b), we explore this concept for a 200 passenger jet train weighing approximately 70 metric tons, supported by a 30 x 3 m planform that glides on a 20 cm thick soft porous track in a channel a few tens of centimeters above the surface of the ground.

The calculations in Mirbod *et al.* (2009b) predict that the train would become airborne at velocities less than 5 m/s with only a 20 percent compression of the fiber layer (4 cm) at the trailing edge of the planform for lift-off. For such small compressions the fiber phase provides less than one percent of the total lift and friction forces are negligible compared to aerodynamic drag. One finds that this airborne jet train needs far less powerful jet engines and consumes far less energy than commercial aircraft with the same passenger load since there is no need to climb to cruising altitude and lift induced drag is negligible since the maximum angle of attack is $< 0.1$ degrees.

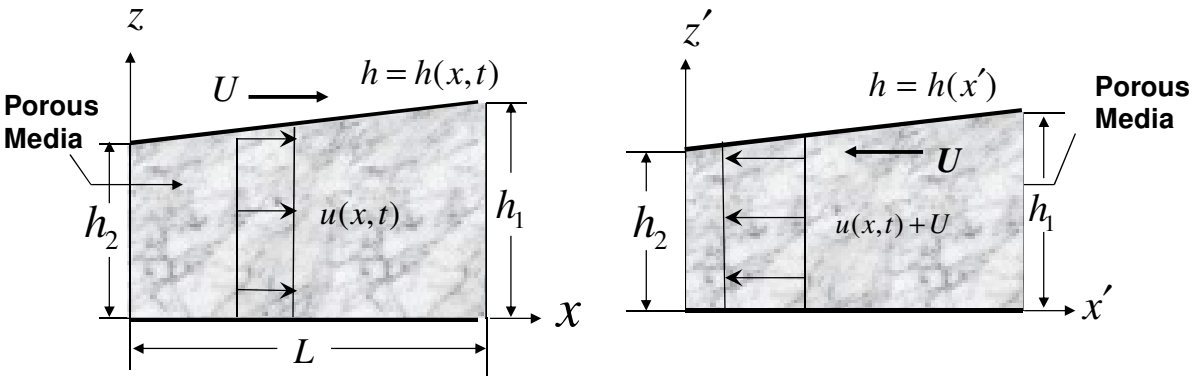


Figure 2.1 Schematic illustration of the present model for sliding motion of a rigid surface over or beneath a thin layer of a soft fiber matrix. (a) Inclined planar surface moves over a stationary matrix attached to the lower boundary. (b) Horizontal planar surface moves beneath a stationary matrix attach to the inclined upper boundary.

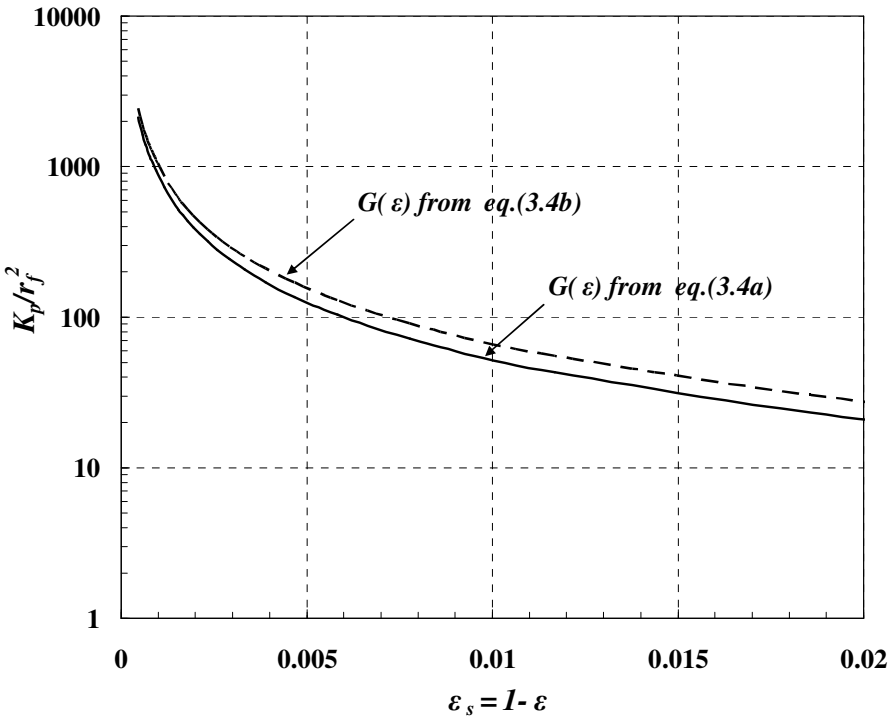


Figure 2.2 Comparison of $\frac{K_p}{r_f^{\,2}}$ using equations (2.16a) and (2.16b) for the Carman-Kozeny constant $G(\varepsilon)$.

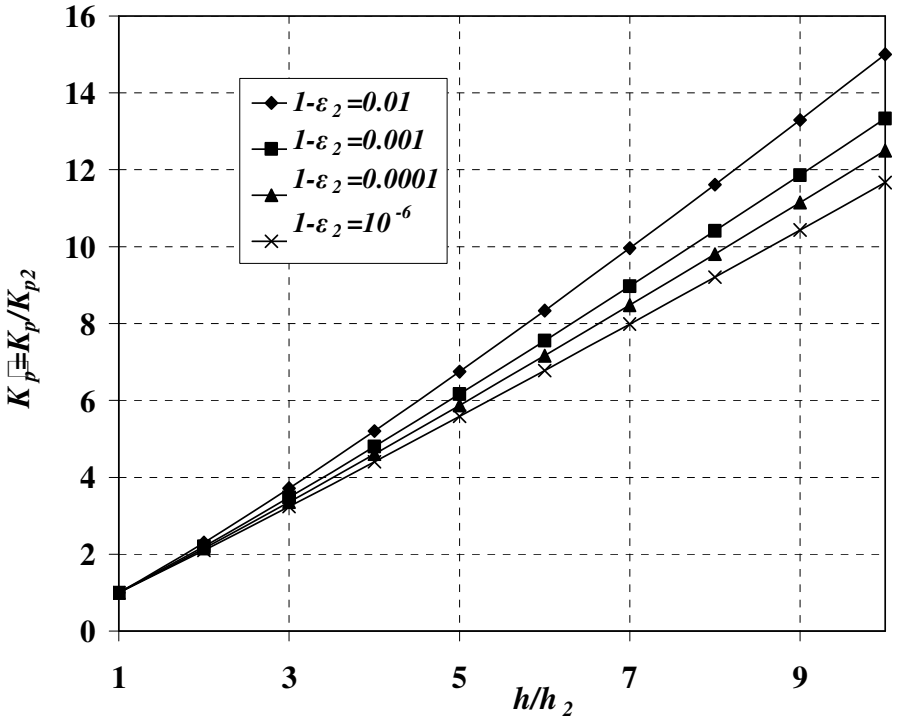


Figure 2.3 Variation of $\tilde{K}_p = \frac{K_p}{K_{p2}}$ as a function of $h/h_2$ for representative values of $(1-\varepsilon_2)$.

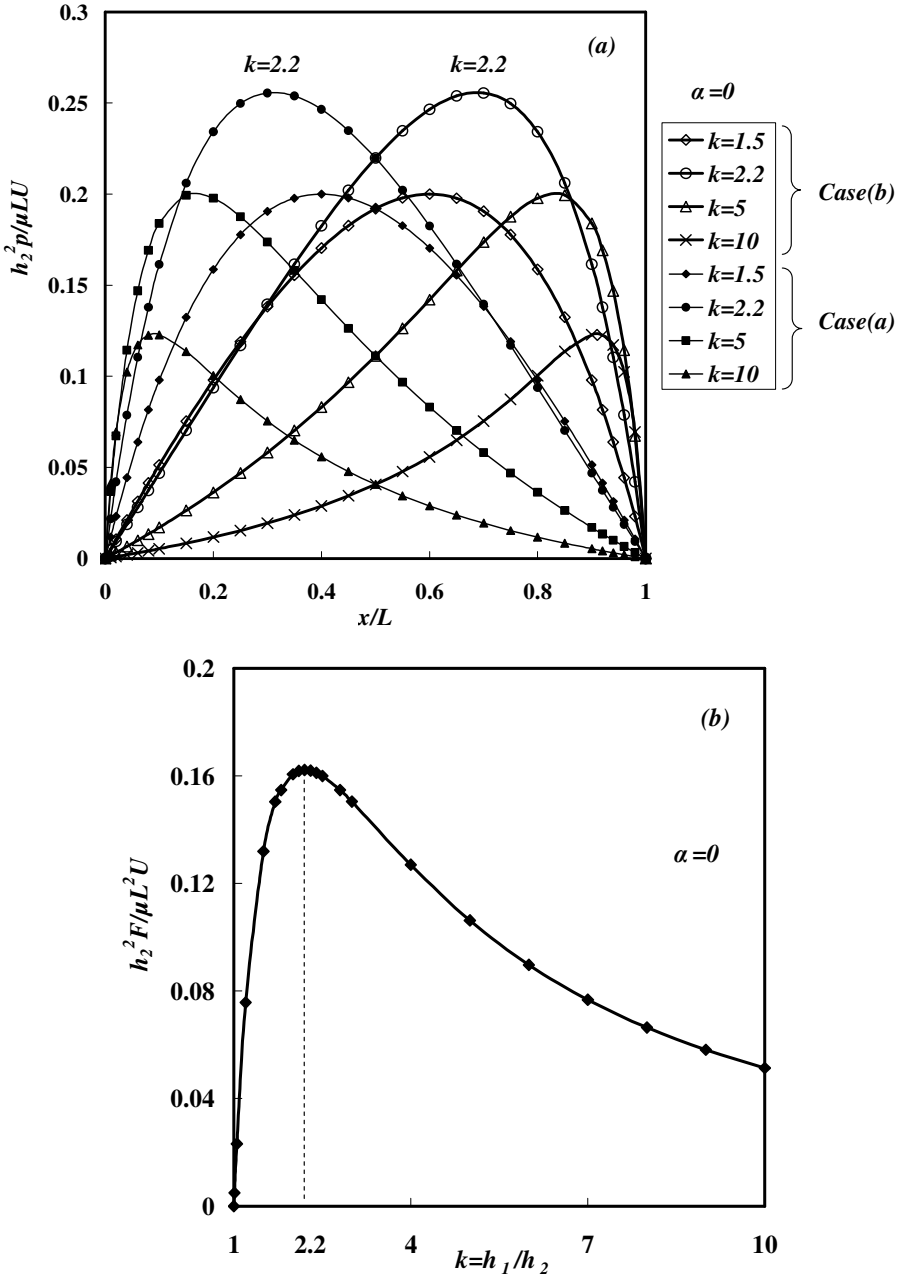


Figure 2.4 Classical lubrication theory $\alpha$=0. (a) Dimensionless pressure distribution for a slipper bearing. (b) Dimensionless lift force as a function of compression ratio k showing a maximum at k=2.2.

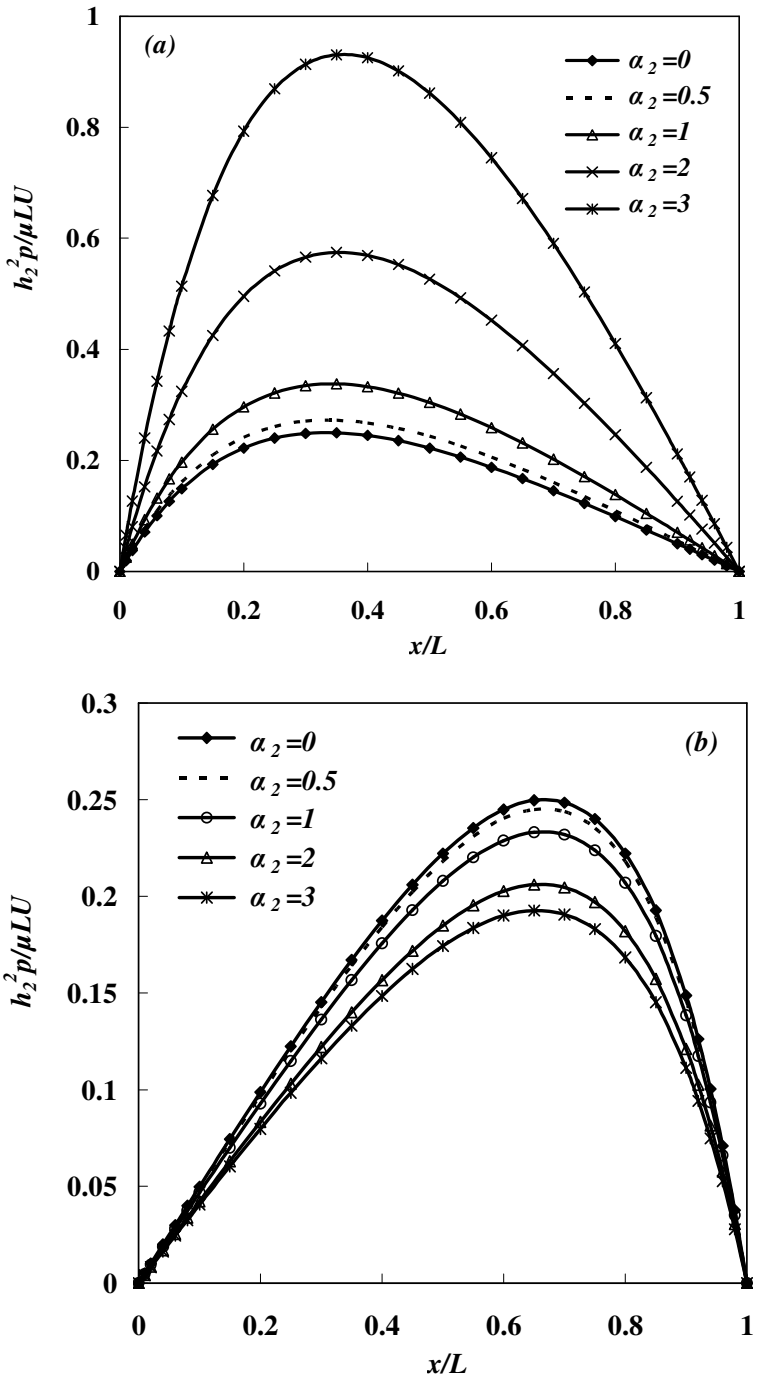


Figure 2.5 Dimensionless pressure distribution for compression ratio k = 2: (a) Inclined upper boundary moves. (b) Horizontal lower boundary moves. Dashed line solution for small α, equation (2.27a) in case (a), equation (2.27b) in case (b).

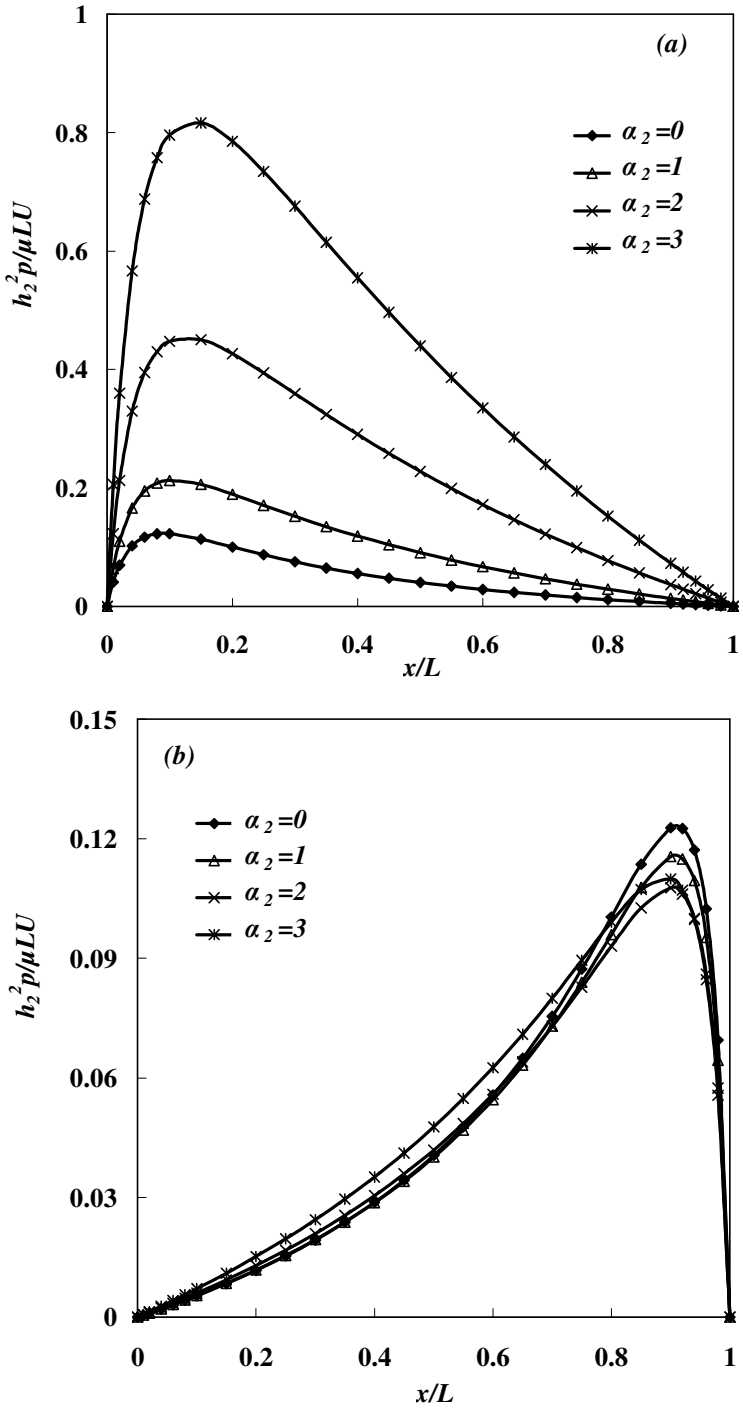


Figure 2.6 Dimensionless pressure distribution for compression ratio k=10: (a) As the upper boundary moves. (b) As the lower boundary moves.

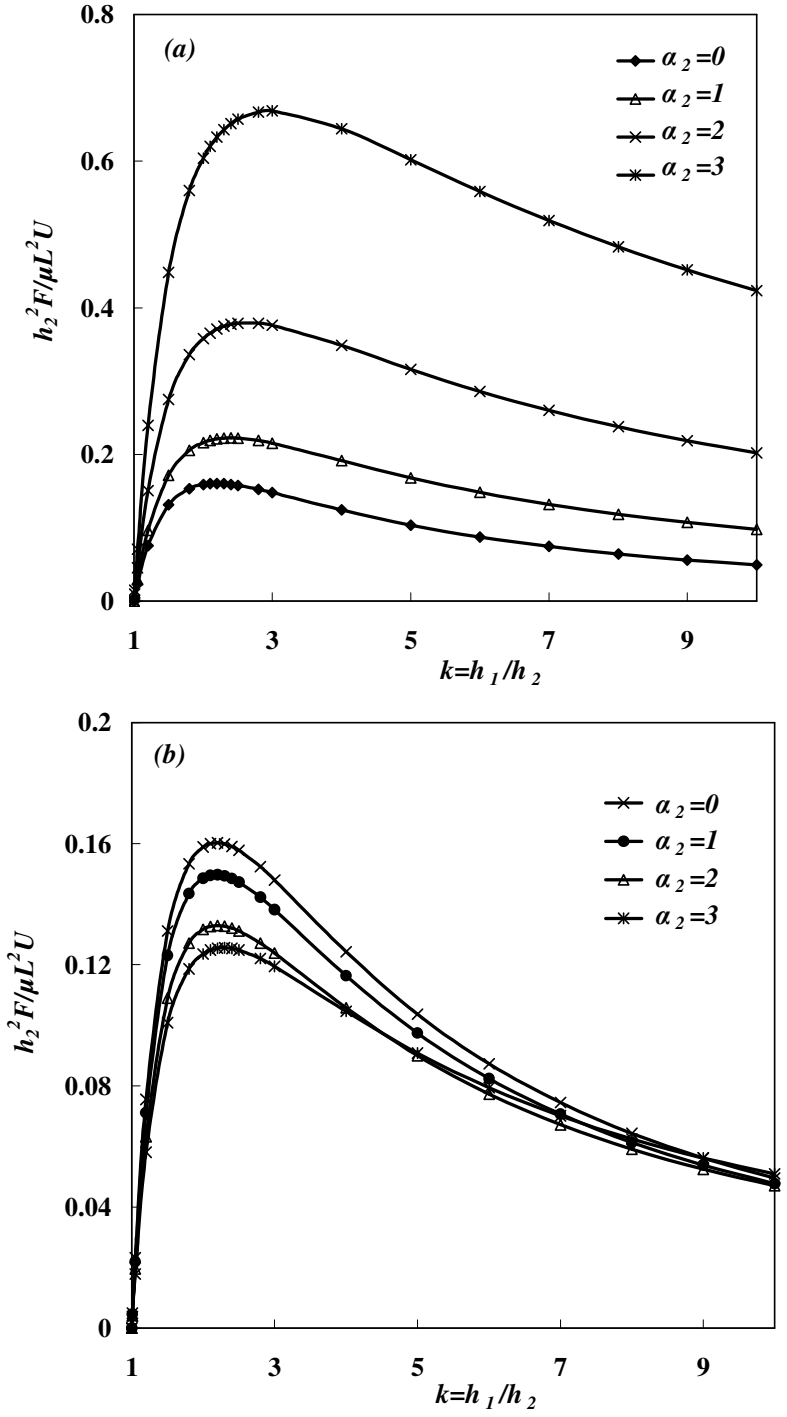


Figure 2.7 Dimensionless lift force as a function of compression ratio k. (a) Inclined upper boundary moves, (b) Horizontal lower boundary moves.

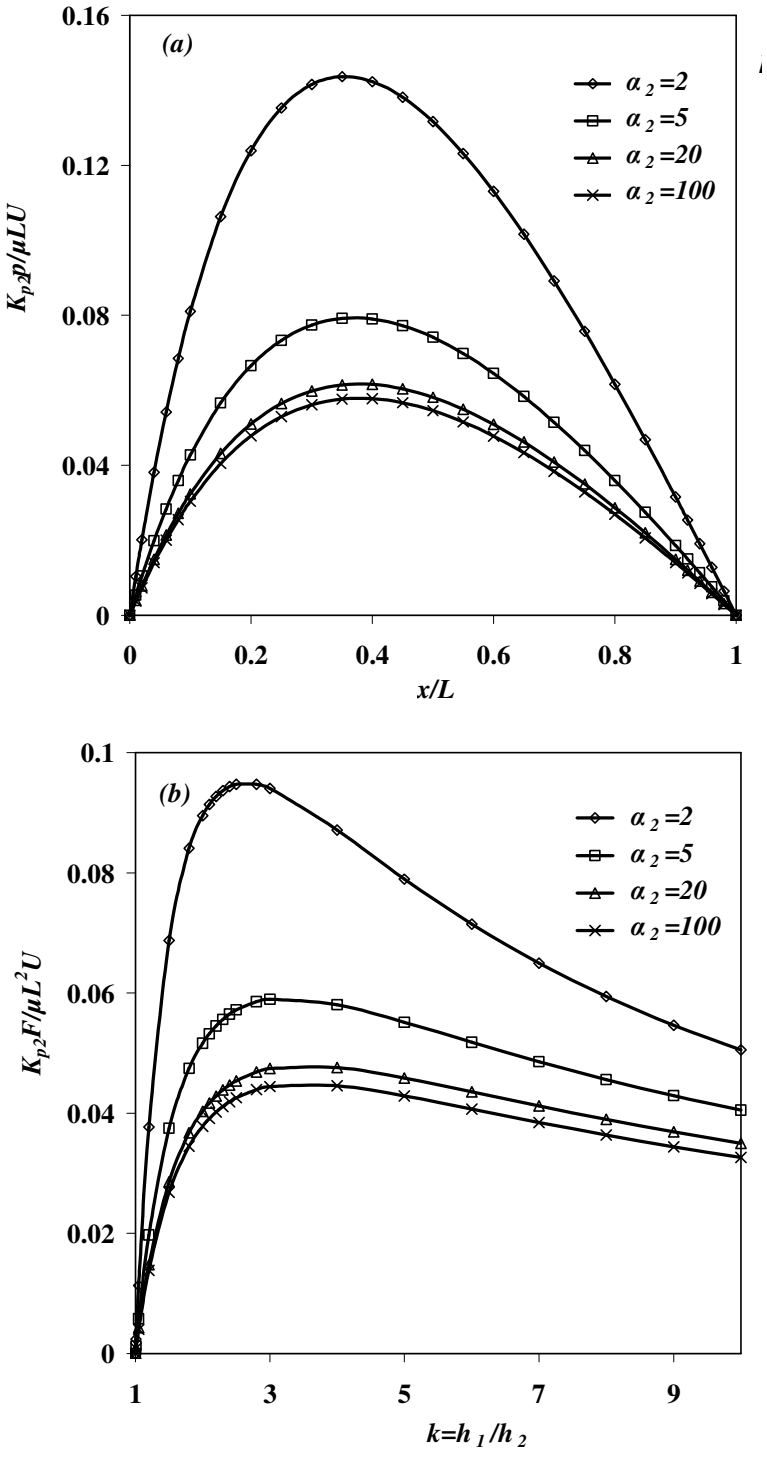


Figure 2.8 Asymptotic behavior ($\alpha_2$ >>1) for pressure distribution (a) and lift force (b) when the inclined upper boundary moves (case a).

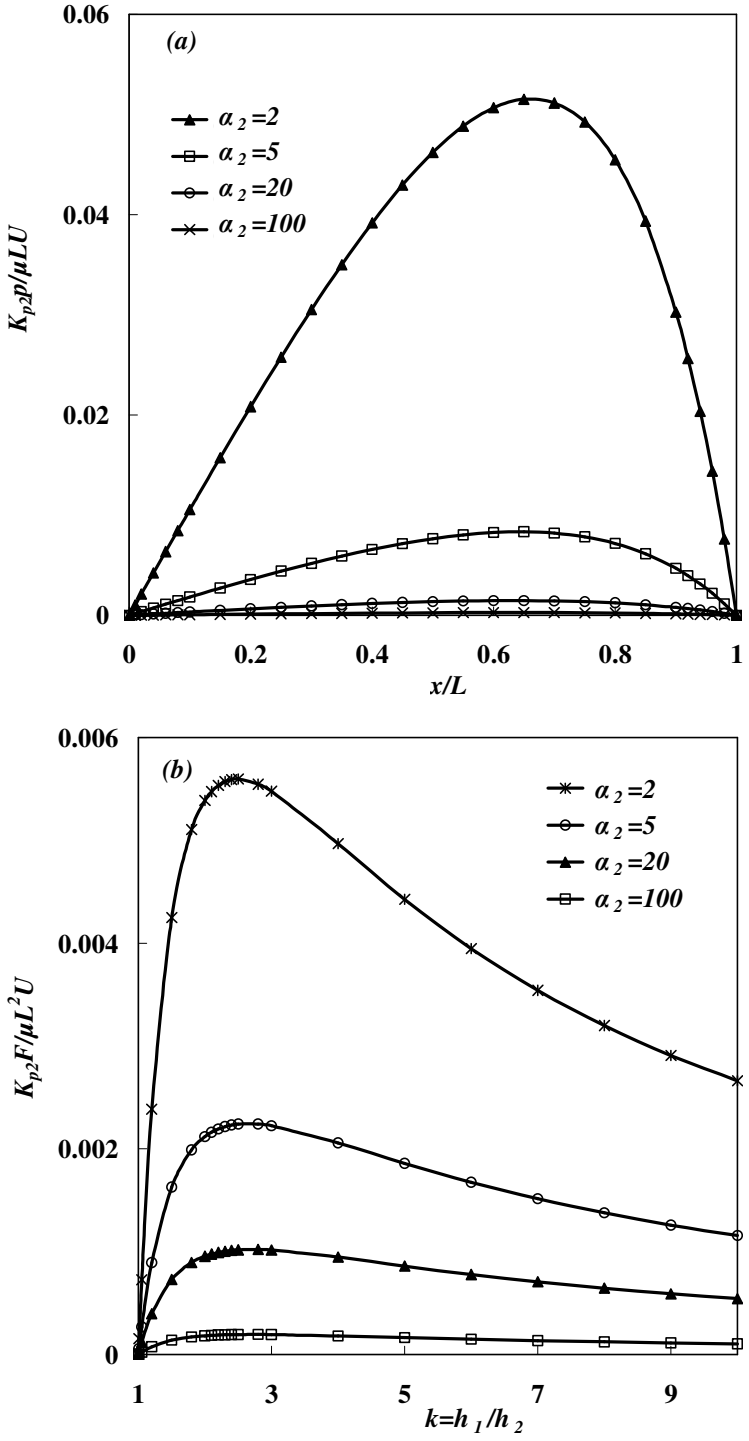


Figure 2.9 Asymptotic behavior ($\alpha_2$ >>1) for pressure distribution (a) and lift force (b) when the horizontal lower boundary moves (case b).

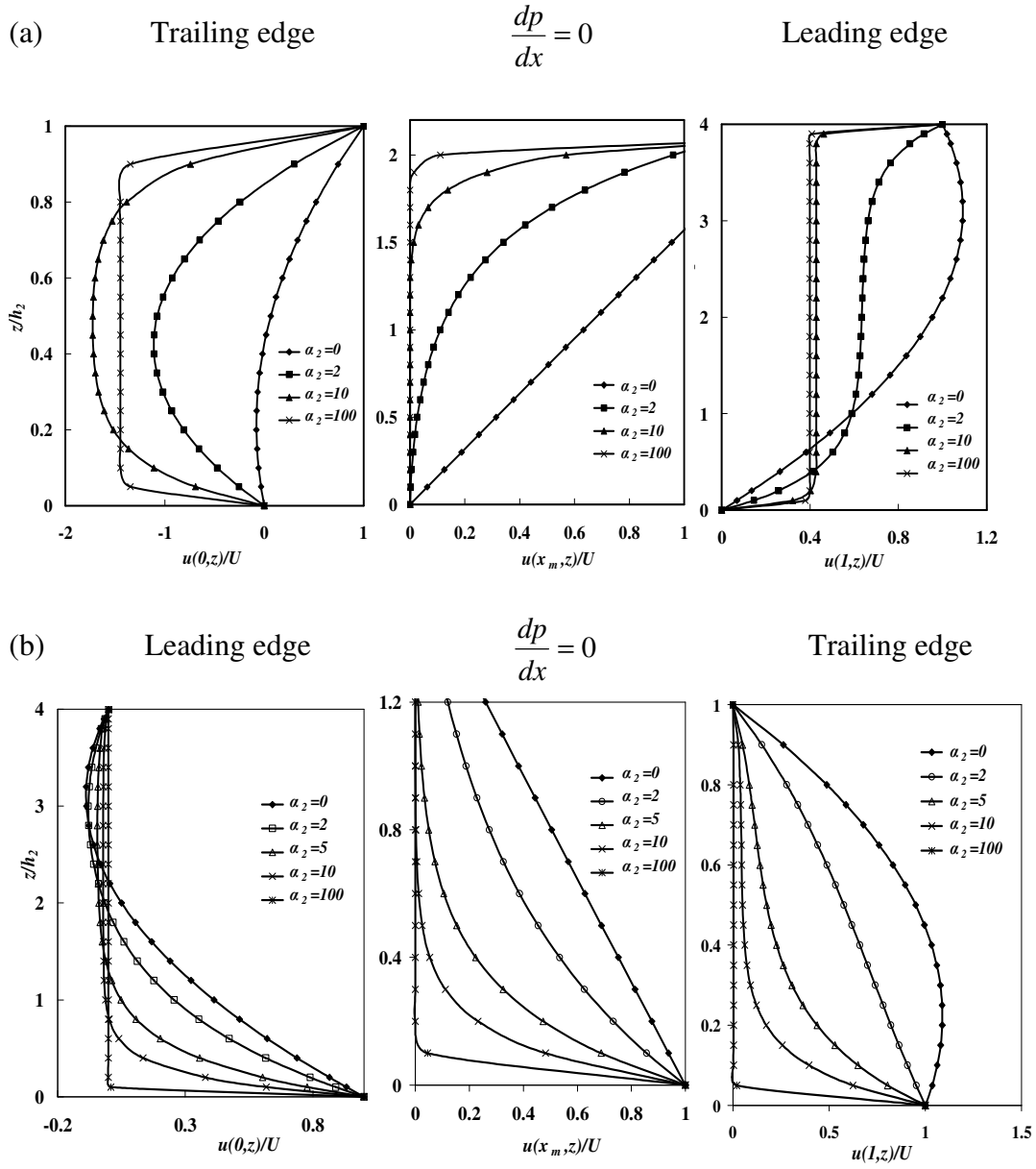


Figure 2.10 Panel (a) velocity profiles in fiber layer for representative $\alpha_2$ when the upper boundary moves in the transformed steady coordinate frame where the upper boundary is stationary and the lower boundary with attached fiber layer moves beneath it, case (a). Panel (b) velocity profiles in fiber layer for representative $\alpha_2$ when the lower boundary moves, case (b). Three sets of profiles are shown which correspond to the leading and trailing edges and the position where the pressure reaches its maximum, $x_m$. (k = 4 for all profiles)

# Chapter 3 Application of soft porous materials to a high speed train track

## 3.1 Introduction

In this chapter we explore the quantitative feasibility and performance of an airborne jet train (AJT) that would fly on a soft porous track (SPT) within centimeters of the earth's surface at speeds approaching current commercial jet aircraft. The AJT employs a lift mechanism first proposed in Feng and Weinbaum (2000) and a nearly frictionless track suggested in Wu, Andreopoulos and Weinbaum (2004). The proposed design would allow lift-off at velocities of < 5 m/s (18 km/hr) and a cruising velocity approaching 700 km/hr with jet engines of 10,000 lbf thrust, about 1/5 that of a 200 passenger commercial jet aircraft. This jet train would require a fraction of the fuel expenditure of commercial jets, and be much less sensitive to weather conditions, since it is ground based and partially protected from the environment. The aero-mechanical technology involved is less sophisticated than maglev trains and requires a track and levitation system that should be far less costly than maglev systems operating in either the electromagnetic (EMS) or electrodynamic (EDS) modes.

Existing maglev technology has provided a very interesting alternative to jet planes but is very costly, requires sophisticated active electronic stabilization systems to maintain the train at a constant distance (approximately 1.5 cm) from the track and the weight and bulkiness of the electromagnets are major design issues. While EMS maglevs can levitate at a standstill, the EDS mode, like our AJT, requires wheels at low velocities to support the weight of the train though the speed to do this for our proposed AJT is remarkably low. Having wheels in the future

could prove to be an advantage if it could permit access to existing traditional train tracks in urban hubs. The AJT could then taxi at low speed to its specially designed SPT, much like airplanes taxi to runways.

The basic idea for obtaining greatly enhanced lift using soft porous media is proposed in Feng and Weinbaum (2000) and is described more fully in the next section. In essence, using a generalized lubrication theory based on effective medium theory (Brinkman equation), one can show that much larger pressures can be generated beneath a moving inclined planar surface if a soft porous material is confined between this inclined moving surface and a stationary flat lower boundary to which the porous layer is firmly attached. The magnitude of this pressure increase depends on two dimensionless parameters, $\alpha = H/\sqrt{K_p}$, where H is the characteristic thickness of the layer and $K_p$ is the Darcy permeability, the aspect ratio of the inclined planar surface, L/W, where L is its length and W its width, and the tilt angle of the planform. It is shown in Feng and Weinbaum (2000) that the pressure and lift force increase as $\alpha^2$ and this enhanced lift is attenuated as $(L/W)^{-2}$ as the aspect ratio is increased due to the pressure loss at the lateral edges of the planform. This theory was initially developed in Feng and Weinbaum (2000) to explain why red cells would either invade the glycocalyx layer (layer of adhered proteins and glycoproteins coating the endothelial lining of our capillaries, reviewed in Weinbaum, Tarbell and Damiano 2007) when the red cell velocity decreased to < 20 μm/s or popped out of the layer when the cell started from rest and its velocity increased to this same value (Secomb, Hsu and Pries 2001). A surprising finding was that the value of $\alpha$ for a human being skiing or snowboarding on fresh powder,

100-400, bracketed the value for a red cell even though they differed in mass by 15 orders of magnitude.

The last observation was the catalyst for a series of papers, Wu, Andreopoulos and Weinbaum (2004), Wu, Andreopoulos, Xanthos and Weinbaum (2005), Wu, Igci, Andreopoulos and Weinbaum (2006), in which the authors started to explore the combined effects of the air and solid crystal phases in skiing and snowboarding and the importance of the aspect ratio in maintaining the enhanced lift. In Wu, Andreopoulos and Weinbaum (2004); Wu, Andreopoulos, Xanthos and Weinbaum (2005) experiments were performed using a porous walled piston-cylinder apparatus to measure the characteristic time for the decay of the excess pore pressure during skiing for different snow conditions. These results were then applied in Wu, Igci, Andreopoulos and Weinbaum (2006) to theoretically predict the fraction of the total lift force provided by the air that was transiently trapped beneath a ski or snowboard. Typically, one finds that for fine powder about one half of the total lift for a snowboard comes from the air and about 40% for a ski when traveling at 10 m/s. However, both are highly inefficient in this regard since most of the excess pore pressure is drained at the lateral edges and one is able to take advantage of only a small fraction of the total lift that is possible. It was this last observation that led to the design of a soft porous, nearly frictionless track with impermeable sidewalls that is explored in the present chapter.

The feasibility of designing a new type of train track with a restorative porous material akin to down feathers in pillows, where this lateral leakage is abrogated and much heavier loads accommodated, was first proposed in Wu, Andreopoulos and Weinbaum (2004) the porous material was not identified or characterized, the

stability of the train car and its performance were not examined or was a possible propulsion system discussed. These three principal questions are the primary focus of the present chapter. This analysis has led to the design of the AJT described herein and its theoretically predicted performance.

## 3.2 Basic Design Criteria

The key insights into the design criteria for the new track can be gleaned from figure 15 in Feng and Weinbaum (2000), see Fig. 3.1. The three curves in this figure quantitatively illustrate the importance of the three key dimensionless parameters, $\alpha$, L/W, and $k = h_1/h_2$, a tilt parameter which describes the ratio of the fiber layer thicknesses, $h_1$ and $h_2$, at the leading and trailing edges. L/W= 10 was chosen to lie midway between a ski and a snowboard and L/W = 0 corresponds to a red cell that is completely surrounded by a thin glycocalyx layer that is attached to the endothelial lining of a capillary. For a red cell there are no lateral edges since the outer boundary closes on itself. One notes that the dimensionless lift force per unit width W, $Fh_1^2/\mu UL^2$, where $h_1 = H$ is the undeformed layer thickness, is nearly constant for $\alpha < 1$, but for $\alpha > 10$ increases as $\alpha^2$ independent of the value of k or L/W. Mirbod, Andreopoulos and Weinbaum (2009a) show that in this large $\alpha$ limit that if the pressure is scaled by $\alpha^2$, the resulting dimensionless pressure and lift force $Fh_1^2/\alpha^2\mu UL^2 = FK_p(H)/\mu UL^2$ collapse into a single curve which is a function of $k = h_1/h_2$, but independent of the layer thickness H for a prescribed $K_p(H)$. Thus, for a given $K_p(H)$ the thickness of the layer does not enter into the solution for the lift.

One also notes that for any value of $\alpha$ in Fig. 3.1 the dimensionless lift force is approximately 100 times greater for L/W = 0 than for L/W = 10 and decreases as $(L/W)^{-2}$. These results were obtained for a porous media comprised of a doubly periodic array of parallel circular cylindrical fibers which compress uniformly in the vertical direction. In Feng and Weinbaum (2000) the Darcy permeability is described using a numerical Stokes solution for flow transverse to the fiber axes taking into account the change in vertical spacing of the fibers as the fiber layer compresses.

It is clear from these results that the red cell is able to optimize its lift and will be a far better skier than a human, since there is no pressure loss at lateral edges. This is the behavior that one would like to capture in our track, small deformations and minimal lateral leakage of pressure. Small deformations allow for a nearly complete restoration of the layer after the passage of the train and the small compressive force on the fibers greatly reduces sliding friction. In our theory for skiing and snowboarding in Wu, Igci, Andreopoulos and Weinbaum (2006) nearly half of the lift force, as noted earlier, came from the compression of the solid crystal phase. In our train track we would like to reduce this component dramatically to less than 0.2 percent of the total lift and, hence, for a sliding friction coefficient of 0.2, a sliding friction force of less than 1/2500 of the lift. Finally, the simplest way to greatly reduce lateral leakage is to place the soft fiber layer in a channel with impermeable sidewalls that permit free gliding, but are in near contact with the edge of the planing surface. This sealing can also be enhanced by narrow felt slider strips on the edges of the highly porous, light weight plastic protective screen that rests on top of the porous layer. This screen, which is attached from below to the channel

walls, is also used to minimize shear deformation of the porous layer and protect the fibers from wear, tear and debris.

## 3.3 Theoretical methods

### 3.3.1 Excess pore pressure and aerodynamic lift force

In Figure 3.2a we present the basic flow geometry for the planar lifting surface. An inclined planar lifting surface of length L is moving to the right with velocity U compressing a soft porous material in a channel of width W with impermeable sidewalls. The fiber layer is firmly attached to the flat, rigid, bottom boundary of the channel. Due to the tilt of the inclined moving upper boundary air is also pushed through the fiber layer in the x direction with a velocity u(x,t) that depends on the tilt parameter $k = h_1/h_2$ and the local variation of the Darcy permeability $K_p$. $K_p$ is assumed to vary only with x since the compression in the vertical y direction is assumed to be uniform. This is equivalent to having the local vertical displacement of the fiber layer vary linearly with distance from the bottom boundary. Due to the impermeable sidewalls one needs to consider only unidirectional flow in the x direction. Furthermore, since both L and W are >> H, the characteristic thickness of the layer, one can apply the classical approximation in lubrication theory that the pressure is constant across the local fiber layer thickness. The equation governing this flow is derived in Feng and Weinbaum (2000) for an arbitrary value of the dimensionless permeability parameter $\alpha$, equation (2.25) in Feng and Weinbaum (2000). However, since $\alpha$ is of order $10^3$ and thus >>>1, one can employ a much simpler asymptotic analysis. In this limit, the complicated velocity profile u = u(x,y,t) in the porous layer becomes

independent of y and reduces to a plug flow. Basically, the thickness of the fiber interaction boundary layers at the top and bottom boundaries are of order $\sqrt{K_p}$ and for $\alpha = H/\sqrt{K_p} = 1000$ and H = 20 cm, $\sqrt{K_p} = 0.2$ mm. Thus, outside these thin layers the velocity is locally uniform across the height h(x,t) and u = u(x,t). One essentially has a slip velocity at the confining boundaries which is typical of a Darcy flow. Note that a non-linear Forchheimer term describing inertia is not needed since, as we will discuss later, both the Reynolds number based on the fiber diameter and the fiber pore size are in the low Re regime with a maximum value of only 1.2.

The problem sketched in Figure 3.2a is inherently unsteady in the coordinate system of the stationary lower boundary with its attached fiber layer and the local height of the inclined upper boundary is time varying, h=h(x,t). However, we can transform the flow into a steady reference frame where the observer sits on the inclined upper boundary and the lower boundary with its attached fiber layer moves beneath it with velocity $\boldsymbol{U} = -U\boldsymbol{i}$ as observed in Figure 3.2b. The Darcy equation, $u(x) = -(K_p/\mu)dp/dx$, depends on the frame of the observer since it describes the relative motion $\boldsymbol{u} - \boldsymbol{U} = (u + U)\boldsymbol{i}$ of the fluid and solid constituents where $\boldsymbol{u} = u\boldsymbol{i}$ is the absolute velocity of the air in the steady transformed (x′,y′) coordinate system. The generalized Darcy equation describing this relative motion in the (x′,y′) coordinate system is given by

$$u + U = -\frac{K_p}{\mu}\frac{dp}{dx'}, \tag{3.1}$$

Introducing the dimensionless variables

$$\tilde{x} = \frac{x'}{L},\ \tilde{h} = \frac{h}{H},\ \tilde{P} = \frac{pK_p(H)}{\mu UL},\ \tilde{u} = \frac{u}{U},\ \tilde{K}_p = \frac{K_p(h)}{K_p(H)}, \tag{3.2}$$

where $K_p(H)$ is the reference permeability at the reference height H, one can rewrite equation (3.1) as

$$\frac{d\tilde{P}}{d\tilde{x}} = -\frac{\tilde{u}}{\tilde{K}_p} - \frac{1}{\tilde{K}_p}. \tag{3.3}$$

In this steady frame the local volume flux $Q'$ (integral of $u$ across the layer) is a constant from continuity. The value of this constant can be found by integrating equation (3.3) from $\tilde{x} = 0$ to $\tilde{x} = 1$ and requiring that the pressure at the leading and trailing edges be equal to the atmospheric pressure $P_o$,

$$\frac{Q'}{Q_0'} = -\frac{\int_0^1 \frac{1}{\tilde{K}_p} d\tilde{x}}{\int_0^1 \frac{1}{\tilde{K}_p \tilde{h}} d\tilde{x}} = C_1, \tag{3.4}$$

where $Q_0' = UH$ is a reference flux.

The pressure distribution is given by

$$\tilde{P}(\tilde{x}) - \tilde{P}_0 = -\int_0^{\tilde{x}} \frac{C_1 + \tilde{h}}{\tilde{K}_p \tilde{h}} d\tilde{x}. \tag{3.5}$$

The dimensionless lift force $\mathbf{F}$= $FWK_p(H)/\mu L^2 U$, where F is the dimensional lift per unit width, is the integral of equation (3.5). The variation of $\tilde{K}_p$ with $h(\tilde{x})$ is determined from a Carman-Kozeny equation that takes account of the change in solid fraction with the variation in h as described in the next section.

For a planar planform, one can describe the variation of $\tilde{h}$ with $\tilde{x}$ as

$$\tilde{h}(\tilde{x}) = \tilde{h}_2 + (\tilde{h}_1 - \tilde{h}_2)\tilde{x}, \qquad 0 \le \tilde{x} \le 1 \tag{3.6}$$

and

$$d\tilde{h} = (\tilde{h}_1 - \tilde{h}_2) d\tilde{x}. \tag{3.7}$$

Thus, the variable $\tilde{x}$ in equations (3.4) and (3.5) can be replaced by $\tilde{h}$. For variable $\tilde{K}_p$, the integral in equation (3.5) needs to be evaluated numerically, however for $\tilde{K}_p$ constant, equation (3.5) can be integrated analytically

$$\tilde{P}(\tilde{x}) - \tilde{P}_0 = -\frac{1}{(\tilde{h}_1 - \tilde{h}_2)} \int_{\tilde{h}_2}^{\tilde{h}} \frac{C_1 + \tilde{h}}{\tilde{K}_p \tilde{h}} d\tilde{h} = \frac{-C_1}{\tilde{K}_p (\tilde{h}_1 - \tilde{h}_2)} \ln(\frac{\tilde{h}}{\tilde{h}_2}) - \frac{\tilde{h} - \tilde{h}_2}{\tilde{K}_p (\tilde{h}_1 - \tilde{h}_2)}, \tag{3.8}$$

Where

$$C_1 = -\frac{\int_{\tilde{h}_2}^{\tilde{h}_1} d\tilde{h}}{\int_{\tilde{h}_2}^{\tilde{h}_1} \frac{1}{\tilde{h}} d\tilde{h}} = -\frac{(\tilde{h}_1 - \tilde{h}_2)}{\ln(\frac{\tilde{h}_1}{\tilde{h}_2})}. \tag{3.9}$$

Figure 3.3 plots the dimensionless pressure distribution as a function of $\tilde{h}$ for k=1.25, the take-off position, and $\tilde{K}_p = 1$. This pressure profile has nearly the same shape as the dimensional pressure profiles in Fig. 3.12 of the chapter when the variation of $\tilde{K}_p$ with $\tilde{h}$ is considered since the maximum compression of the fiber layer is only 20 percent.

### 3.3.2 Porous media and theory for Darcy permeability

The properties of the porous material, its permeability $K_p$, the flexural rigidity *EI* of its fibers, and the maximum compression of the fiber layer, $k = h_1/h_2$, are all determined so as to satisfy the constraints outlined in the section Basic Design Criteria. The basic design of the AJT is illustrated in Figure 3.4 where the important dimensions are shown in longitudinal and transverse-section. Figure 3.4a, is a side view prior to lift-off when the AJT is fully (stationary) or partially supported by its front and rear wheels and Fig. 3.4b is cross-section A-A shown at mid-train. The

AJT has a fully loaded lift-off weight of 70 metric tons fully supported when airborne by a planform that is 30 m long and 3 m wide symmetrically positioned beneath the AJT, see Figure 3.4. Lift-off occurs in reverse order to conventional commercial aircraft where the front wheels lift-off first and then the rear wheels at higher speeds when the lift on the tail is sufficient. In marked contrast the center of pressure of the lifting planform on the AJT lies just aft of its center of gravity (c.g.) at midplane, and thus primary lift-off first occurs at low speed when the force on the rear wheels vanishes and the total weight is supported nearly entirely by the air pressure on the planform with very small contributions from the front wheels and the elastic restoring force of the fiber layer. Full lift-off occurs at higher speeds when the very small airfoils near the front are rotated to an angle of attack just sufficient to support the small remaining weight carried by the front wheels.

There are three principal constraints on the selection of the porous material. First, for safety reasons we would like primary lift-off for the rear wheels to occur at very low speeds, preferably < 5m/s (18 km/hr) so that initial take-off can be easily aborted if necessary. Second, we require that more than 99.8 percent of the lift force be generated by the air pressure, or < 0.2 percent from the solid fiber phase. As noted earlier we would like the fibers to produce a friction drag which is insignificant compared to the aerodynamic drag. Third, one would like the maximum compression of the porous medium to be a relatively small fraction of the porous layer thickness, no more than 20 percent of the layer thickness at the trailing edge. This will allow us to both satisfy the second constraint and preserve the resiliency of the porous bed. For H = 20 cm this corresponds to a 4 cm maximum compression at the trailing edge. We shall show that at high speeds this

compression will be reduced to < 1 cm and the planform will rise a little over 3 cm from its initial take-off position at its trailing edge. This is comparable to a maglev track where the suspended height of the train is typically 1.5 cm.

The first parameter that needs to be determined is the permeability of the porous layer $K_p$. Initial studies in Wu, Andreopoulos and Weinbaum (2004) suggest that $K_p$ lies somewhere between $10^{-9}$ m$^2$ for fine grain snow powder and $10^{-8}$m$^2$ for goose down. In essence one would like to perform a parametric study where one could estimate the primary lift-off velocity U as a function of $k = h_1/h_2$ for several values of $K_p$ that lie within this range of $K_p$. For this purpose we consider the simpler case where both the variation of $K_p$ with compression and the small lift force due to the fiber phase are neglected in solving equation (3.4) and (3.5) for the pressure distribution on the planform. One then integrates this pressure distribution over the surface of the planform and sets F.W in the expression for the dimensionless force $\mathbf{F} = FWK_p(H)/\mu L^2U$ equal to the weight of the AJT. Since the required compressions are relatively small this calculation provides a reasonable first order approximation to the lift forces that can be generated for a given $K_p$ in the asymptotic limit where $\alpha >> 1$. This solution, which provides an expression for U as a function of k with $K_p(H)$ as a parameter, is shown in Figure 3.5.

We are primarily interested in the portion of the curves in Figure 3.5 where k < 1.25. This corresponds to a 4 cm compression at the trailing edge if H =20 cm and a tilt of 1/750 or < 0.1 degrees. $\mu$ is the viscosity of the air at 20º C. The values of $K_p$ of interest fall in the range $10^{-8}$ to $10^{-9}$ m$^2$. There are three key observations. First, one notes that for k to be < 1.25, $K_p(H)$ has to be < $5 \times 10^{-9}$ m$^2$ if U is < 5 m/s. This sets the bar for our first constraint on primary lift-off velocity. Second, when

$K_p(H)$ is 1.0 x $10^{-9}$ $m^2$ the compressions of the matrix will be too small at low velocities to finely control the elevation of the planform. Third, at speeds > 50 m/s k will < 1.05, or trailing edge compressions < 1 cm for all values of $K_p(H)$ shown. Thus, very small angles of attack are required for velocities > 50 m/s. This highly non-intuitive result indicates that remarkably small compressions of the porous layer are required to support a 70 metric ton AJT when lateral leakage of the porous bed is prevented.

We would next like to characterize the solid fraction and the fiber radius of the porous matrix layer knowing that the desired $K_p(H)$ is approximately 5 x $10^{-9}$ $m^2$. The fiber radius plays a critical role since the flexural rigidity *EI* of the fibers is the key parameter in determining their elastic restoring force or the solid component of the lift. The moment of inertia, I, for a circular cylindrical fiber of radius $r_f$ is $\pi r_f^4/4$ from which it clear that a mere doubling of the radius $r_f=D/2$ will lead to a 16 fold increase in bending rigidity. Soft, random, fibrous materials are well described by the empirical Carman-Kozeny formula described in detail in Happel and Brenner (1983). As shown in Mirbod, Andreopoulos and Weinbaum (2009a), $K_p$ can be written in the compact form,

$$K_p = \frac{{r_f}^2 \varepsilon^3}{4G(1-\varepsilon)^2}, \tag{3.10}$$

Here $\varepsilon$ is the void fraction, $(1-\varepsilon)$ is the solid fraction, $r_f$ is the fiber radius, and G is an empirically measured Carman-Kozeny constant. In the limit when the solid fraction $1-\varepsilon << 1$, G can be approximated by $\frac{-5}{3(1-\varepsilon)\ln(1-\varepsilon)}$.

Equation (3.10) is plotted for several representative values of $r_f$ between 3 and 10 μm in Fig. 3.6 for values of $K_p$ in the vicinity of 5 x $10^{-9}$ $m^2$. It is clear from Figure 3.6 that polyester fibers with radii between 3 and 10 μm radius can all satisfy our requirements for $K_p$ ~ 5.0x$10^{-9}$ $m^2$, and that the deciding criterion will be their flexural rigidity *EI*.

Equation (3.10) also provides a convenient expression for determining an intuitively reasonable approximation for the variation of $K_p$ with position $x$ that is needed to more accurately describe the change in permeability of the fiber layer with compression. This is particularly useful at low velocities prior to primary lift-off where there is a 20 percent variation in layer thickness and significant variation in permeability. A relatively simple and reasonable assumption is that when the fiber layer is compressed the increase in fiber density is locally proportional to the local decrease in height of the fiber layer. Thus, the solid fraction, $1-\varepsilon$, decreases as $(1-\varepsilon_2)(h_2/h)$ where $h_2$ is the height of the layer at the trailing edge. Using Eq. 3.10 and the foregoing assumptions for the variation of $\tilde{K}_p$ with $\tilde{h}$, one can define a dimensionless local Darcy permeability $\tilde{K}_p$ by

$$\tilde{K}_p = \frac{K_p(h)}{K_{p2}} = \tilde{h} - \frac{\tilde{h}\ln\tilde{h}}{\ln(1-\varepsilon_2)}, \tag{3.11}$$

where $\tilde{h} = h/h_2$ and $K_{p2}$ is the minimum value at $h=h_2$. The solid fraction $(1-\varepsilon_2)$ can be easily determined if the length of fibers per unit volume can be estimated, the fibers are of uniform radius and their density is known.

The results presented in Figs. 3.5 and 3.6 guided our search for an inexpensive, inert soft porous material with a $K_p$ of approximately 5.0x$10^{-9}$$m^2$ and $r_f$

of approximately 5μm. One class of materials with these properties is the soft polyester fiber-fill that is commonly used in inexpensive body pillows. A sample of this fill is shown in Fig. 3.7a, b where we observe in Fig. 3.7a the random arrangement of these fibers and in Fig. 3.7b a single fiber of $r_f$ =5 μm radius, a dimension which is representative of nearly all the fibers observed in Fig. 3.7a. In general, it is a difficult matter to determine, $1-\varepsilon$, unless the fibers are of nearly uniform cross-section as shown in Fig. 3.7a. If this is the case, one can readily measure the weight of a large known volume of fibers and then from the specific gravity of the polyester material and the individual fiber geometry shown in Fig. 3.7b determine the length of fiber per unit volume $L_f$. The polyester fibers shown in Fig. 3.7 have a density of 1.39gr/cm$^3$. Thus, for $r_f$= 5 μm, $L_f$ was found to be 5950 cm/cm$^3$. This corresponds to a solid fraction of 4.7 x $10^{-3}$ or a void fraction ε of 0.995 for our deformed matrix layer. From equation (3.10), $K_p$ is 3.4 x $10^{-9}$m$^2$. The fiber-fill shown in Fig. 3.7 is manufactured by Mountain Mist. It is 95% polyester and 5% silk.

The undeformed thickness H of the fiber layer plays a minor role in the design of the track only if lateral leakage at the sidewalls is negligible and $H/W \ll 1$. However, as $H/W$ increases confined compression tests in our piston loaded porous walled cylinder apparatus show that a sizeable friction force can develop along the sidewalls due to the restrained radial expansion of the fiber layer. The value of H and the initial value of $k=h_1/h_2$ were, therefore, chosen to keep this restraining force small, but large enough so that if there was a small leakage of air at the sidewalls this small leakage would not seriously affect performance. A more detailed model to examine the lateral leakage of air at the sidewalls will need to be developed in the

future to study this important practical limitation. In essence lateral leakage of air must be small compared to the air that is shoved forward by the inclined boundary.

## 3.4 Restorative properties of porous material

As already noted in Fig. 3.6 fibers of different radii can satisfy approximately the same $K_p$ if they have an appropriate solid fraction. The deciding factor is their flexural rigidity. Laboratory tests were performed to measure the local restoring force of the fiber layer as a function of $\Delta h/H$, which is the fractional decrease in height h of the fiber layer.

The non-linear fiber force, $F_s$, is determined by an independent quasi-static experiment, in which one considers a piston-cylinder of 40 cm diameter in which we compress a porous layer whose undeformed height is H = 20 cm. Incremental weights are added, and after each addition, the compression $\Delta h$ of the fiber layer is measured till one achieves a maximum compression, $\Delta h/H$ of approximately 0.6, see Figure 3.8.

The average pressure due to the fibers, $P_s$, is given by $F_s/A$ where $F_s$ is the weight of the piston plus its incremental weights and A is its area. The pressure-displacement curve becomes increasingly non-linear for larger values of $\Delta h/H$ but for small compressions, where $\Delta h/H < 0.3$, the curve is nearly linear, with a slope, $\beta$, of 142.5 N/m$^2$.

$$P_s = \beta \frac{\Delta h}{H}. \tag{3.12}$$

Thus, for $h_1$=20 cm and $h_2$=16 cm or an average compression of 2 cm ($\Delta h/H$=0.1), $P_s$= 14.2 N/m$^2$ and $F_s$=0.13 metric tons. This is the maximum force prior to primary lift-off (U = 4.43 cm/s) when $k=h_1/h_2$ has its maximum value of 1.25. At higher speeds k and $F_s$ both decrease.

The force required to compress a 20 cm thick fiber layer 1.0 cm in a confined compression was 7.1 N/m$^2$. The compression of the fibers varies linearly with distance from the trailing edge of the planform. For a 4 cm compression at the trailing edge, the total force from the fibers prior to lift-off is 0.13 metric tons or about 0.19 percent of the total lift. This lift decreases nearly linearly as the compression at the trailing edge decreases. The maximum friction force on the planform in the ensuing calculations assumes a coefficient of sliding friction of 0.2 or a total friction force of 0.026 metric tons. Fibers of 10 μm radius would clearly have produced lift and sliding friction forces that would have been significantly greater, and the polyester fibers in Fig. 3.7 were the smallest diameter that we could find.

The restorative properties of the fibrous material are shown in Figures 3.9 and 3.10. The tests were performed in the confined cylinder apparatus and various compression ratios were used to characterize the material behavior. Figure 3.9 shows the results immediately after short time compressions at various levels. It appears that for all compression ratios with $\Delta h/H<0.31$ the short time permanent deformation after the load relaxation was < 0.018 and for the average compression anticipated in the present application the remaining deformation is < 0.01.

The long term restorative behavior of the material is depicted in figure 3.10. Compressions from 1 minute to 30 minute durations were applied to the material for

the case of $\Delta h/H=0.22$ and the recovery of the material thickness, defined as the ratio $h_r/H$ is plotted for two different relaxation times. The two minute relaxation data indicate that the recovery of the material depends on the duration of compression. For compression durations of less than 2 minutes the recovery is close to 94 % while for compressions of more than 5 minutes the recovery is only 80 % after 2 minutes relaxation but after a 15 minutes relaxation, is close to 95 %.

The immediate recovery of the material can be attributed to the spatial rearrangement of its fibers while the remaining small permanent deformation is most probably due to the slow and rather incomplete stress relaxation process of the individual fibers.

In order to determine the durability of the material cyclic load/unload was applied with a duty cycle consisting of 1 minute compression duration and 2 minute relaxation. The results are shown in Figure 3.11 where the recovery is plotted against the number of cycles applied. The data show a minor reduction in recovery within the first 10 cycles which levels off to a constant value of 93% in the range up to 50 cycles investigated here.

These experimental data demonstrated some of the non-linear characteristics and memory effects the material exhibits. It appears that for the present design compression parameters and operation envelops the material restores itself to its original characteristics almost immediately after the removal of the load.

Confined compression tests in our piston loaded porous walled cylinder apparatus in Al-chidiac, Mirbod, Andreopoulos and Weinbaum (2009) show that a sizeable friction force can develop along the sidewalls due to the restrained radial

expansion of the fiber layer. The value of H and the maximum value of $k=h_1/h_2$ were, thus, chosen to keep this restraining force small.

## 3.5 Results

### 3.5.1 Pressure profiles and force distribution

The solutions of equations (3.4) for $C_1$ and (3.5) for the quasi-steady pressure profiles beneath the planform are shown in Figure 3.12. At start-up $h_1$ at the leading edge is 20 cm and $h_2$ at the trailing edge is 16 cm. The pressure builds up as the velocity of the AJT increases and at a velocity of 4.43 m/s this pressure is nearly sufficient to support the entire weight of the plane except for the force of the fibers, whose integrated force is 0.13 metric tons, and the small force $F_{WF}$ on the front wheels. As shown in Fig. 3.13, the force on the rear wheels $F_{WR}$ vanishes at this velocity. With further increase in velocity the tilt angle of the planform decreases as the trailing edge rises slowly in the fiber layer, whereas the front wheels remain on the ground but the force on them also slowly decreases as the center of pressure shifts slightly towards the center of gravity. There is little change in the pressure profile under the planform once the rear wheels lift off since the changes in tilt angle are small and the weight that is supported by the air pressure does not change significantly. This analysis does not take account of the end corrections at the leading and trailing edges of the planform where the pressure is nonuniform in the y direction and there is an adjustment to atmospheric conditions. These changes occur on a length scale of $O(H)$ where $H \ll L$.

The force distribution and the stability of the AJT are readily deduced from Fig. 3.13 and its moment diagram, inset of Fig. 3.13, showing the lever arms for the application of the key forces about the c.g. At time t = 0 the forces on the front and

rear wheels are nearly the same except that the small fiber force $F_s$ is asymmetrically distributed due to the planform tilt. The center of pressure for the fibers is 1/3 the distance or 10 meters from the trailing edge. Since this force is only 0.19 percent of the total weight these small differences in $F_{WR}$ and $F_{WF}$ at rest are difficult to observe in Fig. 3.13. However, one does notice that as the velocity increases toward 4.43 m/s a larger difference in force develops between the front and rear wheels. At 4.43 m/s, when $F_{WR}$ vanishes, $F_{WF}$ is 1.4 metric tons. The origin of this asymmetry is due to the fact that the pressure profiles in Fig. 3.13 are not quite symmetric about the center of the planform. This asymmetry arises primarily from the variation of $K_p$ which increases as one proceeds from the trailing to leading edges as a result of the decreasing compression. All of the foregoing results are based on the simplifying assumptions that the aerodynamic drag force and the thrust from the jet act through its center of gravity.

### 3.5.2 Stability

The small force due to the fibers, further decreases as the speed of the AJT increases, since as observed in Figure 3.5, the value of k approaches 1.0 as U increases. At high velocities $F_s$ and the friction force from the fibers are truly negligible. The center of pressure for the pressure (air) force $F_A$ always lies to the left of the c.g. and it is this displacement that creates the small force on the front wheels. The pitching stability is created by the fact that the c.g. always lies between the center of pressure and the front wheels. At speeds in excess of 50 m/s, or 180 km/hr, one would like to become completely airborne to avoid front wheel vibration. This is readily achieved by the small airfoils at the front of the AJT. At

this speed the center of pressure has shifted to within 0.16 m from the c.g. and the force on the front wheels has been reduced to 0.96 metric tons. The area of these small airfoils can be readily estimated. At a 10 degree angle of attack a typical lift coefficient, $C_L = \text{Lift}/0.5\rho U^2 A$, for a wing of area A is 1.0. If we want to reduce the lift force on the front wheels, $F_{WF}$, to zero at this velocity, one finds by applying moments about c.g. that the required area of the two front airfoils is only 4.3 $m^2$. Once this lift is achieved the front wheels can be retracted.

The AJT has built in pitching stability. If too much lift is supplied by the front airfoils the front of the planform will rise slightly above the SPT and the tilt of the planform will increase slightly. This will cause the center of pressure to shift slightly rearward and the planform will dip downward causing the front of the planform to again make contact with the SPT.

Another consideration is the shift in the c.g. due to movement of the passengers and service carts. The main criterion is that the center of pressure must lie sufficiently aft of the c.g. so that small changes in the position of the c.g. do not change the sign of the pitching moment.

Small undulations in the surface of the SPT are smoothed out by its contoured leading edge much like soft snow in front of a toboggan. However, long gradual inclines will cause a vertical bounce (heave) at their crest due to the inertia of the AJT unless properly accounted for. To avoid bounce the centrifugal force $mU^2/R$, where R is the radius of curvature, cannot exceed the gravitational force, mg, or the AJT will overshoot the track. For this not to occur R has to be $> U^2/g$. Other instabilities such as sideslip (jiggle) and rocking or roll are briefly discussed in the Appendix A.

### 3.5.3 Propulsion requirements and performance

Perhaps the simplest propulsion system for our train is a pair of small jet engines. Since one does not have to climb to altitude and the lift induced drag is negligible, these engines can be much smaller than their traditional jet aircraft counterparts. The major considerations are the acceleration of the train and its aerodynamic drag. As already seen, the friction force on the planform and the work done to compress the SPT, which is proportional to its small tilt angle, are negligible. A typical drag coefficient, $C_D = D/0.5\rho U^2 A$ for a streamlined high speed train (maglev or French TGV) is typically 0.2. A, the cross-sectional area is 10.8 $m^2$, and the aerodynamic drag D can be roughly approximated by $D = 0.1\rho U^2 A$. Newton's law for the required thrust (T) to accelerate the train is given by

$$m\frac{dU}{dt} = T - 0.5C_D\rho U^2 A, \tag{3.13}$$

where *m* is the mass of the AJT and ρ is the density of air.

The solution which satisfies initial condition *U=0* at *t=0* is given by

$$U = \sqrt{\frac{T}{0.5C_D\rho A}}\tanh\left(\sqrt{0.5C_D\rho AT}.\frac{t}{m}\right). \tag{3.14}$$

The results for the performance are plotted in Fig. 3.14 for three different thrust jets, 5000, 10,000 and 15,000 lbf. One notes that one can accelerate to nearly maximum velocity in about 100s with 10,000 lbf engines. The maximum velocity is estimated to be 820 km/hr, 670 km/hr and 470 km/hr for the three different thrusts shown. The present record for a maglev is 581 km/hr and for the French TGV 575 km/hr.

The results in Fig. 3.14 can also be used to describe how the terminal velocity would change if the AJT has to ascend a long gradual incline. For example, from

Fig. 3.14 if 5000 lbf (2273 kgf) of a total thrust of 10,000 lbf is used to overcome gravity and 5000 lbf is used to overcome aerodynamic drag, the terminal speed will be reduced from 670 to 470 km/hr for an incline whose angle is 2273/70,000 or 0.0325 radians (roughly 2 degrees).

The energy expenditure or work done is the thrust times the distance. Conventional jet aircraft carrying 200 passengers typically have engines with 50,000 lbf thrust. This is largely required for take off and climbing to altitude. The fuel consumption is proportional to the work done and there could be nearly 80 percent savings in fuel consumption for the AJT on short flights using engines with 10,000 lbf thrust. In addition, the AJT has a major advantage over commercial jets in that its greenhouse emissions are released at ground level rather than at high altitude where the effects on global warming are far more severe.

## 3.6 Discussion

The SPT described in this chapter provides a new concept for generating lift forces of the magnitude that would be comparable to the weight of large capacity commercial jet planes. The unique features of the track are that the fiber phase contributes insignificantly to the lift, in contrast to skiing or snowboarding where this is typically 50 percent, and its main function is to produce a large aerodynamic resistance for the passage of air out of the confined space containing the porous medium due to the presence of impermeable lateral boundaries. Our theoretical model predicts that one should be able to attain speeds higher than existing maglev and TGV train systems with a fuel expenditure that could be as little as 1/5 that of comparable capacity commercial jets, at least for short distance flights over land.

The AJT has the additional advantages over traditional aircraft in that it is land based and not as sensitive to weather and air turbulence and over maglev in that potentially it could be connected to existing track infrastructure with modest changes in design.

Perhaps one of the most revealing insights into the role of the porous layer is that the air beneath the ski in the porous layer is barely moving although the AJT is moving at 180 m/s. This velocity, which is easily calculated from the pressure gradient in Fig. 3.12, never exceeds 0.3 m/s, and this only at the trailing edge of the ski. At first glance this may seem unbelievable since the void fraction is > 0.995. The secret is that the fibers are very slender, 10 μm diameter, and there is nearly 6000 cm length of fiber per $cm^3$. This corresponds to an average fiber spacing of only 120 μm. The Darcy permability, $K_p$ is 3.4 x $10^{-9}$ $m^2$ and thus the fiber interaction layer thickness, $\sqrt{K_p}$, or effective pore size is only 60 μm. The maximum pressure gradient occurs at the trailing edge of the ski and changes little once the velocity of the train car exceeds 4.4 m/s (primary lift-off of the rear wheels), see Fig. 3.12. Thus u is < 0.3 m/s at the trailing edge of the ski no matter how fast the AJT is moving once rear wheel lift-off is achieved. One can readily show that for this velocity the fiber Re is ~ 0.2 and the Re based on $\sqrt{K_p}$ is ~ 1.2. This justifies the neglect of inertia and the inclusion of a non-linear Forchheimer term in the governing equation for the porous layer.

The AJT is similar to a maglev operating in the electrodynamic mode in that at low speeds it must be supported by wheels during initial lift-off. Using the soft fiber-fill described in this chapter, the primary lift-off occurs at the surprisingly low velocity of only 4.43 m/s. This low speed is an added safety feature not available to

subsonic jet aircraft during take-off. A major advantage over maglev is the cost of materials used to construct the track. The polyester fiber-fill is extremely inexpensive, can be produced in large volume and has robust restorative properties.

The proposed AJT still has some of the same disadvantages as high speed trains, difficulty in turning maneuvers, noise control at high speeds and the development of a new track system. As noted earlier, the track requires a highly porous, light weight protective screen that rests on the top of the porous layer to protect it from wear and tear and debris. In a small scale prototype in our laboratory we are exploring the use of a plastic gutter guard commonly used in rain gutters for the protective screen. For both noise control and protection from weather one would probably want to have the train and track covered in an open air tunnel with a transparent or translucent roof which allows in light but protects the track from the elements. The cost of the maintenance of the track and the replacement of the fiber-fill material would depend on its durability. The two most important practical limitations would appear to be keeping the track clean and free of debris and the elimination of pressure leakage at the edges of the planform along the sidewalls as discussed earlier. A larger value of H would compensate for leakage but introduce significant friction forces at the sidewalls. We are currently exploring designs which have the potential to greatly reduced leakage.

Turning maneuvers are difficult at high speed on land. For example, the turning radius of the track on the newest TGV trains using LGV track is four miles. For the proposed AJT there are two alternate designs that would permit turning. The planform itself would either have to allow for a system of overlapping sliding panels so that the planform could adjust to a slowly curving track or the planform

could be raised and lowered so that turns would be done on wheels at lower speeds like traditional trains. The sketch in Fig. 3.4a,b is for a prototype that would involve only a single track. In this sketch the AJT is symmetric and the jets are simply rotated 180 degrees to reverse direction. Deceleration would be achieved by reversing the jets in a similar manner to jet planes.

## 3.7 Appendices

### 3.7.1 Appendix A. Other mechanisms for instability

In addition to pitching instability, short wave length non-uniformities in the surface of the track and vertical bounce (heave), which are discussed in the main text, other modes of instability include sideslip and rocking or roll.

One does not anticipate much in the way of sideslip or jiggle since the 30 m long ski will have only a few mm clearance on each side before it grazes the sidewalls. Practically, one may want to add a hard felt glider material on the sidewalls of the track to prevent abrasion by the edges of the ski. In our 1/30 scale laboratory model there is about one mm total clearance (both sides combined) and there is no evidence of jiggle because the length of the ski, 1 m, is 1000 times larger than the sidewall clearance. The speeds are obviously much slower than the full scale AJT, where the length of the ski is $10^4$ larger than the sidewall clearance.

Rocking or roll is an interesting and difficult question that is hard to answer. There are two obvious means of controlling rolling about the central axis of the train. The situation is clearly very different than a toboggan. When a toboggan tilts laterally there is very little restoring force since the resistance to roll is largely coming from the compressed snow which has no recoil and the air pressure

contributes little since it is lost along the lateral edge of the toboggan. In the train most of the resistance to rolling arises from the air pressure. In fact, as one edge goes down the opposite edge may actually rise slightly above the track and create a cross flow in the porous material with pressure leakage on the high side. This would be a very interesting problem to examine using the 2-D planform theory developed in Feng and Weinbaum (2000). In our contemplated renewal application to NSF we do intend to look at leakage and rolling and to instrument our laboratory model to measure pressure leakage. The other means of controlling roll is by use of the front and rear airfoils which can act as stabilizers if their angle of attack on each side of the AJT is controlled separately. In general, centrifugal forces in turning will create significantly greater lateral moments than rocking or rolling on a straight track where the required restoring forces will be much smaller.

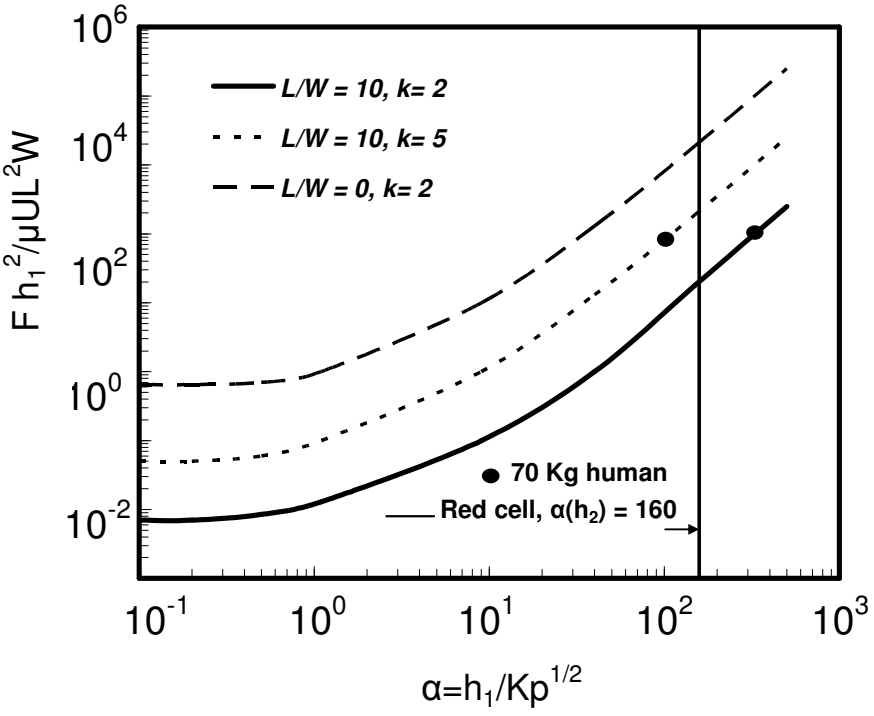


Figure 3.1 Dimensionless lift force as a function of α, L/W and compression ratio k. Also shown are the results for a red cell and ski-snowboard. (Adapted from Fig.15 in Feng and Weinbaum (2000))

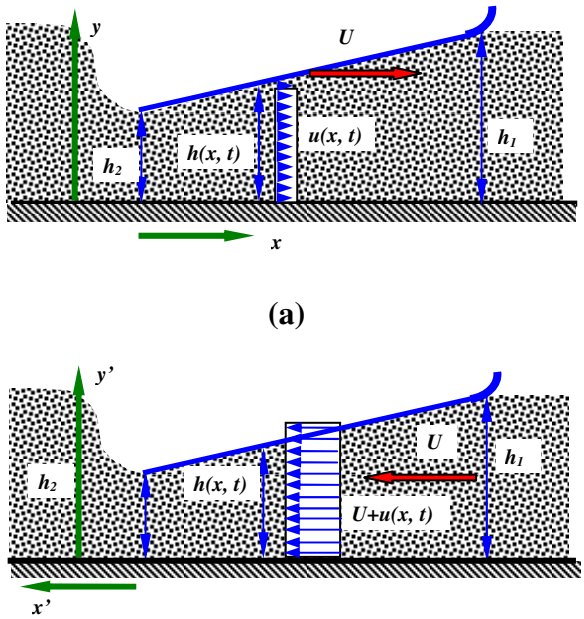


Figure 3.2 The basic flow geometry for the planar lifting surface. (a) Original (x, y) coordinate system. (b) Transformed (x′, y′) coordinate system.

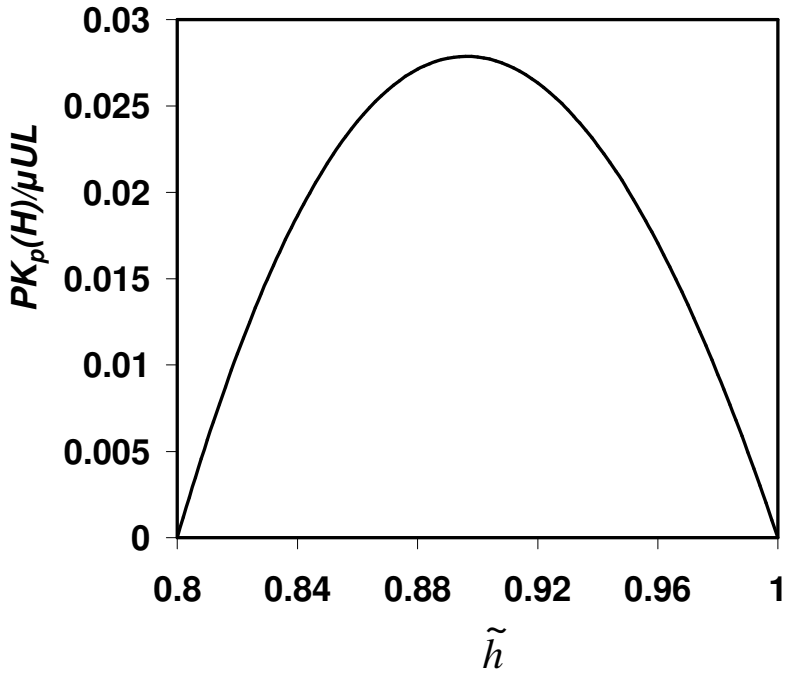


Figure 3.3 Pressure distribution as a function of $\tilde{h}$ for $\tilde{K}_p = 1$ and k=1.25.

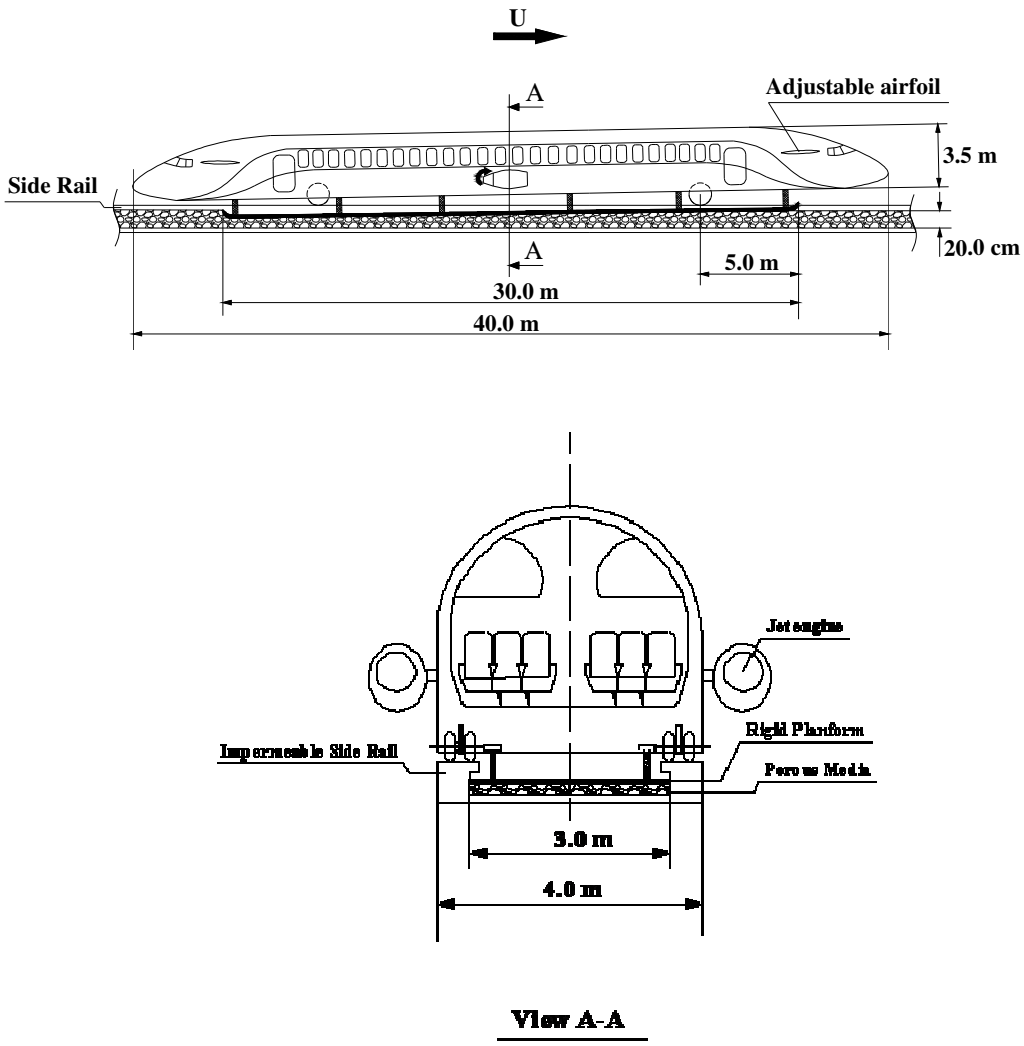


Figure 3.4 (a). Design of the AJT showing initial position at take-off, k = 1.25, and basic dimensions. (b) Cross- section A-A at mid-car.

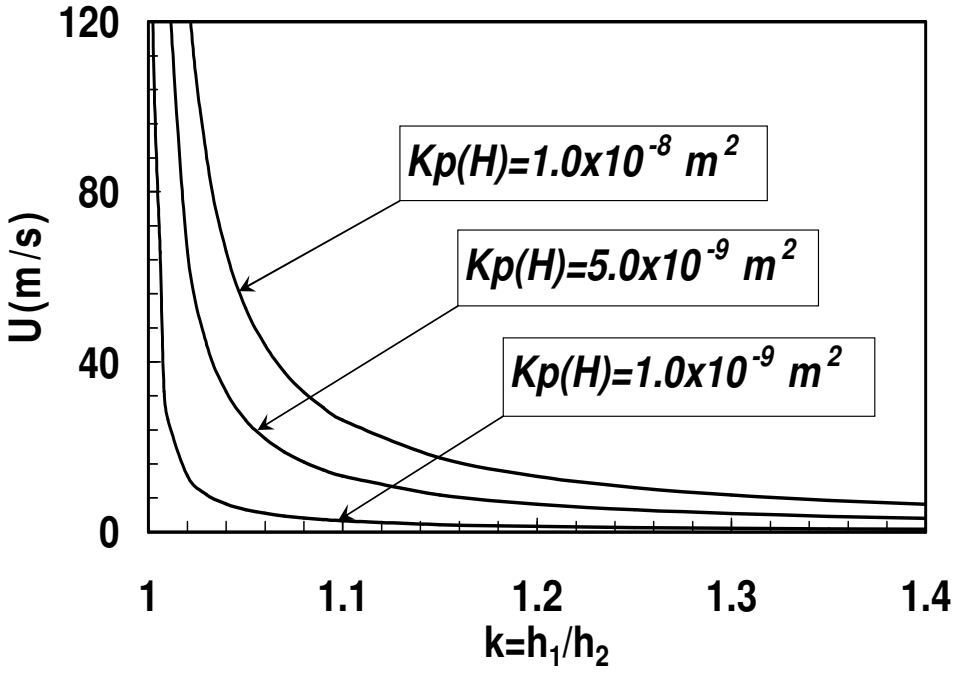


Figure 3.5 The velocity U required to support a 70 metric ton AJT as a function of its planform compression ratio, k, for three different *Kp;* $10^{-9}$, $5.0 \times 10^{-9}$ and $10^{-8}$ $m^2$.

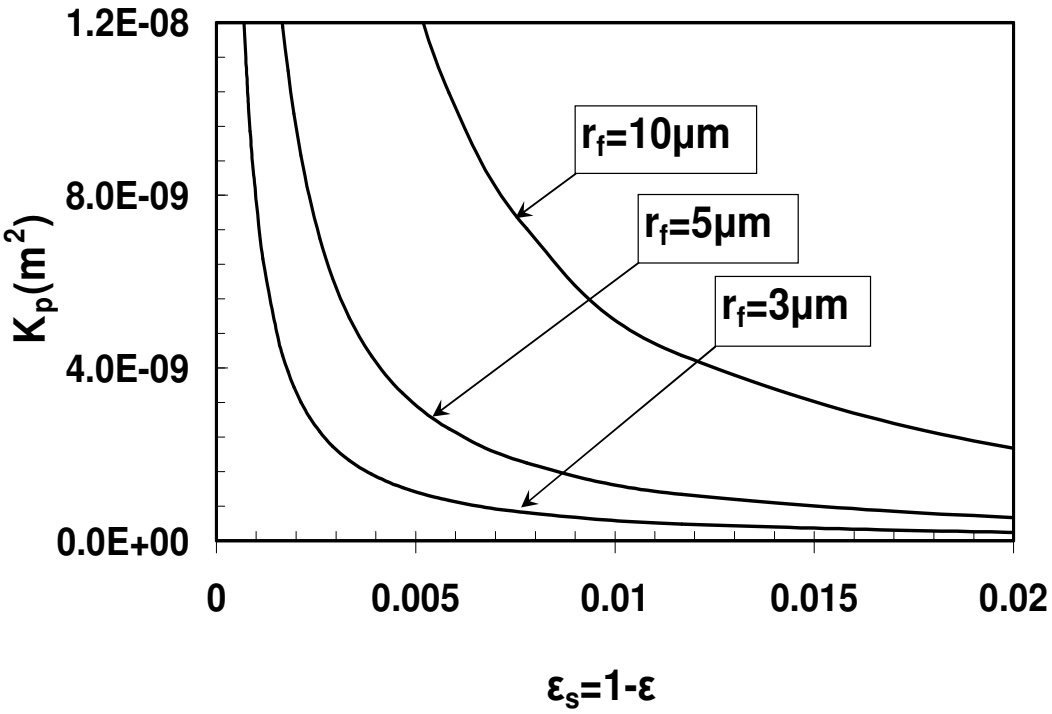


Figure 3.6 Darcy permeability of porous media versus solid fraction, 1-ε, for different fiber radii.

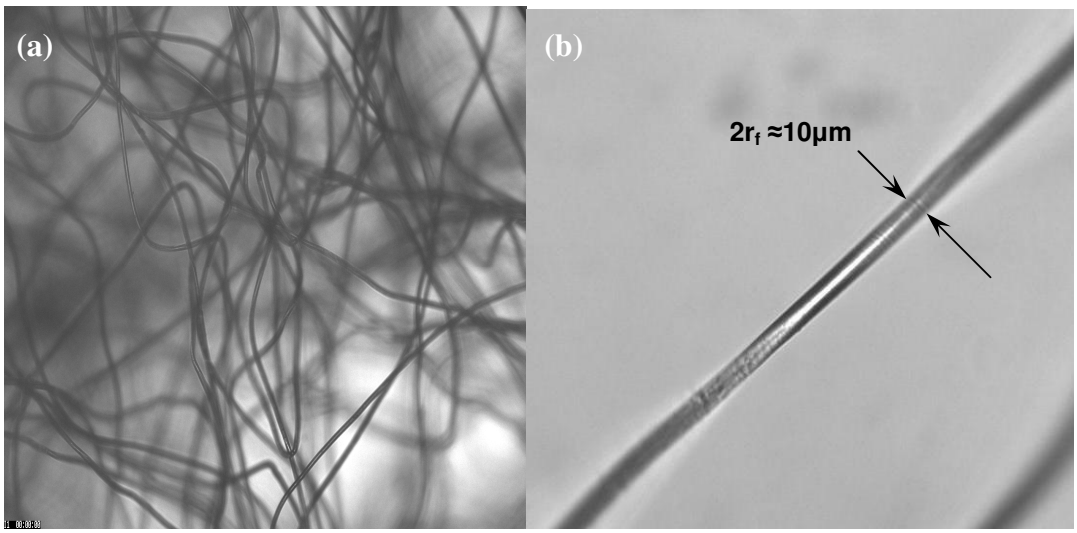


Figure 3.7 (a) Sample of the fiber-fill material. (b) A single filament of the fiber-fill to determine its radius.

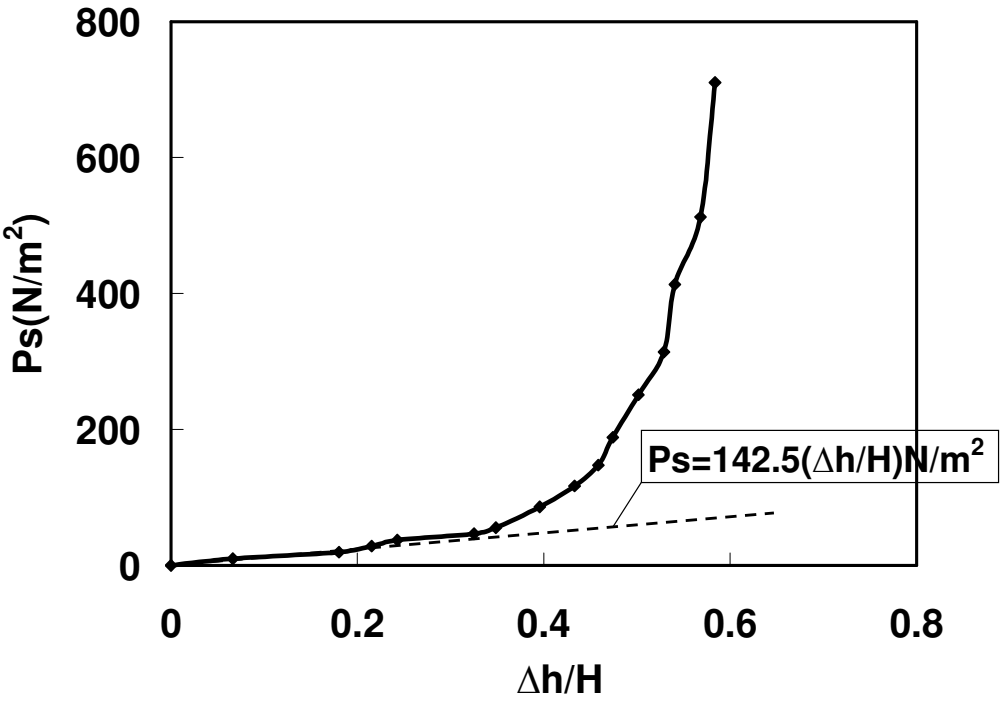


Figure 3.8 Fiber layer pressure $P_s$ as a function of $\Delta h/H$.

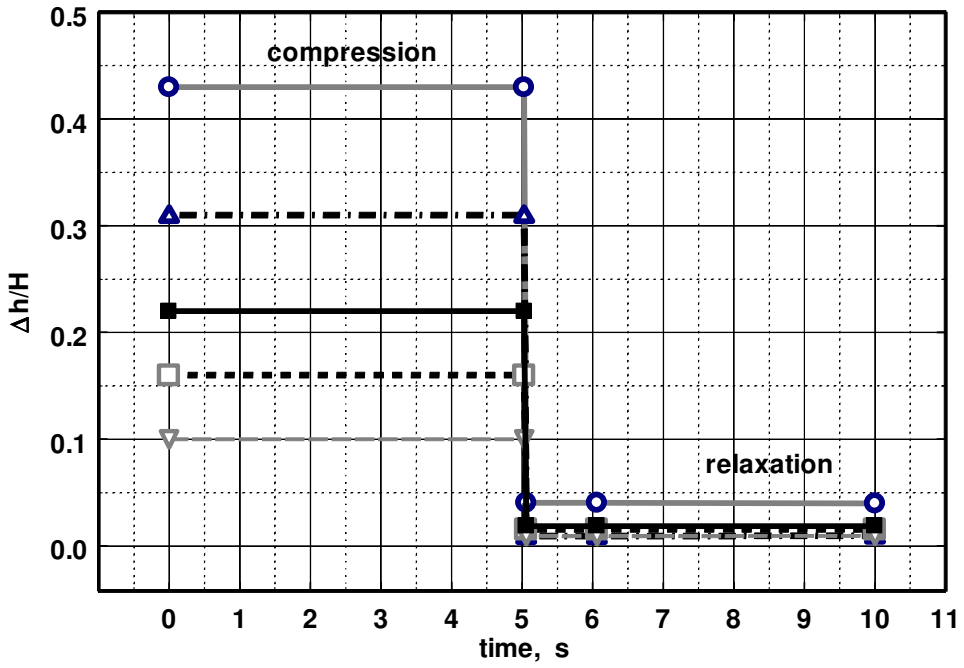


Figure 3.9 Short term restorative properties of material.

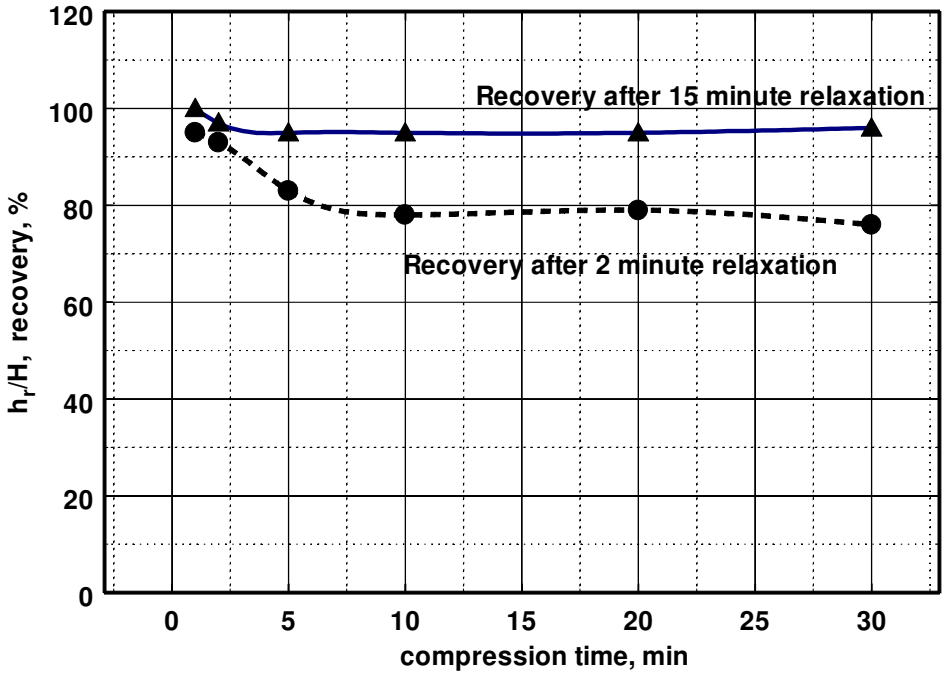


Figure 3.10 Long term restorative properties of material.

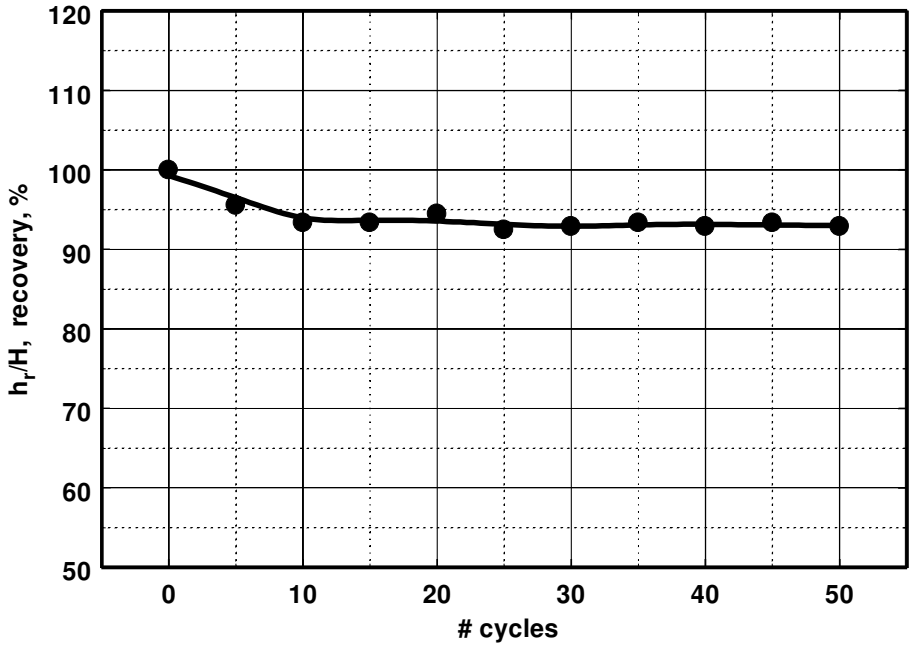


Figure 3.11 Restorative properties of material under cyclic load/unload with duty cycle of 1 minute compression and 2 minutes relaxation for $\Delta h/H=0.22$.

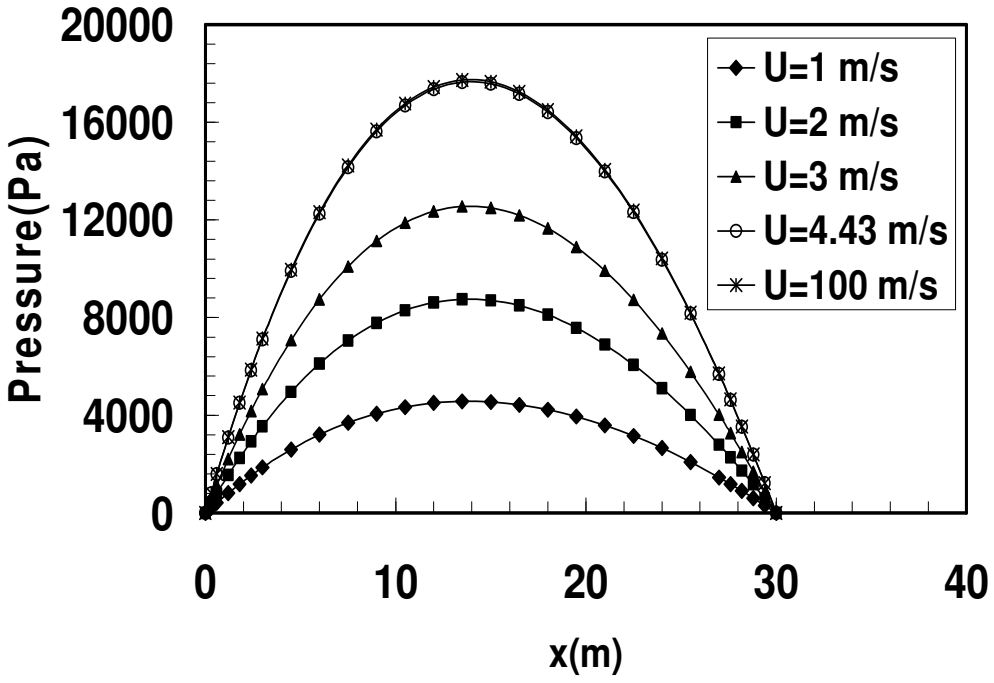


Figure 3.12 Change in pressure profiles as a function of the velocity U during take-off. Note little change in profiles for U > 4.43 m/s.

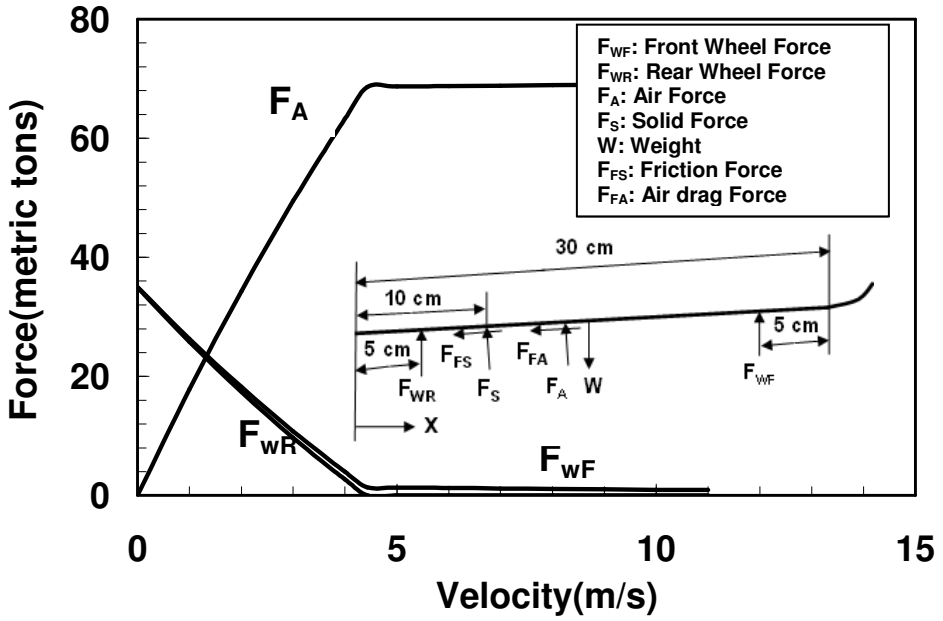


Figure 3.13 Change in the key forces on the AJT as it accelerates during primary lift-off. $F_{WF}$ is the force on the front wheels, $F_{WR}$ force on rear wheels, $F_A$ air pressure force and $F_s$ the force of the fibers. W, the weight acts at the c.g. and moment balance is taken about the c.g.

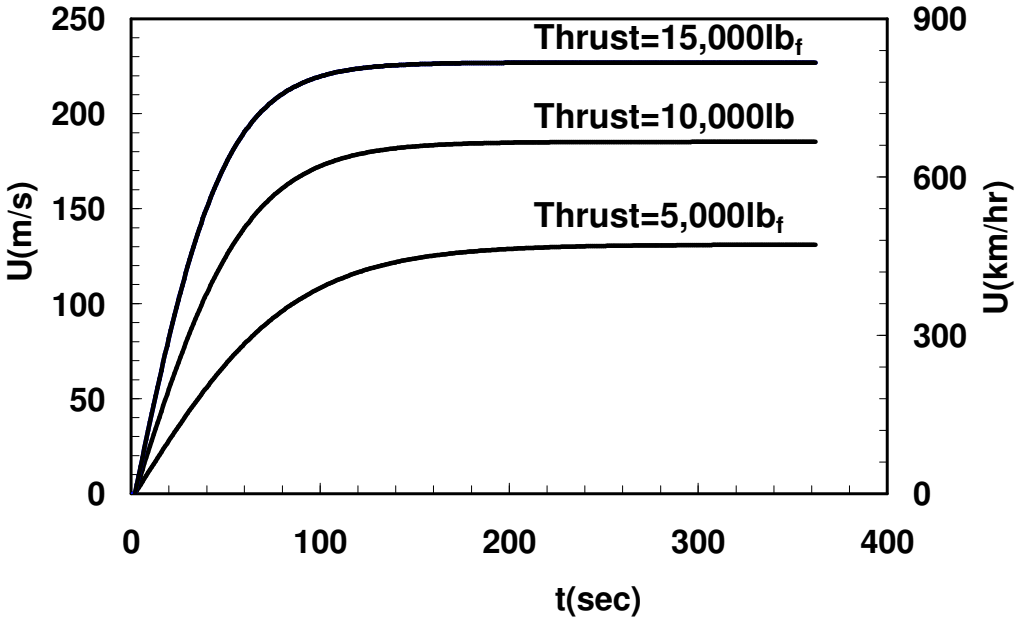


Figure 3.14 Acceleration of AJT to cruising velocity as a function of time for three different thrust jets, 5000, 10000, 15000 lbf.

# Chapter 4 Concluding Remarks

Whereas the mechanical behavior of the solid phase and the flow inside the porous media have been studied in the past, relatively little attention has been paid to highly compressible, soft porous materials since these materials are traditionally thought to be structurally fragile and support little weight unless highly compressed. This view was dramatically changed as a result of the series of studies on lift generation in porous media developed by Feng and Weinbaum (2000), Weinbaum *et al.* (2003), Wu *et al.* (2004, 2005, 2006), Mirbod *et al.* (2009a, 2009b) and Al-Chidiac *et al.* (2009) in which they have demonstrated theoretically and experimentally that these materials could transiently support very large loads beneath a planing surface for short duration if the trapped fluid within the fibrous medium could not escape on the time scale of the passage of the planing surface. These concepts, which were first conceptualized in trying to explain the "pop out" phenomena that was observed in the motion of red blood cells in capillaries by Vink and Duling (1996), are applied in this dissertation: 1) To extend the generalized Reynolds equation derived in Feng and Weinbaum (2000) to random porous media using the Carman-Kozeny equation for a random fiber array. The loss of pressure at the lateral edges is eliminated by using impermeable sidewalls. 2) To examine the generation of pressure and lift forces in a random soft fibrous media layer that is confined between two planar surfaces, an infinite horizontal lower boundary and a horizontal inclined upper boundary, in the lubrication limit where the characteristic thickness of the fiber layer $H \ll L$ the length of the inclined surface. 3) To explore the quantitative feasibility, performance and stability of a 70 metric ton airborne jet-ski train that flies on a soft porous track with extremely low sliding friction.

In the Appendices I and II of this dissertation, the dynamic lift forces generated during compaction of soft highly compressible fibrous materials in a piston/cylinder apparatus are examined and these experimental results are applied to a model for the AJT in Chapter 3.

A summary of the fundamental concepts in lift generation in porous media and key results are listed bellow:

**1.** F&W (2000) predicted that the excess pore pressure generated by a planing surface moving on any compressible porous media scales as the square of the dimensionless permeability parameter, $\alpha=h/\sqrt{Kp}^{1/2}$, where h is the layer thickness and Kp is the Darcy permeability, and that α is of order of 100 or larger for both red cells gliding on the endothelial glycocalyx and human skiing.

**2.** The new theory developed in F&W, also showed that there is an unexpected striking similarity between the gliding motion of a red cell moving over the endothelial glycocalyx that lines our microvessles and a human skier or snowboarder skiing on compressed powder although they differ in mass by $10^{15}$. In both cases one observed an order of magnitude compression of the matrix layer when the motion is arrested and predicted values of α that are of order 100. In this large α limit one finds that the pressure and lift forces generated within the compressed matrix are four orders of magnitude greater than classical lubrication theory.

**3.** F&W also proposed that the principle difference between the tightly fitting red cell and the snowboarder is the lateral leakage of the excess pressure at the edges of

the snowboard which greatly diminishes the maximum enhancement in the lift force by a factor $(W/L)^2$, where W/L is the ratio of the width to the length of the planing surface. That is why we use a highly flexible impermeable membrane at the side walls of our train track model, Wu *et al.* (2004) and Mirbod *et al.* (2009b).

**4.** As quantitatively predicted for the red cell in Weinbaum *et al.* (2003), if the elastic restoring force of the solid phase is small, the sliding friction will be greatly reduced since this frictional force is proportional to the contact force of the fibers in the solid phase. In our train-track model, we try to trap the air inside the porous track so the air provides most of the lift and the sliding friction is greatly reduced, Wu *et al.* (2004) and Mirbod *et al.* (2009b).

**5.** In Wu *et al.* (2005) experiments were performed to measure the characteristic time for the excess pore pressure to decay during skiing for different snow conditions. These results were then applied in Wu *et al.* (2006) to theoretically predict the fraction of the total lift force provided by the air that was transiently trapped beneath a ski or snowboard. They found that for fine powder about one half of the total lift for a snowboard comes from the air and about 40% for a ski when traveling at 10 m/s.

**6.** In chapter 2, the generalized theory derived in F&W was extended to random porous materials by using a Carman-Kozeny equation for a random fibrous array and initial predictions were made for the lift force that would be generated by the air phase using a one-dimensional analysis which assumed that there is no leakage

along the lateral edges of the planform since the soft porous track was confined in a channel with impermeable sidewalls. In addition, we examine the dramatically different behavior that is obtained depending on whether the porous medium is attached to a stationary horizontal lower boundary or to a moving inclined upper boundary. As a result, we showed that if lateral leakage can be eliminated it is possible in the first case to lift enormous loads that are order $\alpha^2$ greater than classical lubrication theory; for example it is possible to lift a 70 metric ton train car with a $Kp < 5x\ 10^{-9}\ m^2$ at a velocity >5 m/s.

**7.** In chapter 3, the performance criteria for an airborne jet train with weight of 70 metric tons, carrying 200 passengers gliding on a soft fibrous track was developed. Using random porous media theory, Mirbod *et al.* (2009a) predicted that one can achieve lift-off at only 5 m/s if the porous material has a fiber radius of 5μm, a solid fraction of 0.005 and $Kp=3.4 \times 10^{-9}\ m^2$. In addition, we showed that a porous track with polyester fibers with these properties is nearly frictionless. One class of materials with these properties is the soft polyester fiber-fill that is commonly used in inexpensive body pillows with 95% polyester and 5% silk. Furthermore, the required thrust needed to approach velocities comparable to commercial jet aircraft was only 10,000 lbf or about 1/5 that of commercial jets carrying the same passenger load. This can be achieved because the train rises only 4 cm at its trailing edge before it becomes airborne so there is negligible lift induced drag and also one does not have to climb to altitude. Since energy expenditure is thrust times distance, fuel consumption should be less than 1/5 that of commercial jets. Also combustion

products are not released high in the atmosphere where global warming effects are greatest.

**8.** The studies in chapters 2 and 3 were the catalyst for performing experiments to examine the generation of dynamic lift forces during rapid compaction loading of soft porous materials presented in Appendix I. Several porous materials have been tested and one commercially available material with 95% polyester and 5% silk composition, our proposed fibrous media, provided the most promising results. Novel experimental techniques have been developed to measure the dynamic forces acting on the compressing piston by the air and solid phases. The measurements demonstrate that the excess pore pressure builds up inside the porous material during sudden compression which is large enough to temporarily support huge weights, Al-Chidiac *et al.* (2009). In Appendix II, a preliminary laboratory experiment has been designed and constructed to measure the time dependent pressure beneath the ski. These results are in reasonable agreement with our theoretical calculations.

## 4.1 Future work

The following tasks are suggested for the future research:

**Task (1):** We propose to build a 1/10 scale, instrumented laboratory scale model of the AJT, pulled by a constant velocity motor including a realistically designed superstructure. The basic design parameters of the laboratory model such as its velocity, weight and tilt angle will be predicted using the theory in Mirbod *et al.* (2009b). In particular, we will determine the velocity required to support the model as a function of its compression ratio and also the take-off speed of the

model. As indicated in Appendix II, an initial smaller laboratory train track model has been designed which suggests peak values close to the theoretical calculations without leakage. This proof of concept paves the way for a more realistic model of the ski-train with a suitable superstructure representing the AJT to test the performance predictions in Mirbod *et al.* (2009b). This model also will examine the effect of key input parameters such as the thickness of the porous bed and its aspect ratio W/h, the clearance gap at the sidewalls and the location of the c.g. on pitching stability. In addition, Particle Image Velocimetry will be used to obtain qualitative and quantitative information of the velocity field around the front and rear of the overstructure.

**Task (2):** Since pressures as high as 18kPa build up beneath the AJT one anticipates that significant lateral leakage can occur depending on the width of the clearance gap between the ski and the channel sidewalls. To our knowledge there is no prior theory for the effect of leakage in confined soft porous media. One notes that the closest models are probably for our model track where air is vented through an entire sidewall as opposed to a narrow gap of width "δ" as shown in Fig. 4.1. This leakage per unit length q(x) is proportional to the difference in pressure between centerline of the track and the external pressure $P_a$. In the absence of lateral leakage the pressure beneath the planform is nearly uniform in the span-wise direction. This will change significantly if the leakage is an important fraction of the air that is being shoved forward by the advancing ski. The leakage rate is given by $q(x) = \beta(P - P_a)$ where β is a leakage coefficient. From dimensional analysis one can show that β is a function of two parameters $\delta/\sqrt{Kp}$ and h/W the aspect ratio of the cross section, where h is the fiber layer thickness and W is the width of the

track. To determine β one needs to develop a model for the flow in the cross-sectional plane for our model track. The predictions of this theory will be compared with an experiment in which a board of a known weight with a prescribed clearance "δ" will be allowed to settle in the channel and its settling velocity and centerline pressure measured. The detailed pressure distribution in the channel cross-section will be predicted using a time dependent 2-D, Darcy flow theory applied to the flow geometry in Fig. 4.1 for a time varying settling velocity dh/dt. The predicted centerline pressure will then be compared with its measured value. These solutions will be used to define a parametric family of transverse pressure profiles to describe the pressure beneath the ski and to determine the value of β as a function of $\delta/\sqrt{Kp}$ and h/w. The leakage term is then set equal to dQ/dx where Q is the total axial flow in the cross-section and a governing equation derived for the centerline pressure at any x. The theoretical model will then be used to scale the results of the laboratory model to the actual ski on the AJT so that the sensitivity of the pressure loss to the size of the clearance gap can be estimated for the prototype.

**Task (3):** The fast moving train creates an upstream effect which causes sub-atmospheric pressure fields along the edges of the front surface which may interfere with the above-atmospheric pressure field developing inside the porous track. Similarly, the sub-atmospheric pressure in the wake of the train may attenuate the peak pore pressure which is formed closer to the trailing edge than the leading edge of the ski. It is very difficult to accurately estimate these effects but a combined computational and experimental approach can be used to put bounds on the magnitude of the changes in the front and rear pressures generated by the passage of the AJT. Note that only modest effects should be felt above the ski since it is largely

protected by front and side panels that extend nearly to the surface of the track. In order to address this issue of interference and obtain reasonable estimates of the pressure distributions in the front and rear of the model, one can perform CFD calculations using Fluent. In addition, one can carry out wind tunnel testing of the laboratory model in which the drag force and the pressure distribution in the vicinity of the front and rear surfaces of the superstructure will be measured in the absence of a porous track, but in the presence of a moving wall. This information will be inserted into the theoretical model which includes the porous track to obtain the pressure distribution beneath the planform for various values of the non-dimensional parameters. The wind tunnel will consist of the PIV system and other resources.

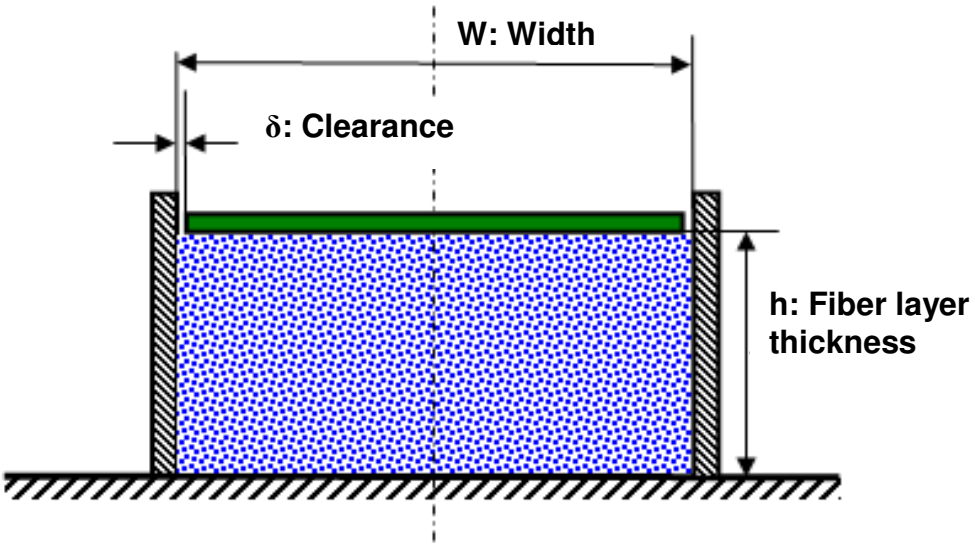


Figure 4.1 Cross section of the model train indicating the clearance between the side walls and sliding train.

# Appendix I. Dynamic compaction of soft compressible porous materials: experiments on air-solid phase interaction

## I.1 Introduction

Whereas the flow inside porous media and the mechanical behavior of the solid phase of porous materials have been extensively studied in the past, relatively little attention has been paid to highly compressible soft porous materials because these materials are traditionally thought to be structurally fragile and support little weight unless highly compressed. In the past such materials were largely used in pillows. This view was dramatically changed as a result of the theoretical investigation by Feng and Weinbaum (2000), hereafter referred to as F&W, which demonstrated that these materials could transiently support very large loads beneath a planing surface for short duration if the trapped fluid within the fibrous medium could not escape on the time scale of the passage of the planing surface. The basic idea was first conceptualized in trying to explain the "pop out" phenomena that was observed in the motion of red blood cells (RBCs) in capillaries. At velocities < 20 μm/s the RBCs were observed to glide on a compressed endothelial surface layer (ESL) of sulfated proteoglycans and glycoproteins that line the endothelial cells (ECs) of our entire microcirculation and that when the motion of the RBC was arrested the ESL collapsed and the RBC filled the entire lumen of the capillary, Weinbaum *et al.* (2007). F&W showed that there is a remarkable hydrodynamic similarity between the motion of the RBC and a human skier or snowboarder skiing on soft snow powder even though their difference in mass is of order $10^{15}$. F&W predicted that the excess pore pressure generated by a planing surface moving on any highly compressible porous media, including snow, scales as $\alpha^2 = h^2/K_p$, where

h is the layer thickness and $K_p$ is the Darcy permeability and that this excess pressure is attenuated as $(L/W)^{-2}$, where L/W is the aspect ratio of the planing surface, if there is leakage at the lateral edges of the planform. The theory in F&W shows that $\alpha$ is of order $10^2$ or larger for both red blood cells gliding on the ESL and for a human being skiing. Thus, the lift forces generated can be four or more orders of magnitude greater than classical lubrication theory in the case of the RBC in a tightly fitting capillary where there is no lateral leakage, whereas for a human skiing this lift is reduced by roughly a factor of 400 due to the escape of air at the lateral edges. Despite this leakage Wu et al (2006) predicted that fully 50 percent of the total lift on a snowboard traveling at 10 m/s arose from the excess pore pressure that developed due to the transiently trapped air beneath the snowboard and the increased hydraulic resistance of the compressed snow.

The present Appendix utilizes the porous cylinder-piston apparatus first described in Wu *et al.* (2004, 2005). In Wu et al (2004) this novel apparatus was used to measure for the first time the dynamic pressures that develop on the centerline of the cylinder on the time scale of skiing or snowboarding. Wu *et al.* (2004) also conducted experiments to determine the Darcy permeability of feathers from down pillows. The authors predicted that it might be possible to support the weight of a fast moving train using a giant ski that glided on synthetic materials with the properties of down feathers using a novel track that consisted of a channel with impermeable side walls that eliminated or greatly reduced lateral leakage. The cylinder–piston apparatus was further refined in Wu *et al.* (2005) and more detailed measurements made to determine the time dependent pressure profiles that develop beneath the piston for different snow types and the results interpreted using

consolidation theory. However, in both these studies only the excess pore pressure due to the air was measured after the weighted piston was dropped. In contrast, in the present investigation we also use a load cell to simultaneously measure the total pressure due to both the air and solid phases. This allows us separate out the transient pressure due to the air and solid phases. This is particularly important in determining the friction force on a moving planform since the latter force is proportional to the applied force of only the solid phase since the air friction force is small.

The immediate catalysts for this appendix are two recent papers by Mirbod *et al.* (2009a, b). In Mirbod *et al.* (2009a) the theory developed in F&W is extended to the generation of lift forces in random porous media. The authors examine the dramatic difference in behavior that is obtained depending on whether the porous medium is attached to a stationary horizontal lower boundary or to a moving inclined upper boundary in a channel with impermeable sidewalls. The second paper develops the performance criteria for an airborne jet train (AJT) carrying 200 passengers gliding on such a track. Using random porous media theory and the Carman–Kozeny equation (see Happel and Brenner 1983), Mirbod *et al.* (2009b) predicted that one can achieve lift-off at only 5 m/s if the porous material has a fiber radius of 5μm and a solid fraction of 0.005. Furthermore, the required thrust needed to approach velocities comparable to commercial jet aircraft is only 10,000 lbf or about 1/5 that of commercial jets carrying 200 passengers. Since the train rises only 4 cm at its trailing edge before it becomes airborne there is negligible lift induced drag. An inexpensive polyester fiber-fill material has been identified with these

properties. It is the properties of this material that will be examined in all the experiments described in this chapter.

According to the theory of Wu *et al.* (2005) both the build up and the drainage of the pore pressure within the cylinder exhibit a time-dependent quasi-steady behavior that is governed by Darcy's law, the instantaneous supporting force of the fibers and the conservation of mass for both the air and the solid phase. The weight of the piston is balanced by its inertia, the time varying integrated pressure force of the transiently trapped air and the supporting force of the solid-phase. The latter is determined directly from a separate static experiment in which small weights are gradually added to a light weight piston and the compression of the fiber-fill layer measured as a function of the applied force until the full weight of the piston in the dynamic experiment is achieved. One finds that the maximum compression depends on the elastic properties of the fiber-fill layer and its initial depth, but if the compression is scaled relative to the maximum compression and the force relative to the maximum force, the dimensionless empirical relation is nearly independent of the weight of the piston with its load. The theoretical model is, therefore, able to predict the time-dependent variation of each force if one can take account of the change in permeability of the fiber layer as a function of its compression. No direct measurement of the dynamic fiber force has been attempted in Wu *et al.* (2005).

One of the parameters governing the dynamic compaction of porous media is the square of the ratio of the two time scales $\gamma = (t_g/t_v)^2$ where $t_g = (h_0/g)^{1/2}$ is the gravitational time scale and $t_v$ is the viscous draining time scale given by

$t_v = \frac{\mu_v R^2 (1-\phi_0)}{P_w K_p}$ where $\phi_0$ is the initial porosity, $P_w$ is the applied pressure on the piston, $\mu_v$ is the viscosity and $K_p$ is the permeability.

This Appendix is organized into four sections. In § 2, details of the experimental set-up used in the dynamic and static experiments are provided. The results are described in § 3. This section includes a discussion of the results obtained in the dynamic experiments and material characterization tests under static conditions. The effects of friction forces and strain rates during the fiber compression are discussed in this section. Finally, in § 4 we conclude by discussing the major implications of the Appendix.

## I.2 Experimental set-up

### I.2.1 Dynamic compression experiments

These experiments were carried out by using the same piston/cylinder apparatus used in our previous snow experiments (Wu *et al.*, 2005; Wu *et al.*, 2004) which provided the first experimental demonstration of the excess pore pressure predicted by the F&W theory. This apparatus has been modified in the present work by adding a force measurement system which provided information used to estimate independently the solid and air phase forces acting on the piston during the dynamic compression. Figure I.1 shows a schematic of the piston/cylinder apparatus. It consists of a cylindrical sidewall which is porous and is attached to a solid base plate. A light piston that can carry additional fixed weights can slide freely along the inner surface of the cylindrical porous sidewall and provide a uniform loading to the porous media. Rigimesh was used to form the desired cylindrical surface.

Rigimesh is an arrangement of several screens sintered together for more rigidity. The mesh provides a negligible airflow resistance.

A detail description of the apparatus can be found in Wu *et al.*, (2005). A high sensitivity and high frequency response load cell type Honeywell model MBL was used to measure forces during dynamic compression. A thin aluminum plate of 25.4 mm in diameter was firmly attached to the cells' 5mm in diameter piston/rod so that the sensing area is amplified. This plate-load cell arrangement was fitted in an enclosure which was attached to the larger compacting piston so that no pressure leaks could occur. This load-cell-based-force-measuring system was installed at a location 19 mm off the piston's center (see figure I.1(b)). The information provided by the two nearby pressure transducers was used to determine the pore pressure of the air phase and then decouple it from the solid-phase force. Additional information provided by two accelerometers type EGAX-25-C200001 fabricated by Entran (Measurement Specialties) was used to estimate the effect of inertia forces on the force measuring system and the moving piston.

Seven high-frequency-response sub-miniature differential pressure transducers fabricated by Kulite Semiconductor Products (model XCS-062-5-D) and Entran (model EPX) were installed on the apparatus to measure the time-dependent pore-pressure distribution inside the fiber layer and its spatial variation under rapid compression. One transducer was fixed at the center of the piston; five were installed on the piston at distances 0.19R, 0.33R, 0.48R, 0,62R and 0.77R away from the center, respectively, where R is the radius of the piston; and the last one was installed inside the porous material along the centerline of the cylinder at 40mm height. The inner diameter of each transducer is 1mm, which is small enough

to ensure good spatial resolution of the local pressure measurement. The pressure transducers were powered by a 9-V battery and calibrated in a small portable pressure chamber with controllable pressure. The electrical outputs were filtered and amplified by multi channel Iotech Filter 488/8 and signal conditioners and then digitized by an Iotech ADC488/8SA data acquisition system with 16 bit resolution. Finally, the signals were transferred to a computer for further processing.

Our instrumented apparatus can not only measure the transient pore pressure response to rapid deformation, but also its spatial variation along the radial direction and across the depth of the fibers. The latter is needed to address the question as to whether the fiber beneath the piston is relatively uniformly compressed. This non-uniformity in density can be observed with the pressure distribution measurement along the vertical centerline of our porous cylinder- piston apparatus.

The apparatus was filled with fiber in layers to a height of ~14 cm. The piston was weighted and then released under gravity to compress the fibers. The tolerance between the piston and the cylinder wall is large enough to allow the piston to drop with little friction between the sliding surfaces. The air leakage through this narrow gap is negligible compared to the porous side wall. The depth of the fiber layer before and after the compression, and its mass were measured to determine the initial and final density and porosity.

Four different porous materials were tested. They are regular polyester pillow materials obtained in local retail stores. One, however, consisting of 95% polyester and 5% silk, fabricated by Mountain Mist (Heritage Collection) outperformed the others. The results presented here have been obtained in experiments with this material which had fibers of 10 μm diameter that provided low flexural rigidity *EI*

where $E$ is Young's modulus and $I$ is the moment of inertia of the fiber cross-section.

## I.2.2 Static compression experiments

To gain insight into the mechanical properties of the solid phase in the absence of piston inertia and excess pore pressure, we have measured the quasi-steady force generated when the fiber material is subject to incrementally increasing compressive forces. The load is added gradually to the piston so that the air in the pores could freely escape without elevating the pore pressure in contrast to the dynamic experiments in which the air in the pores is temporarily trapped before it escapes. This has also made it possible to separate out the inertial effect associated with the acceleration and deceleration of the piston. The apparatus described in the previous section for the dynamic compaction of porous media was used to determine the relation between applied quasi-static stress and displacement. This will enable us to obtain realistic estimates of the stress that is applied by the solid phase as the compression proceeds. The deformation of the porous material sample was measured immediately after the load application. Thus, creep deformation was excluded.

Figure I.2 shows three typical incremental loading/unloading curve sequences for a static compression test on fibers with an initial porosity of 0.98. The results in figure I.2 indicate that the supporting force from the solid phase of the fiber sample increases with increasing deformation in a non-linear way. In addition, a significant hysteresis can be observed during the quasi-static unloading. The maximum deformation measured in these experiments is between 50 and 60% of the

undeformed height of the fiber porous layer, $h_0$. This experimentally determined force-displacement profile can be used to estimate the increasing force that the solid fiber phase would exert on the falling piston during the dynamic compression experiments and also to compare it with the directly measured force obtained with the load cell.

### I.2.3 Accelerometer tests

The piston instrumented with the accelerometers, the pressure transducers and the load cell was tested in a free fall experiment in order to acquire information on the performance of the three different measuring systems, particularly, with reference to electronic noise levels and interference. In addition this test was used to calibrate the accelerometers. The recorded accelerometer output, shown in Figure I.3, reveals some interesting behavior on how the acceleration of gravity is eventually settled. The free falling phase of the piston has two distinguishable parts, the slow one which lasts about 40 ms during which the amplitude reaches only 25% of its final value and the fast decreasing part in a step change fashion which is of the order of 1 ms in duration. The first part is affected by the manual release of the piston by the operator while the second fast part is controlled by the frequency response of the accelerometers which is of the order of 1 kHz. Thus the onset of gravity acceleration has a slow responding part which is due to the manual release of the piston. The constant value of output voltage reached after 0.13 s corresponds to the gravity acceleration and it is used to calibrate the accelerometer.

## I.3 Results

Five experiments were carried out with different weights on the piston. They are listed in Table I.1. In all cases the initial density of the fiber was the same, while the terminal one at the end of compaction differed due to different applied load.

Figure I.4 shows the time-dependent pressure signals during a typical test in the case of the experiment with Load #5. The signals were obtained from eight pressure transducers on the piston and inside the porous medium located at positions shown in figure I.1. The peak value of pressure at the center of the piston is about 600 Pa, roughly 20% lower than the average normal pressure applied on the bottom surface of the piston (745 Pa). The pore pressure builds to its peak value within ~0.15 s, and then relaxes on a time scale (~0.05 s) which is three times faster than the compression scale. These times are very close to the gravitational time scale $t_g=(h_0/g)^{1/2}$ =0.12 s and the viscous draining time scale $t_v$ which is of order of 0.066 s. This differs greatly with the wind-packed snow crushing experiments reported in Wu *et al.* (2005) where the time scale of relaxation is about six times larger than the compaction time scale. However, there is some similarity with the case of fresh snow during compaction, where there is no extended pressure relaxation phase because the dimensions of the piston are too small and the value of permeability K too large for the excess pore pressure to support the full piston weight. One also notices a damping oscillation of the piston motion with a sub-atmospheric vacuum pressure that is created before the pore pressure finally returns to atmospheric pressure.

Another interesting observation is that there is a small pressure difference of 40 Pa between transducers $P_1$ and $P_8$ which is about 0.066 of the maximum pressure

$p_{max}$ =600 Pa. This suggests a pressure gradient in the vertical direction whose average value is $(\Delta p/\Delta z)_{r=0}$ =40/(100-40)=0.66 Pa/mm where $\Delta z$ is the distance between the piston and the pressure transducer $P_8$ at the time when the maximum pressure is measured at transducer $P_1$. This occurs when $\Delta h$ is about $0.8\Delta h_{max}$. The maximum value of $\Delta p/\Delta z$ occurs at the center of the cylinder and becomes zero at its periphery r=R. The pressure gradient in the radial direction is estimated to be about 5 to 6 times larger. Similar estimates of the vertical pressure gradient at the symmetry axis of the cylinder have been found in our CFD work (not shown here).

Some further insight into the interaction between the compressed fiber and the flow through the pores has been obtained by carrying out several decompression experiments by suddenly removing the applied load on the piston. In this trial testing, the operator lifts manually the piston with its weights, some considerable time after the completion of the compression experiments. Unlike the case of compression where the free falling piston acquires gravitational acceleration shortly after its release by the operator, the unloading experiments are characterized by the influence of the manual operation which was not under constant velocity or acceleration. Nevertheless the results indicated some interesting behavior and the pressure results are shown in figure I.5. These pressure signals have been obtained by the pressure transducers during unloading of the piston in the case of the Load #5 experiment. Negative i.e. sub-atmospheric pressures have been observed in all locations indicative of air flow in the direction towards the center of the porous medium. As the piston moves upwards its displacement creates a vacuum pressure which sets up a pressure gradient driving air at atmospheric conditions into the porous medium. The maximum generated vacuum pressure takes place at the center

of the piston and occurs about 0.1 s after the beginning of the unloading. Then, the pressure field returns to atmospheric pressure after a long and monotonic relaxation process with time scale about 0.5 s.

The distribution of maximum pressure of each of the pressure signals in the radial direction beneath the piston during the compression and decompression experiments in the case of Load #5 is shown in Figure I.6(a). The data have been normalized by the applied load $P_w$. Pore pressures during compression are about four times greater than vacuum pressures developed during decompression. In order to provide information on azimuthal inhomogeneities of the fiber distribution the piston has been rotated 90 and 180 degrees from each original angular position. The acquired data were compared with the original one at each radial position and the error bars in the graph indicate the range of this variation. In terms of standard deviation the actual error is about 4%.

The theories of Feng & Weinbaum (2000) and Wu *et al.* (2005) assume a parabolic distribution in the radial direction at each time step and the present data of maximum pressure shown in Fig. I.6 seem to closely approximate that. The deviation from the parabolic distribution near the cylinder walls is likely due to the constrained radial expansion of the fibers and the friction forces that are generated by the Rigimesh. This expansion is absent for snow compaction.

The build-up of the pressure field throughout the porous medium field is also of interest. The present data as well as the work of Wu *et al.* have shown that pressure normal to the piston direction changes very little with distance at any time during the process of compaction. Pressure changes, however, in the radial direction are substantial. Figure I.6(b) shows the pressure distribution in the radial direction

at five different time steps. The data shows that the pressure build up is very gradual with higher pressure in the middle of the piston and lower pressure toward the edge of the piston where pressure adjusts to the atmospheric boundary condition. The time scale of this build up is of the order of 0.15s. Biot's general theory of two- and three-dimensional compression of porous medium described in Biot (1941) and Biot and Willis (1957) assumes compression wave propagation with the speed of sound. The imposition of the pressure field through compressive waves undergoing multiple reflections over the surfaces of the apparatus is of the order of $10^{-4}$ s and therefore it takes place on a scale that is much shorter than the viscous scales measured here which are very well described by the time-dependent quasi-steady behavior of Reynolds equation and Darcy's law.

Balance of forces acting on the load-cell was used to decompose the measured force into the solid-phase force $F_{C,s}$ , the air-phase force $F_{C,air}$, and the inertia force $m_C(a+g)$ where $m_C$ is the mass of the load-cell piston, a is its acceleration $d^2h/dt^2$ and g is the gravity acceleration. A closer look into the load-cell design and construction indicated that there is no relative motion between the sensor and the cell's force transmitting piston/rod. In addition, due to the small mass of the sensing area, only 4 grams, the inertia force was negligible. Thus, the measured force by the load-cell is balanced by the contributing individual phase forces, $F_{C,M}= F_{C,s} + F_{C,air}$. The air phase force was obtained from the nearby pressure transducers $P_1$ and $P_2$, one on the left and a second on the right side of the load cell, by averaging the two pore pressure measurements and multiplying by the sensing area of the load cell, $A_C$, through the approximation $F_{C,air} = \int_{A_C} p dA = \frac{p_1 + p_2}{2} A_C$ .

Typical measured time-dependent signals of forces are shown in figure I.7. The total force starts to increase with the onset of dynamic compaction at time 0.9 s and peaks at 1.1 s. During the first 0.15 s of the compression process, the pore air pressure force supports the cell's piston completely. The peak air-phase force appears to be 0.275 N which is about 68% of the 0.4 N applied static force. This appears to be the portion of the applied piston weight force acting on the sensing area of the load cell. The solid-phase force, which affects friction in the case of a moving plane, is negligible. After this time the air phase force drops quickly due to pressure venting related processes, the solid phase starts to increase rapidly and at time 1.1 s it supports the cell completely. At this time, some oscillations can be observed in all forces due to the piston rebound, which are damped entirely for t >1.255.

Figure I.8 shows the forces acting on the piston and fiber. For the case of the piston equilibrium, balance of forces requires that

$$M\frac{d^2h}{dt^2} = -Mg + F_a + F_s \qquad \text{(I.1)}$$

where M is the combined mass of the piston and applied weights W=Mg, $F_a$ is the surface integral of the dynamic pore pressure on the piston and $F_s$ is the resistance force due to the solid phase which is provided by the load cell and which does not change with radial position. A representative example of this dynamic balance of forces is shown in figure I.9(a) for one of the several cases of loading which we tested. All quantities are normalized by Mg. The summation of all normalized forces at any time must equal unity. In the initial stages of the compression, the force due to the pore pressure builds up very slowly and is

counterbalanced solely by the inertial force of the piston. Close to $P_{max}$ the piston achieves its maximum downward velocity, the inertial force is quickly reduced and the solid phase force starts to increase.

It is evident from these data that during the time when $F_a$ is increasing, the solid-phase force $F_s$ is quite small. The time scale of the rise of the pore pressure is about 0.15 s while the loss of air-phase force support due to air venting is more than three times faster. At its peak, $F_a$ supplies about 40% of the total lift force acting on the piston. As a result of the piston rebound, the measured force overshoots its relaxation equilibrium value by about 50% and damped oscillations appear in all signals.

The acceleration signal has been integrated twice to obtain the time-dependent displacement of the piston. In addition to the acceleration measured by the accelerometers, acceleration was also computed from the force balance (1). The displacement obtained through successive integration of the measured acceleration in this particular case and that computed by difference in the force balance are plotted in figure I.9(b). There is some disagreement between the two displacement signals which is of the order of 24% and is most pronounced in the beginning of the compression where gravitational acceleration is not set immediately as demonstrated in figure I.3. The two instruments, i.e. load cell and accelerometer, are different with different phase characteristics and when their outputs are integrated twice, initially small differences are accumulated to yield this 24% difference. This process of calculating distance from acceleration through successive integrations is known to be very sensitive to initial conditions and, therefore, rather inaccurate. The terminal static equilibrium position of the piston measured directly at the end of

the compression is close to the values of the computed displacements. It is evident from figure I.9(a) that at the time of maximum air phase force, the material has been compressed more than 70% of its final deformation 0.63.

These dynamic compression experiments clearly demonstrate the significant potential of soft porous materials in engineering applications where a sudden compression can generate peak pore pressures which can temporarily support a substantial portion of the applied normal stress.

## I.3.1 Further material characterization

Additional tests were carried out to determine the lateral or transverse deformation of the fiber during static compression and the resulting frictional forces acting on the fiber by the cylinder wall. Several experiments were carried out to determine the transverse or radial strain, $\Delta R/R$, concurrently with the axial one $\Delta h/h_0$. $\Delta R$ and $\Delta h$ are the radial and vertical deformations respectively. The ratio of these two relative deformations is Poisson's ratio defined as

$$\nu=-\Delta R/R/\Delta h/h_0. \qquad \text{(I.2)}$$

In one of the experiments which were conducted outside the cylinder/piston apparatus i.e. in the absence of a confined wall with the same specimen, the strains during decompression were also recorded. The results are shown in figures I.10(a) where Poisson's ratio is plotted against applied force/stress. It appears that Poisson's ratio increases reasonably quickly with the onset of the load and then practically remains constant during the duration of the compression with a value of 0.1. These data, which represent the bulk radial deformation since no height dependence was determined, clearly suggest that the lateral deformation is

substantial. There is also a hysteresis during decompression of the porous material evident in both figures.

The same lateral deformation data together with the normal deformation data are plotted in figure I.10(b) against the applied stress data normalized by their maximum value. A set of data of the normal deformation data obtained inside the cylinder/piston apparatus is also plotted in the same figure. It is evident that for the same applied normalized stress the deformation $-\Delta h/h_0$ is larger in the case of unconfined compression. Another key difference between the confined-by-the-walls compression and the unconfined-by-the-walls compression is the hysteresis effect which seems to be considerably less in the case of the laterally unconfined axial compression/decompression.

The development of lateral deformation during normal compression is a characteristic of the present material which is in contrast to the behavior of snow which under one dimensional dynamic compaction showed no signs of lateral deformation. Thus, the theoretical model to predict the excess pore pressure in snow can be described using Terzaghi's (1943) one dimensional consolidation theory.

The data in figure I.10 will be used to estimate the lateral/radial stress $\sigma_r$ exerted in the case of the cylinder/piston compression experiments.

The generalized Hook's law relations in 2-D axisymmetric compression are:

$$\varepsilon_z = \frac{1}{E}[\sigma_z - \nu(\sigma_r + \sigma_\theta)],$$

$$\varepsilon_r = \frac{1}{E}[\sigma_r - \nu(\sigma_z + \sigma_\theta)]$$

And

$$\varepsilon_\theta = \frac{1}{E}[\sigma_\theta - \nu(\sigma_z + \sigma_r)] \qquad \text{(I.3)}$$

The strains are defined as $\varepsilon_z = \frac{\partial u_z}{\partial z}, \varepsilon_r = \frac{\partial u_r}{\partial r}$ and $\varepsilon_\theta = \frac{1}{r}\frac{\partial u_\theta}{\partial \theta} + \frac{u_r}{r}$ where $u_z$, $u_r$ and $u_\theta$ are the particle displacements in the vertical, radial and azimuthal directions. We are interested in determining the radial stress $\sigma_r$ at the periphery of the piston where r=R. The axial compressive strain is $\varepsilon_z$=-$\Delta h/h_0$ and the relative change in volume is also the same $\varepsilon_V$=-$\Delta h/h_0$. Therefore, for small deformations it is $\varepsilon_V \approx \varepsilon_z + \varepsilon_r + \varepsilon_\theta$ which implies that $\varepsilon_r + \varepsilon_\theta \approx 0$. Since the boundary at r=R is rigid, it is reasonable to assume $\varepsilon_\theta \approx 0$. Thus, $\varepsilon_r \approx 0$ and $\sigma_r = \sigma_\theta = \frac{\nu}{1-\nu}\sigma_z$.

These relations are valid for pure elastic materials which are incompressible with small deformations. The present porous material is not elastic but the whole process of compression/decompression can be considered as piecewise elastic. The process can be sub-divided into various short domains where elastic behavior can be assumed and the above relations can be used. The value of E is not the same in each of these sub-domains.

During the experiments to determine $\nu$ i.e. in the absence of a restricting wall, these relations become $\varepsilon_z = \frac{\sigma_z}{E}$ and $\varepsilon_r = \frac{\nu\sigma_z}{E}$ with $\sigma_r$=0. In the case of the experiments within the cylinder/piston apparatus the confining walls result in $\varepsilon_r = 0$ which leads to the relation

$$\sigma_r = \frac{\nu}{1-\nu}\sigma_z \qquad \text{(I.4)}$$

and, therefore,

$$\varepsilon_z = \frac{1}{E}\left[\frac{1-\nu-2\nu^2}{1-\nu}\right]\sigma_z . \qquad (I.5)$$

Relation (I.4) can provide the lateral i.e. radial force $F_R$ generated by the bulging material which is acting on the cylindrical walls of the apparatus. Then

$$\frac{F_R}{F_{max}} = 2\frac{\nu}{1-\nu}\frac{h}{R}\frac{F_z}{F_{max}} \qquad (I.6)$$

where h is the current depth of the material and $F_{max}$ is the maximum applied load. The data for $\Delta h/h_0$ and $F_z/F_{max}$ of the experiment shown in figure I.2 have been used to estimate the ratio $F_R/F_{max}$. The values of ν from exp#1 of figure I.10(a) were used to estimate the value of the lateral force $F_R/F_{max}$. The results are shown in figure I.11. It appears that the lateral force is only 12% of the $F_{max}$. However, this force is comparable to $F_z$, particularly at small compression ratios.

## I.3.2 The effects of friction under fiber compression

The substantial magnitudes of the lateral deformation and the radial force, $F_R$, that develop during the fiber compression, indicate that friction forces between the fiber and the inner wall surface of the cylindrical container may not be negligible. An experiment was designed to estimate the friction forces directly under various compression ratios $\Delta h/h_0$.

The fiber was constrained by two rigid discs of slightly smaller diameter than the diameter of the cylinder and minimum thickness made out of light weight compressed paper, cut out from the back of a paper pad, as shown in figure I.12. Three pieces of string were used to keep the fiber and the two discs together under known tension. Knots at fixed locations were tied on the strings in order to provide

the desired compression length h under the corresponding force $F_s$. The fiber, strings and discs assembly was set to a prescribed length and a hand held dynamometer was used to read the applied force necessary to maintain a reasonably constant motion of the fiber assembly. This force was about twenty percent smaller than the force needed to initially overcome the static friction. Due to the short traveling distances of the assembly there is considerable uncertainty in estimating friction forces, particularly at low compression ratios $\Delta h/h_0$.

Figure I.13(a) shows the frictional shear stress $\tau_f = F_f / 2\pi Rh$ at various compression ratios $\Delta h/h_0$. It is very interesting to observe that friction forces increase with increased compression in a non-linear way. A three plus fold compression results in a five-fold increase in shear stress. The friction coefficient μ, defined through the relation $F_f=\mu F_R$, has been computed by using equation (I.6) to estimate $F_R$. The results obtained by the relation

$$\mu = \frac{(1-\nu)}{\nu}\frac{R}{2h}\frac{F_f}{F_z} = \frac{(1-\nu)}{\nu}\frac{\tau_f}{\sigma_z} \tag{I.7}$$

are shown in figure I.13(b) where they are plotted at various compression ratios. The values of μ range from 2.4 at small compression ratios to 2.5 at large compression ratios. These large values are due first to the roughness of the inner cylindrical surface and second to its pores which tangle and grab the fibers of the material during its motion. Friction coefficients obtained during constant motion of the same material under compressive tension inside a smooth plexiglass tube had values roughly half of the values measured inside the present cylinder apparatus. Both experiments showed that μ is more or less independent of compression ratio $\Delta h/h_0$. The reason for this behavior is that Poisson's ratio ν is reasonably constant

during most of the compression except at the beginning and that $\tau_f$ and $\sigma_z$ vary similarly with $\Delta h/h_0$. Thus, the friction coefficient $\mu$ depends mostly on the surface roughness and porosity and the fiber material rather than on the values of $\Delta h/h_0$ or the values of $\tau_f$ and $\sigma_z$ as is usually the case.

### I.3.3 Strain rate effects and the mutual interaction

If we consider the free body diagram of the fiber as shown in figure I.8, the opposite forces $-F_s$ and $-F_a$ act on the fiber together with the reaction force from the bottom wall, $R_w$ which can be decomposed in to its solid and air phase components, $F_{s,w}$, $F_{a,w}$ respectively, $R_w=F_{a,w}+F_{s,w}$. Balance of forces acting on the fiber of mass $m_f$ requires that

$$m_f a = -m_f g - F_a - F_s + R_w + F_f \tag{I.8}$$

In the present approach, all these forces represent point forces which are obtained after integration over their distributed values. In that respect, the acceleration, a, is not the same as the piston's acceleration, $d^2h/dt^2$ because the top surface of the fiber moves with the piston while the bottom surface remains still. By combining equations (I.1) and (I.8) or by considering the combined two-body equilibrium the following relation is obtained

$$M\frac{d^2h}{dt^2} + m_f a = -(M + m_f)g + F_f + R_w \tag{I.9}$$

The mass of the fiber is at most about 0.05 to 0.1 of the mass of the piston, M and its equivalent averaged acceleration, a, is smaller than $d^2h/dt^2$ and therefore the corresponding terms can be neglected in equation (I.9). Thus

$$M\frac{d^2h}{dt^2} = -Mg + F_f + R_w = -Mg + F_f + F_{a,w} + F_{s,w} \tag{I.10}$$

As it was shown earlier in figure I.4, the air phase pressure force changes slightly with depth and therefore $F_a=F_{a,w}.+ \Delta F_a$ where $\Delta F_a$ is the difference in air force between the piston and the bottom surface due to the small vertical pressure gradient. If $dA_p = 2\pi rdr$ is the area of a ring on the piston with an infinitesimally small thickness dr and h the distance of the piston from the wall then $\Delta F_a = \int_0^R 2\pi r( p_a - p_{a,w} )dr$ where $p_{a,w}$ is the pressure distribution on the bottom surface. In Wu et al (2005b) the pressure distribution along the axis of a stagnation point flow in a porous media of infinite width is derived. In the large $\alpha$ limit this pressure decrease is shown to be parabolic, [see equation (49)]. Pressure measurements at transducers 1 and 8 can, therefore, be used to extrapolate the pressure at r = 0 on the bottom wall assuming a parabolic profile. At r = R, $p_a$ and $p_{w,a}$ are the same. In the absence of actual measurements of $p_{w,a}$ is reasonable to assume that the difference between $p_a$ and $p_{w,a}$ decreases linearly with r and is given by $p_a - p_{w,a} = (p_a - p_{w,a})_{r=0}$ (R-r)/R. When the expression for $\Delta F_a$ is integrated on r one finds that $\Delta F_a = 1/3\pi R^2(p_a - p_{w,a})$.

A direct comparison of equation (I.10) with equation (I.1) gives the friction force, $F_f$, acting on the piston. The solid phase force at the bottom of the fiber layer, since it is not moving, can be obtained from static conditions and therefore,

$$F_s = F_f + F_{s,w} - \Delta F_a \qquad (I.11)$$

where $F_s$ is the solid phase force at the top surface of the fiber under dynamic conditions. It should be noted that $F_{s,w}$ now is the force $F_z$ mentioned earlier. The term $\Delta F_a$ corrects for the loss in pressure that is needed in the dynamic compression to drive the air through the fiber layer.

The measurement of the solid phase force and the piston displacement information under dynamic conditions makes a comparison with the static load-deformation curve, friction and $\Delta F_a$ through equation (I.11) feasible. Values of $F_s$ have been normalized by the equilibrium load of $F_{max}$ and values of the displacement by its final deformation $h_{max}$. $\Delta F_a$ is function of time and it reaches its maximum value at the time when $p=p_{max}$ when the ratio $\Delta F_a/F_{max}=0.02$ with $(\Delta p/\Delta z)_{r=0}=0.066p_{max}$. At other times than that corresponding to $p_{max}$, the pressure gradient was set at $(\Delta p/\Delta z)_r=0.066p(t)$ which is an overestimate of the actual pressure gradient. The comparison between the dynamic and static solid forces is shown in figure I.14 where dynamic data for $F_s$ for 4 different loads have been plotted. Due to the piston rebound there is some fluctuation about the final equilibrium values of load and deformation which is reflected as overshoot above the values of the normalized load and displacement. This results in the knotting of the curve at the (1,1) point. All curves indicate large deformations with very small loads which is the major property of the material under testing. At the end of the compression large loads are needed to achieve small changes in deformation. At the beginning of the dynamic compression, the values of $F_s$ remain extremely small in all experiments and it is rather remarkable to observe that as the maximum load decreases the dynamic data of $F_s$ approach the static data of $F_{s,w}$. If the effects of friction are added onto the static deformation data then the resultant $F_s^{'} = F_f + F_{s,w}$ - $\Delta F_a$ can be obtained and compared to the dynamic load data $F_s$. These results are also plotted in figure I.14. The agreement between the measured $F_s$ data and those of reconstructed $F_s^{'}$ appears to be reasonable in the last stages of compression and rather poor in the early and middle stages of compression.

In order to further investigate this disagreement between the dynamic and the reconstructive from static data of the solid phase force $F_s$, the effect of strain rate, $\dot{\varepsilon}_z = d\varepsilon / dt$ on $F_s$ has been explored. It has been reported in the past that high strain rates may affect the characteristics of material behavior and that the applied normal stress depends not only on the deformation $\varepsilon$ but also on the corresponding strain rate, dε/dt, i.e. $\sigma_z = f(\varepsilon, \dot{\varepsilon})$. Yi, Zhu, Zu, & Yi, (2001) reported that strain rate effects in metallic alloy foams start to affect the characteristics of materials at rates of $10^2$ $s^{-1}$ or higher. Strain rate effects have been observed in other cellular materials (polysterene foams) to start at rates of $10^{-2}$ $s^{-1}$ which correspond to quasi-static conditions (Song *et al.* 2006). It has also been found by Yu, Li and Hu (2006) that the onset of strain rate effects starts earlier in lighter cellular materials. Experimentally obtained values of dε/dt for various experiments are plotted in figure I.15 as a function of time. Since the time origin is different in each of the experiments the time lag between various experiments is irrelevant. The data indicate that the peak value of strain rate increases with increasing piston loading and at the maximum load it reaches a value of 4.7 $s^{-1}$. Although this value is not as high as $10^2$ $s^{-1}$ it is not that small to ignore strain rate effects. It has been reported in the literature that these strain rate effects are partly attributed to inertia effects which in the present case of equation (I.11) have been neglected. It is therefore quite plausible that the disagreement between the $F_s$ and $F_s'$ in figure I.14 to be a simple difference between the static and dynamic behavior of the material. Another interesting feature of the response of the material is the observed time-lag between the peak strain rate and peak stress rate which is of the order of 50 ms. If strain rate

effects were absent, the initial static strain-stress relation $\sigma_z = E\varepsilon_z$ will become $\dot{\sigma}_z = E\dot{\varepsilon}_z$ and therefore $\dot{\sigma}_z$ and $\dot{\varepsilon}_z$ should be in phase. However, this is not the case here.

Strain rate effects may well explain the difference between the static and dynamic strain–stress data of figure I.14, particularly at the end of the compression where $\varepsilon_z$ is large, they can not fully explain the close to zero values of $\sigma_z$ at the early and intermediate stages of compression. It is very possible that due to the relative motion of the air and the solid phases in the beginning of compression and at times much before the maximum pressure occurs, the faster moving air drags the fibers with it. This drag force opposes the solid phase force generated by the compression and therefore the measured resultant force may be small. Later the fluid velocity goes down because the flow is trapped and this drag force diminishes.

## I.4 Final remarks

In this Appendix, an experiment has been designed to demonstrate the generation of dynamic lift forces during rapid compaction loading of soft fibrous materials. Several porous materials have been tested and one commercially available material with 95% polyester and 5 % silk composition provided the most promising results.

Novel experimental techniques have been developed capable of measuring the dynamic forces acting on the compressing piston by the air and solid phases of the material. These measurements demonstrated for the first time that excess pore pressure builds up inside the porous material during sudden compression which is large enough to temporarily support huge weights. This is possible because the air

pressure develops much earlier than the solid phase force peaks. This pressure subsequently decays due to air venting into the ambient environment at the edges of the testing apparatus. Significant opportunities for engineering applications arise where heavy weights can be supported by large surfaces under pressure if this venting is substantially reduced or eliminated.

This new concept is being explored in the design of a track which can generate lift forces of the magnitude that would be comparable to the weight of large capacity commercial airborne jet trains (Mirbod *et al.* 2009a, b). The unique features of the track are that the fiber phase contributes insignificantly to the lift, in contrast to skiing or snowboarding where this is typically 50 percent, and its main function is to produce a large aerodynamic resistance for the passage of air out of the confined space containing the porous media due to the presence of impermeable lateral boundaries.

In addition, our work has established detailed characteristics and properties of these materials under dynamic and static conditions. Strain rate effects appear to be present in the dynamic experiments which suggest that a mutual interaction between the solid phase fiber and the air develops which is pronounced in the beginning of the compaction process. By building an instrumented laboratory model we can also investigate the rolling of the AJT.

| Experiment | Load (kg/N) | Applied pressure, $p_w$ (Pa) | $-\Delta h_{max}/h_0$ | $\rho_0$ (kg/m$^3$) |
|---|---|---|---|---|
| Load #5 | 8.95/87.07 | 745 | 90/141=0.64 | 19 |
| Load #4 | 7.6/74.55 | 633 | 86/141=0.60 | 19 |
| Load #3 | 6.25/61.31 | 520 | 79/141=0.56 | 19 |
| Load #2 | 4.9/48.07 | 408 | 71/141=0.50 | 19 |
| Load #1 | 3.55/34.82 | 295 | 66/141=0.46 | 19 |
| Load #0 | 2.2/21.6 | 183 | 25/141=0.18 | 19 |

Table I.1 Load and displacement parameters in dynamic compression experiments.

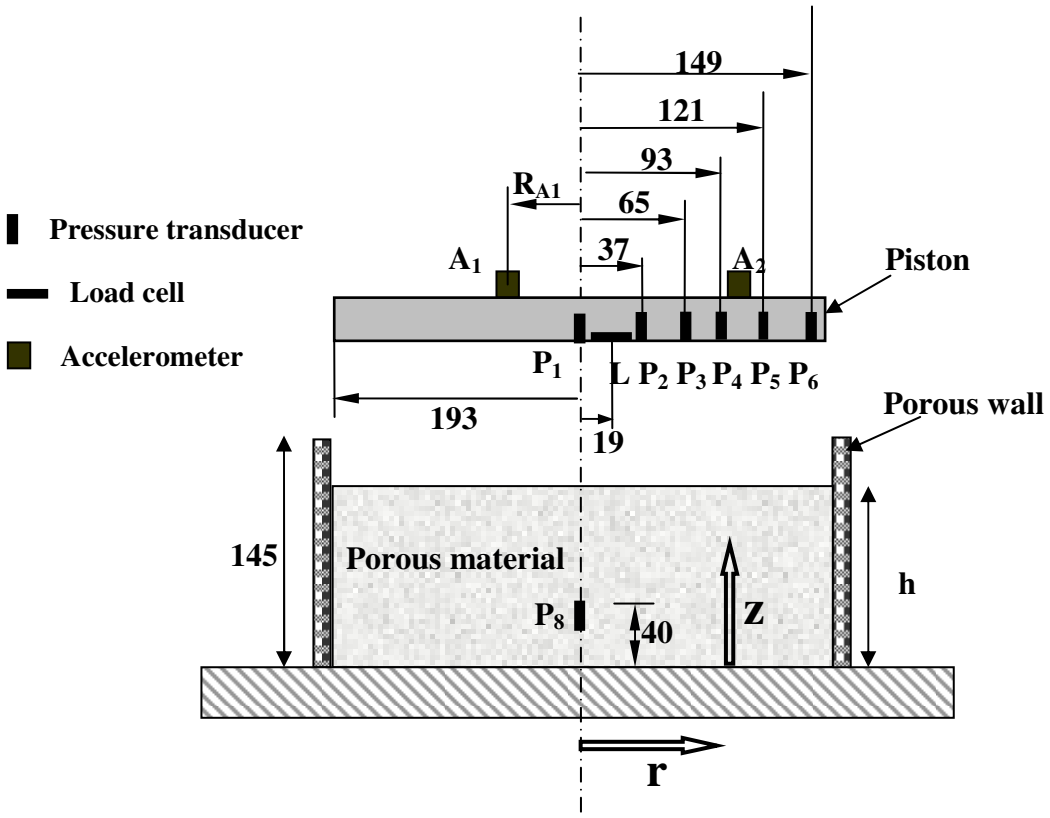


Figure I.1(a) Schematic of piston/cylinder apparatus used for dynamic compression experiments. All dimensions in mm.

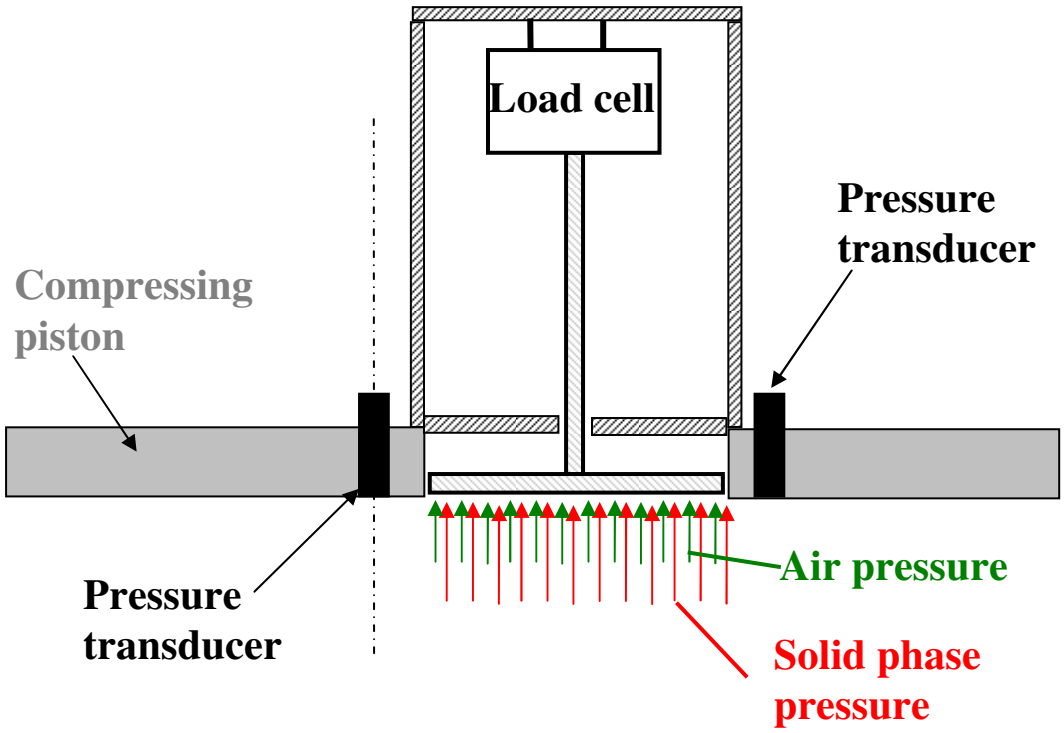


Figure I.1(b) Force measurement system with load cell and pressure transducers.

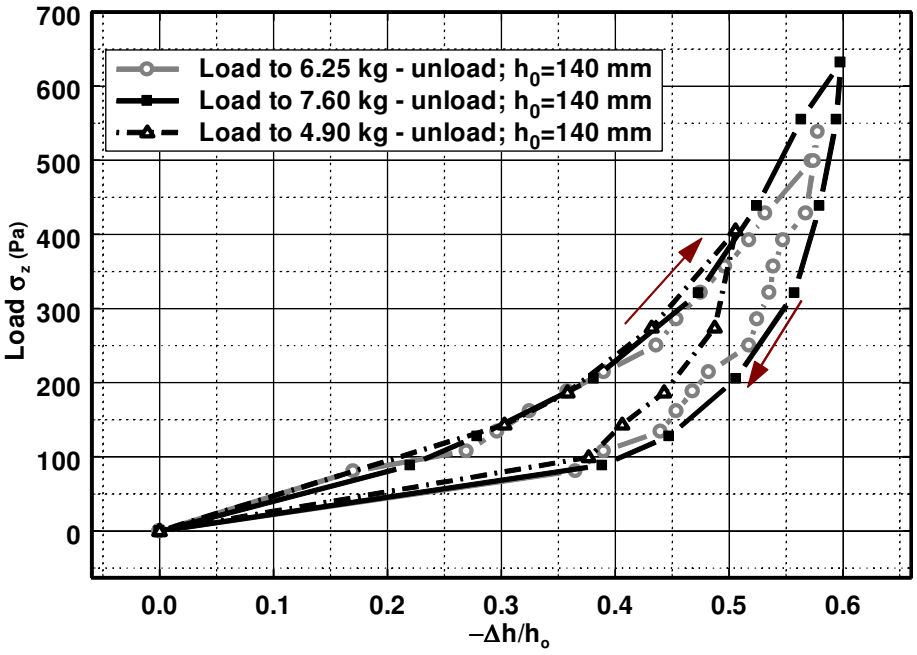


Figure I.2 Typical static load – deformation curves for fiber materials with 95% polyester fibers and 5% silk ($h_0$=141 mm).

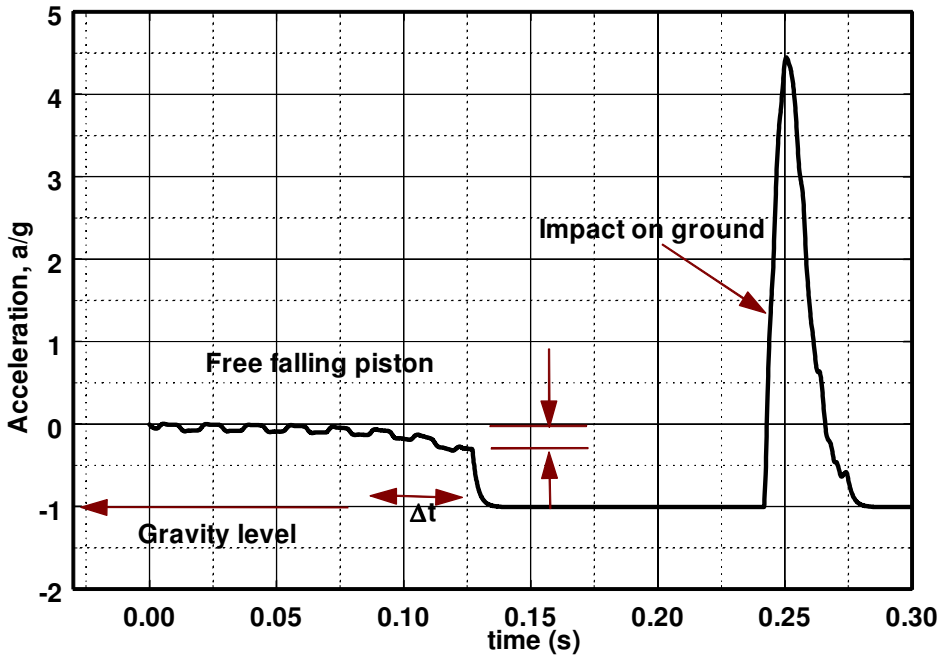


Figure I.3 Accelerometer tests in piston free falling experiments.

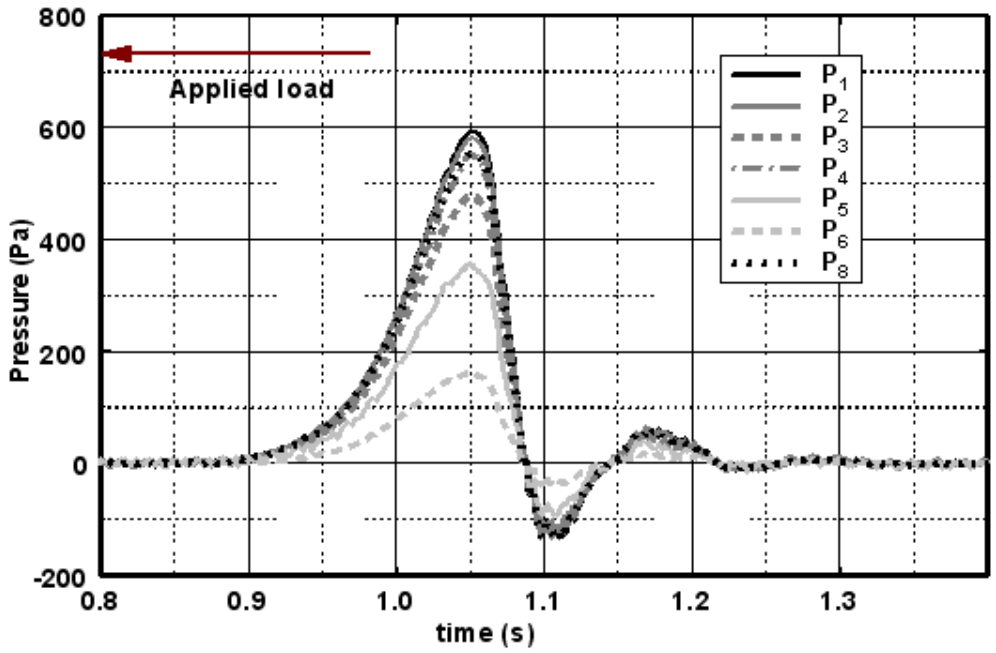


Figure I.4 Time-dependent pressure signals obtain during dynamic compression of fibers at different radial locations on the piston. Case of Load #5. For locations of pressure transducers $P_1$ through $P_8$ see figure I.1.

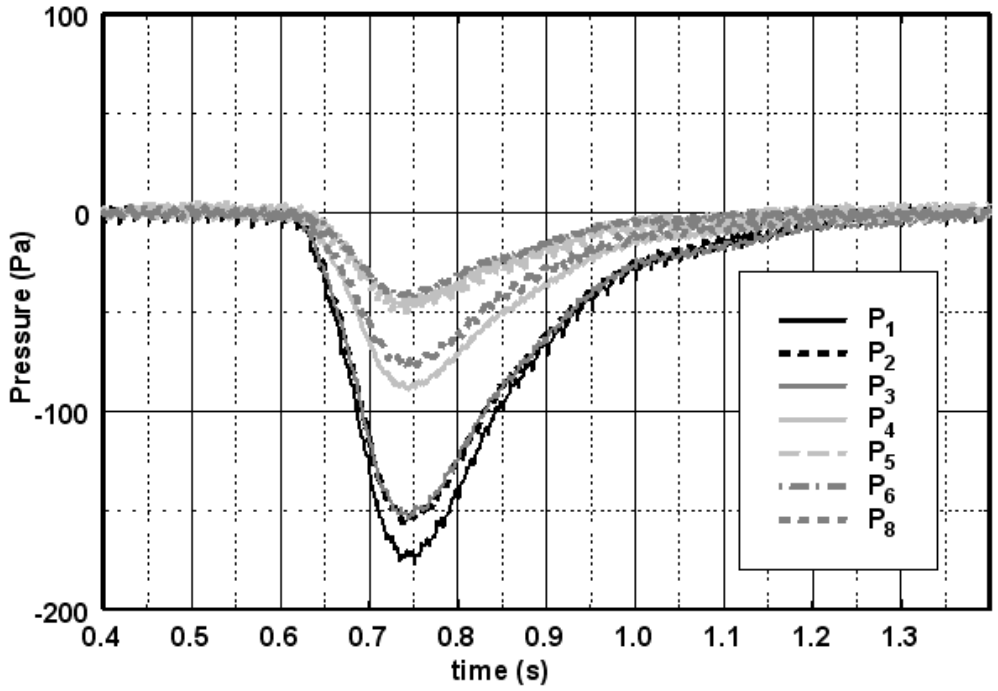


Figure I.5 Time-dependent pressure signals obtain during dynamic unloading and decompression of fibers at different radial locations on the piston. Case of removing Load #5. For locations of pressure transducers $P_1$ through $P_8$ see figure I.1.

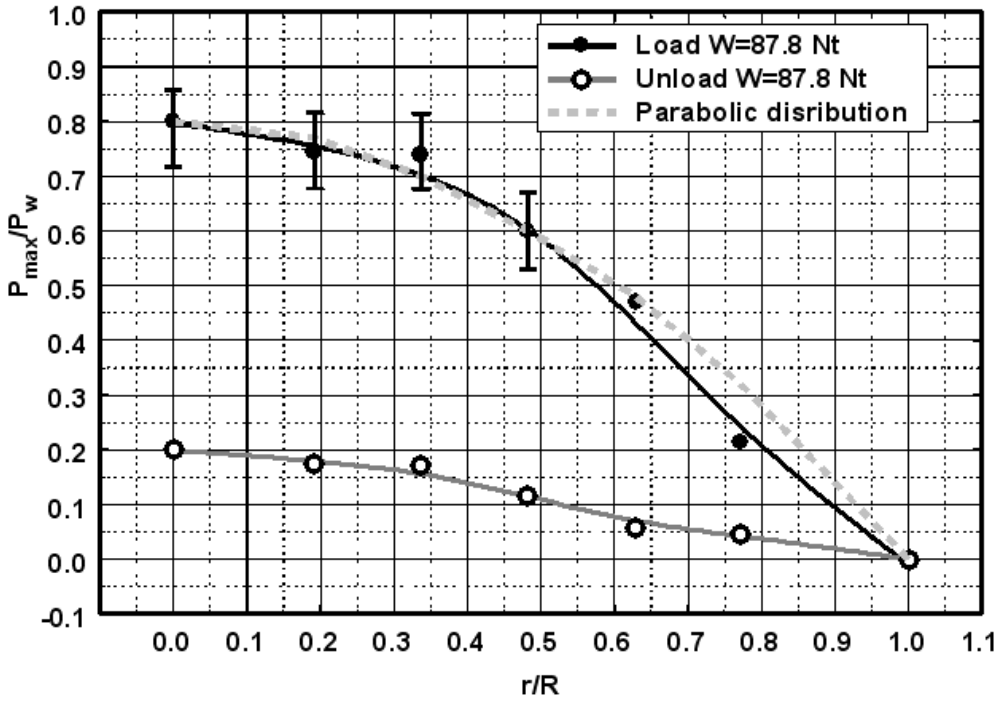


Figure I.6(a) Maximum pressure distribution during loading and unloading of experiment Load #5. Error bars indicate variation in pressure in experiments with piston rotated 90 and 180 degrees.

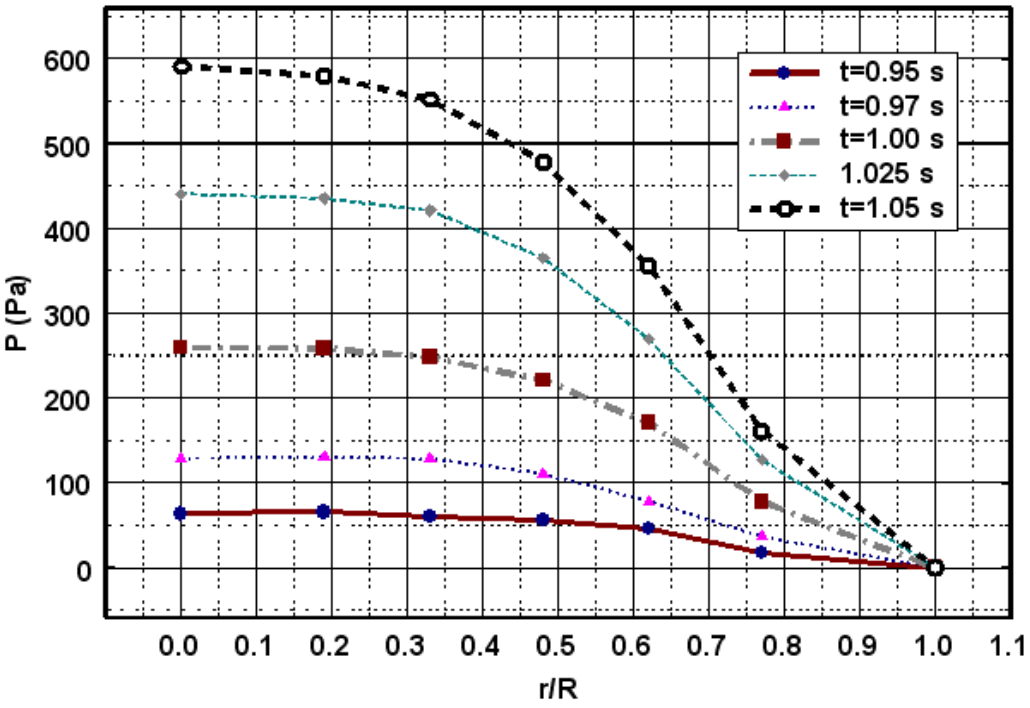


Figure I.6(b) Pressure distribution along radial direction of piston at fixed times.

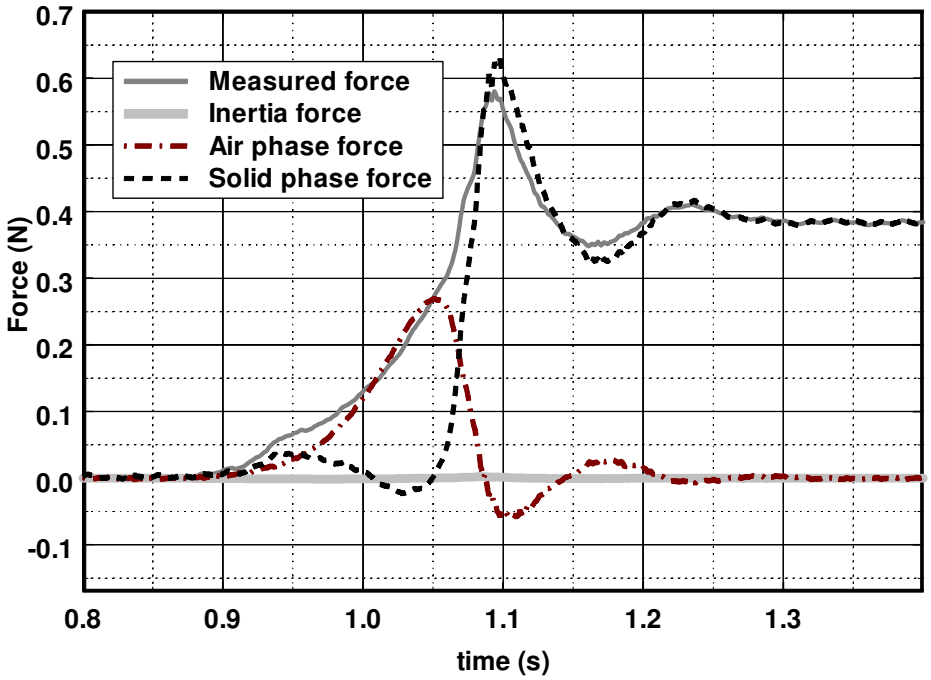


Figure I.7 Time-dependent forces acting on load cell-based force measuring system.

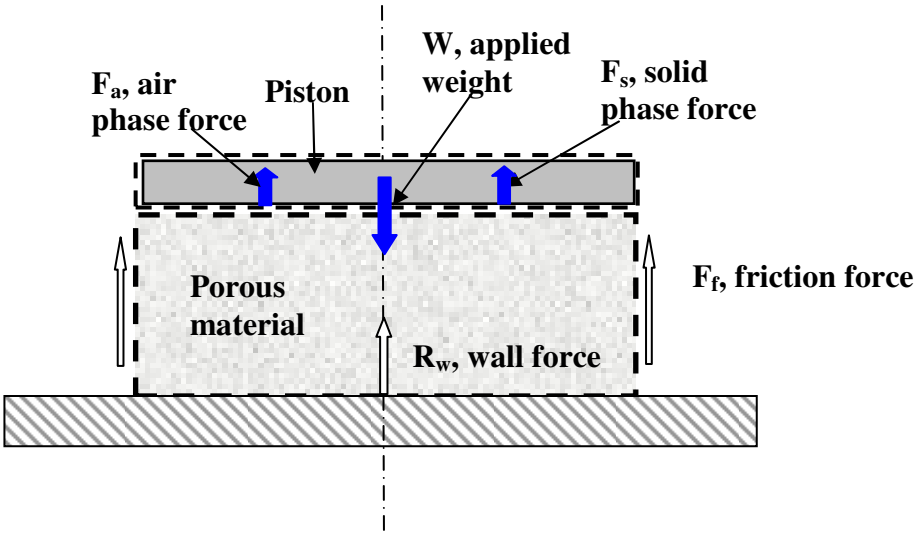


Figure I.8 Forces acting on piston and fiber.

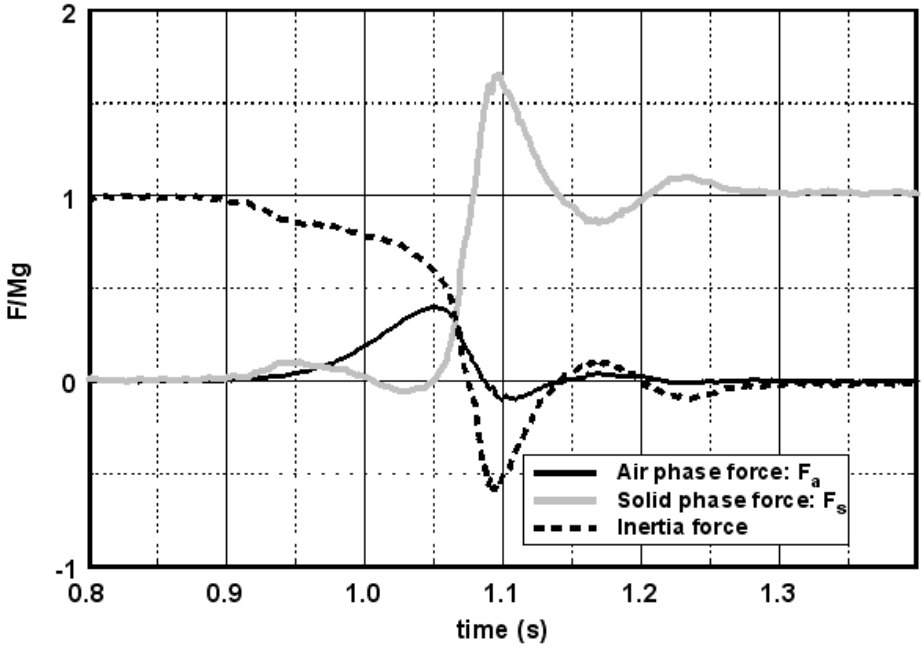


Figure I.9(a) Time-dependent forces acting on piston during dynamic compression. Case, Load #5: Load 87.07 N, which generates a 745Pa pressure; Compression ratio $-\Delta h/h_0=90/141=0.638$; Initial density of fiber material, $\rho_0=19kg/m^3$.

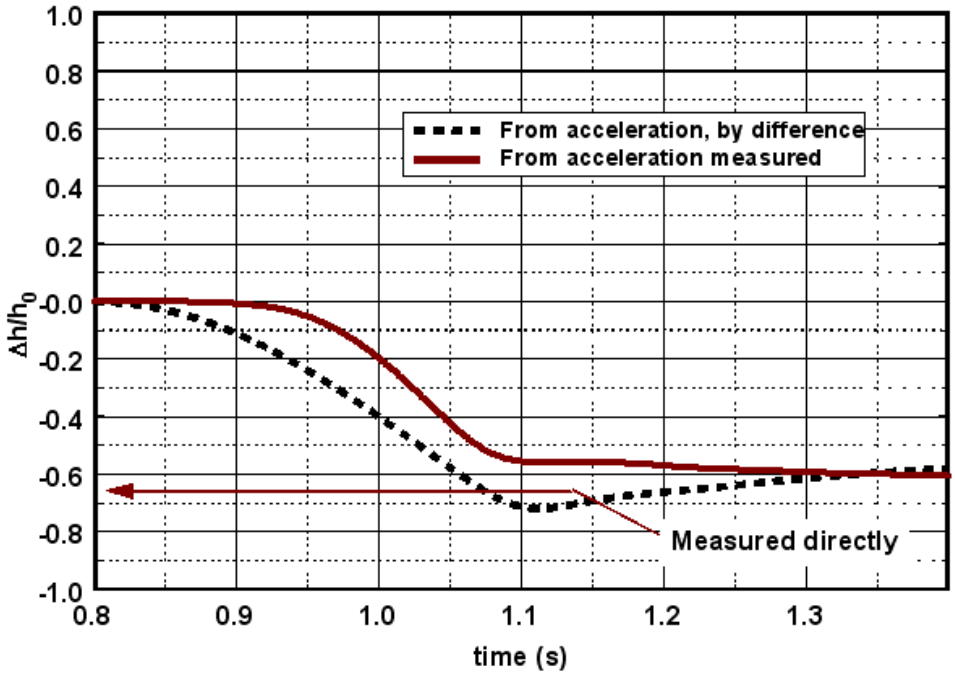


Figure I.9(b) Computed time-dependent displacement of piston during dynamic compression. Case Load #5: Load 87.07 N, which generates a 745Pa pressure; Compression ratio $-\Delta h/h_0=90/141=0.638$; Initial density of fiber material, $\rho_0=19kg/m^3$.

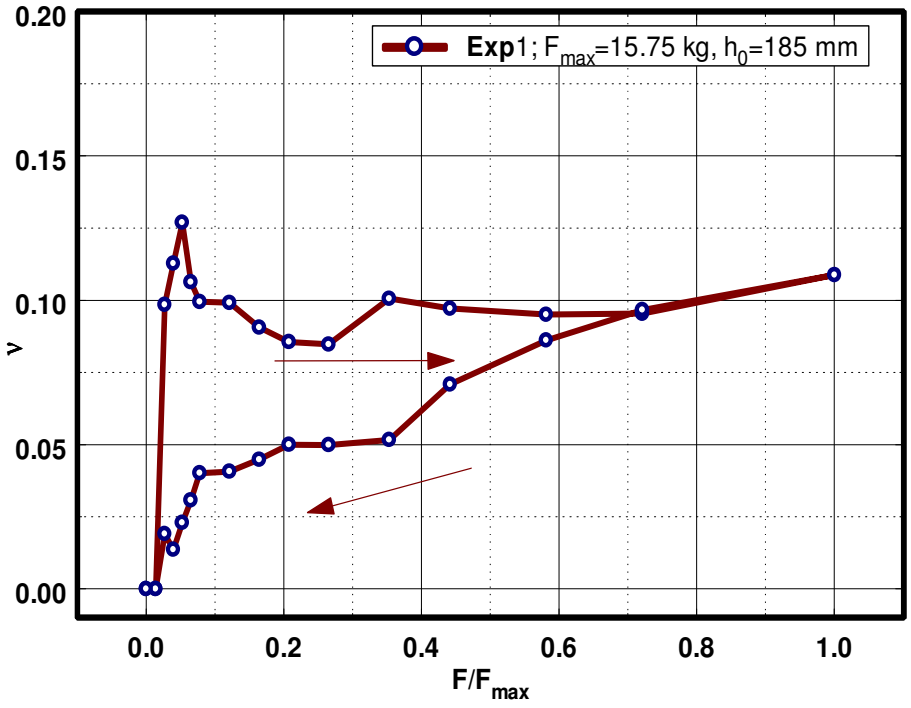


Figure I.10(a) Poisson's ratio versus applied axial stress.

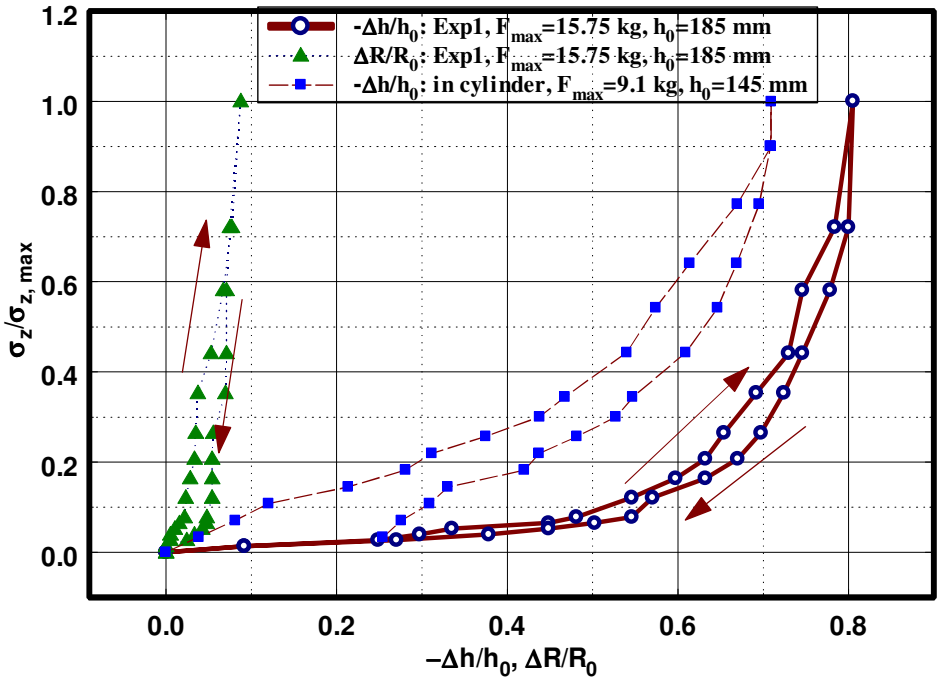


Figure I.10(b) Stress/strains relations.

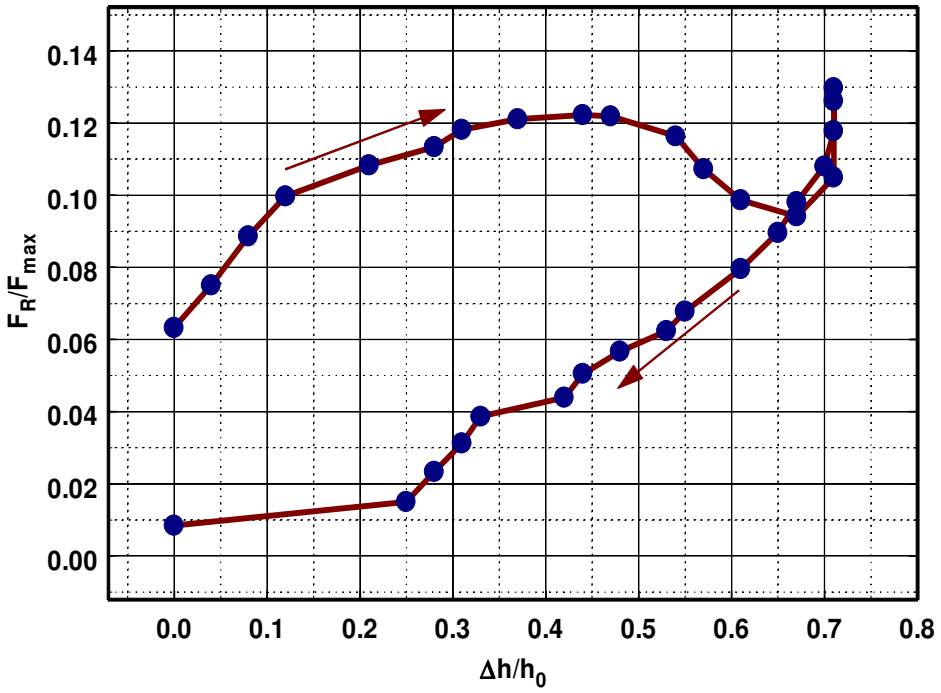


Figure I.11 Static lateral force $F_R$ as a function of compression.

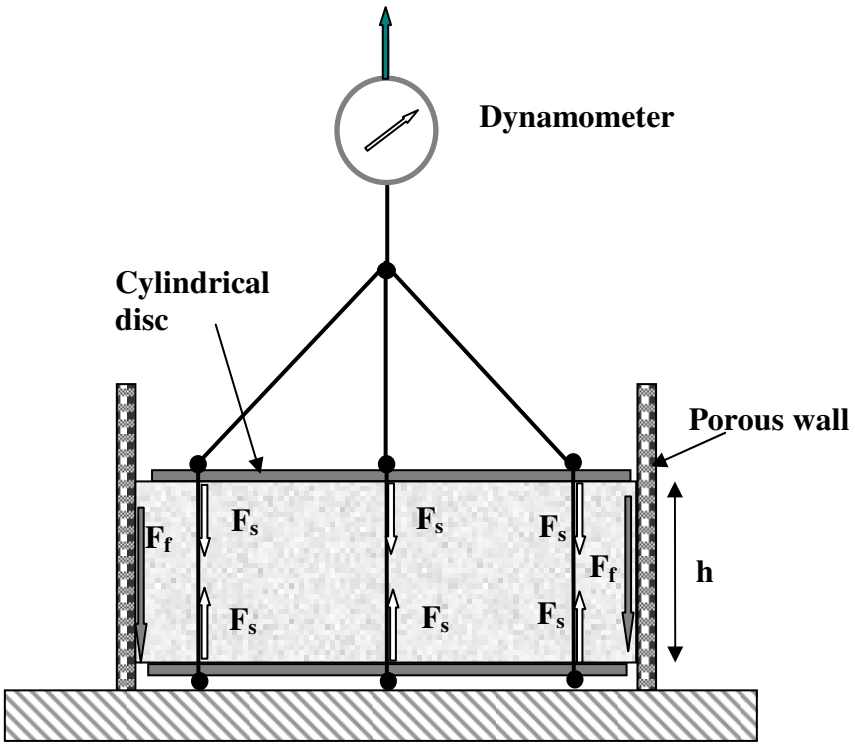


Figure I.12 Experimental setup to estimate friction in cylinder-piston apparatus.

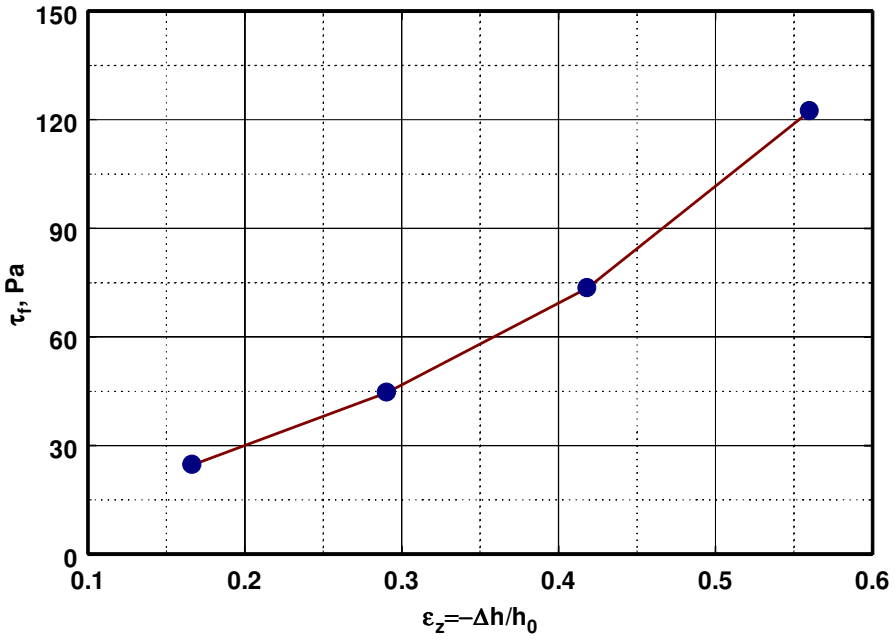


Figure I.13(a) Measured frictional stress as a function of compression.

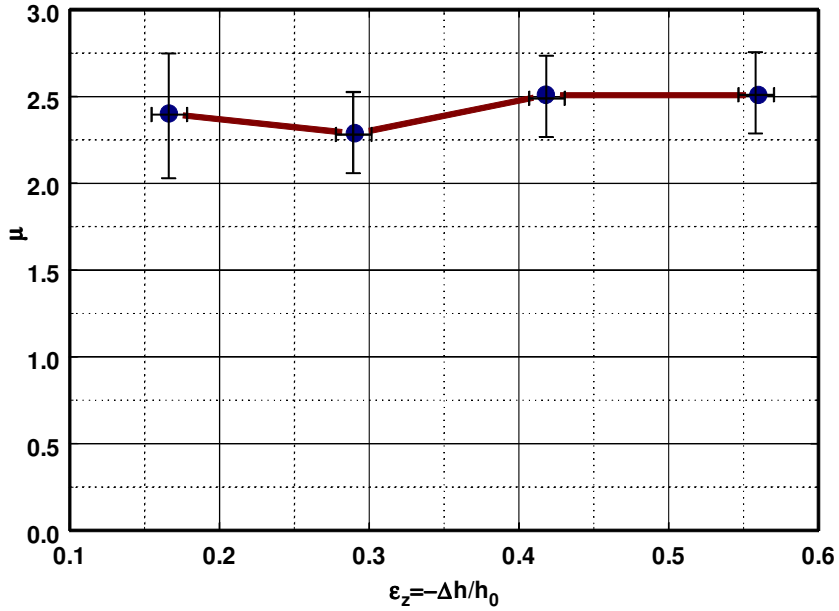


Figure I.13(b) Measured friction coefficient as a function of compression.

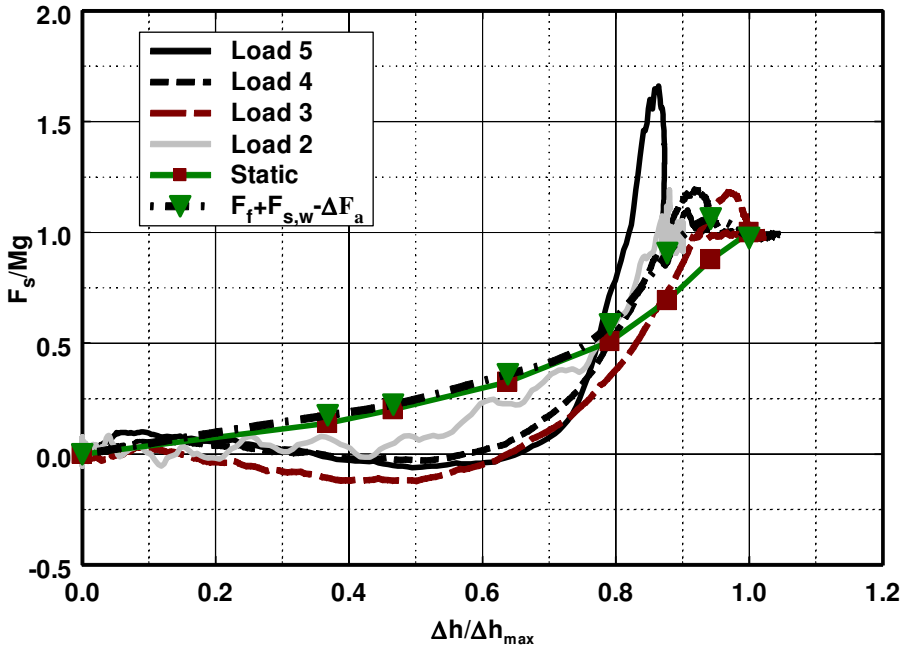


Figure I.14 Comparison between dynamic and reconstructed solid phase forces from static load – deformation curves for fiber materials with 95% polyester fibers and 5% silk.

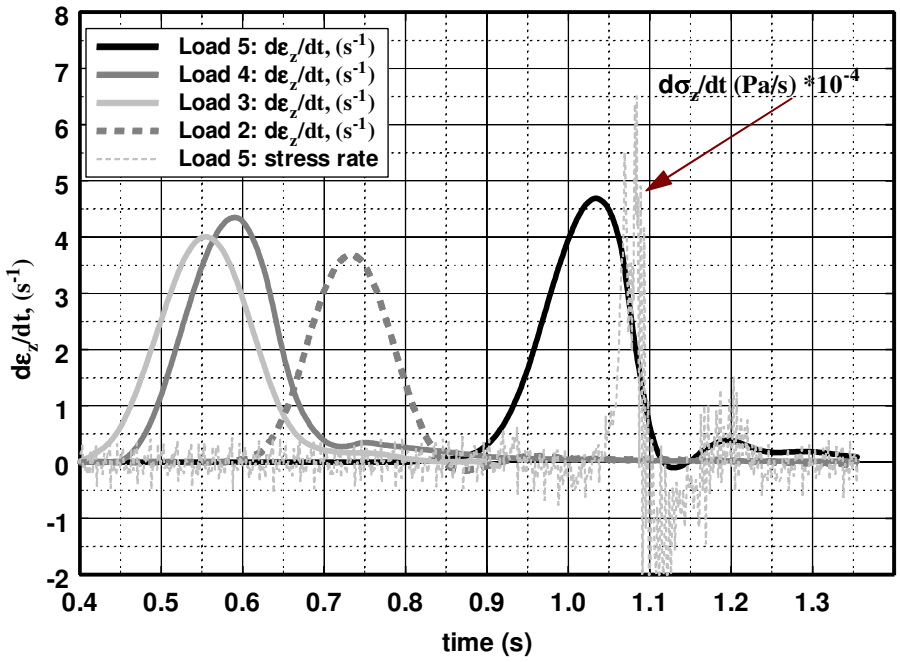


Figure I.15 Strain rates and stress rates as a function of time in various experiments.

# Appendix II. Design of laboratory scale model and experimental results

## II.1 Introduction

A preliminary laboratory experiment has been designed and constructed in our laboratory as illustrated in Fig. II.1 a, b. The length of the track is 250 cm and the model ski slides on the sidewalls of the track. The sidewalls of the channel are impermeable so that there is no lateral leakage and the maximum compression of the soft porous track at the trailing edge is only 1.5 cm in a 8 cm thick layer or compression ratio around 20%. A detailed drawing of the ski which has a lift-off weight, W, of 1 or 2 kg, length, L, of 65cm and four adjustable Teflon pads (dimensions 5 x 3 cm) is shown schematically in Fig. II.2.

Our prototype model utilizes the same porous media, described in chapter 3 for the full scale AJT, where the Darcy permeability $K_p$, is $3.4 \times 10^{-9}$ $m^2$. We performed a parametric study to estimate the primary lift-off velocity $U$ as a function of $k=h_1/h_2$ for this value of $K_p$ and W = 1 or 2 kg. For this purpose, we consider the simpler case where both the variation of $K_p$ with compression and the small lift force due to the fiber phase are neglected in predicting the pressure distribution on the planform. One then integrates this pressure distribution over the surface of the planform and sets F in the expression for the dimensionless force $\mathbf{F} = F K_p(H)/\mu L^2 U w$, equal to the weight W of the prototype model when w is the wide of the ski and L is its length. This solution, which provides an expression for U as a function of k with $K_p(H)= 3.4 \times 10^{-9}$ $m^2$ as a parameter, is shown in Fig. II.3.

We are primarily interested in the portion of the curve in Fig. II.3 where $k<1.25$, similar to the AJT in Fig. 3.6. For primary lift off, we consider $h_1$=8 cm,

$h_2$=6.5 cm or k =$h_1/h_2$=1.23 and $K_p$(H) =3.4x$10^{-9}$ $m^2$, one observes in Fig. II.3 that the initial take-off velocity, U, for a compression ratio of 23% would be, U = 0.92 m/s for W= 1 kg and U= 1.8 m/s for W= 2 kg.

As noted in chapter 3, fibers of different radii can satisfy approximately the same $K_p$ if they have an appropriate solid fraction. The deciding factor is their flexural rigidity. Laboratory tests were performed to measure the local restoring force of the fiber layer as a function of $\Delta h/H$, as shown in Fig. 3.8 in chapter 3. For small compressions, where k is <1.25, the curve is nearly linear. The measured fiber pressure required to achieve a compression ratio of 1.25 in our confined compression in Fig. 3.7 is 25.5 N/$m^2$. The compression of the fibers varies linearly with distance from the trailing edge of the planform, so that the average compression is 0.5 cm and the average pressure beneath the planform is 12.5 N/$m^2$. The area of the planform is 0.1 $m^2$ so that the lift force from the fibers prior to lift off is 1.25 N or about 12.5 percent of the total lift. This lift decreases nearly linearly as the compression at the trailing edge decreases. The maximum friction force on the planform, assuming a coefficient of sliding friction of 0.2, is 0.25 Newton.

In this experiment, we would like to measure the pressure signals of the laboratory model for two different weights of, 1 and 2 kg. For this purpose, two pressure transducers were installed at the wall beneath the track to record the time dependant pressure induced by the passage of the ski as shown in Fig. II.1a.

The ski was pushed downward and forward at the same time by hand under conditions of constant fiber compression at the trailing edge, $h_2$=6.5 cm. The recorded pressure signals shown in Fig. II.4 indicates a peak pressure levels in excess of 300 Pa. These data are the first experimental measurements of the

overpressure produced in our laboratory scale model. The time lag between the two signals is consistently about 0.03 s which suggests that the ski is traveling with a velocity of 6.6 m/s. The two pressure signals drop rapidly after the passage of the ski and then reach negative values during fiber decompression.

The theoretical predicted dimensionless pressure distribution without leakage for k=1.25 is shown in Fig. II.5. Using the pressure profile in Fig. II.5, one can determine the dimensional pressure as a function of time at a given pressure transducer as the planform passes over a particular location which is shown in Fig. II.6 for k=1.25 and two different weights of 1 and 2 kg. One notes that for a weight of 1 kg where the initial velocity, U would be 0.92 m/s for lift off, the maximum pressure is 148.6 $N/m^2$, and for a weight of 2 kg, where U is 1.8 m/s, the maximum pressure would be 290.7 $N/m^2$ which is close to the experimental data that was described in Fig. II.4. This proof of concept paves the way for a more realistic model of the ski-train with a suitable superstructure representing the AJT.

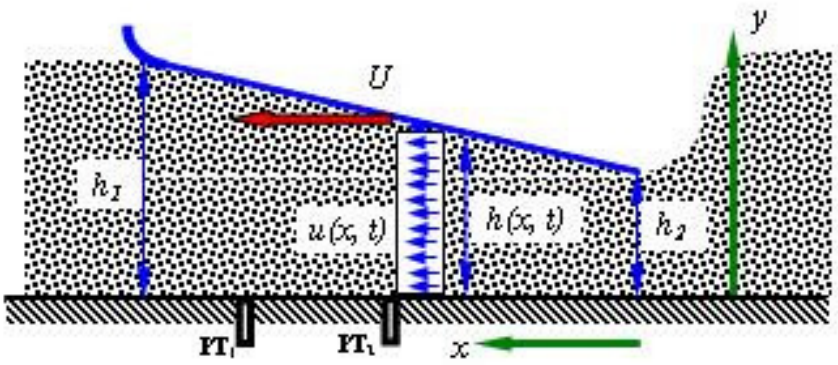


(a)

(b)

Figure II.1 (a) Schematic of an initial laboratory experiment. $PT_1$ and $PT_2$ are the bottom wall pressure transducers. (b) Photograph of the laboratory train track model.

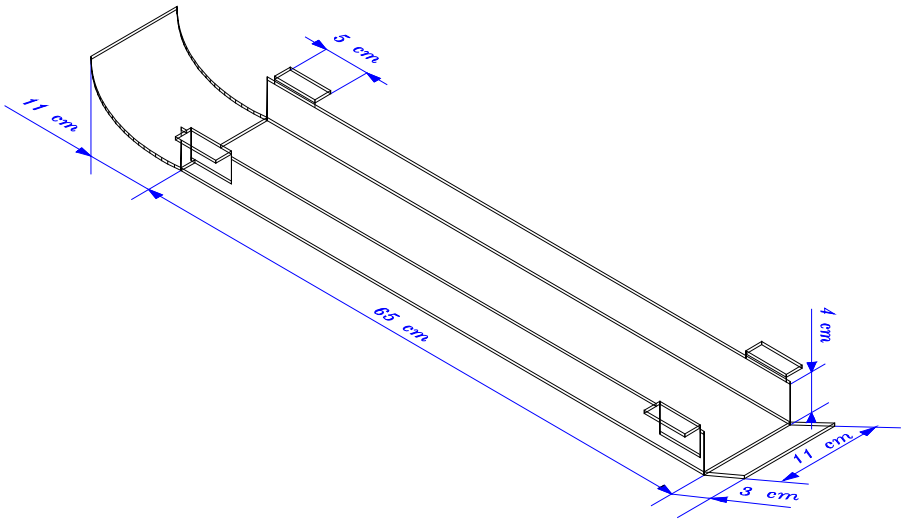


Figure II.2 Drawing of the ski-train model.

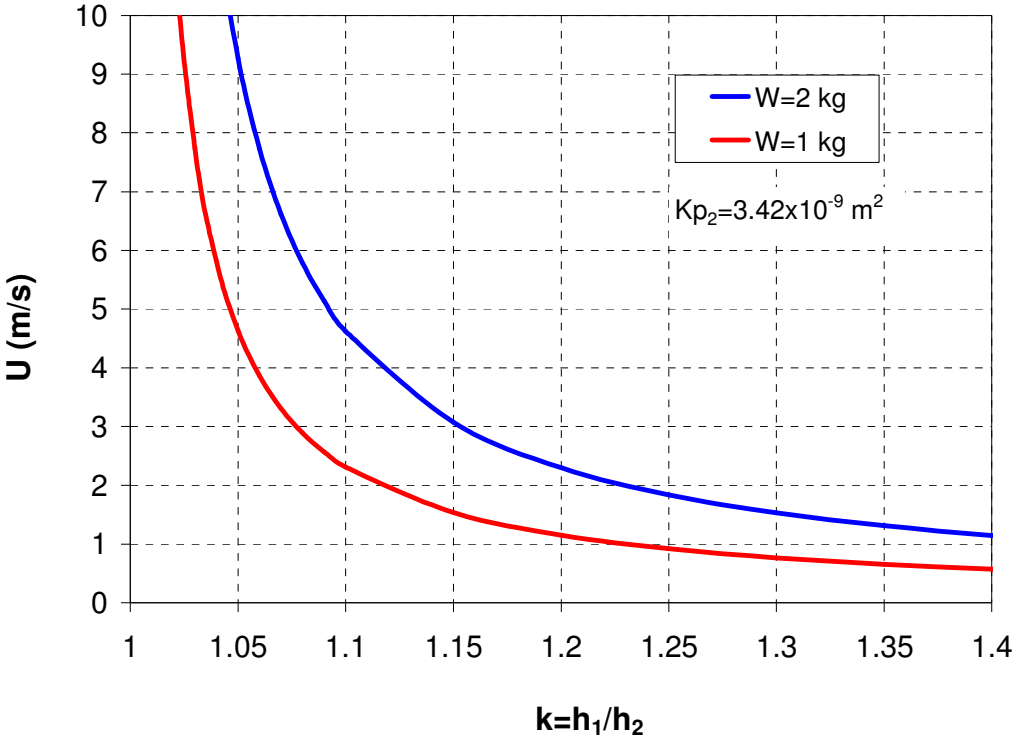


Figure II.3 The velocity U required to support 1 or 2 kg AJT as a function of its planform compression ratio, k.

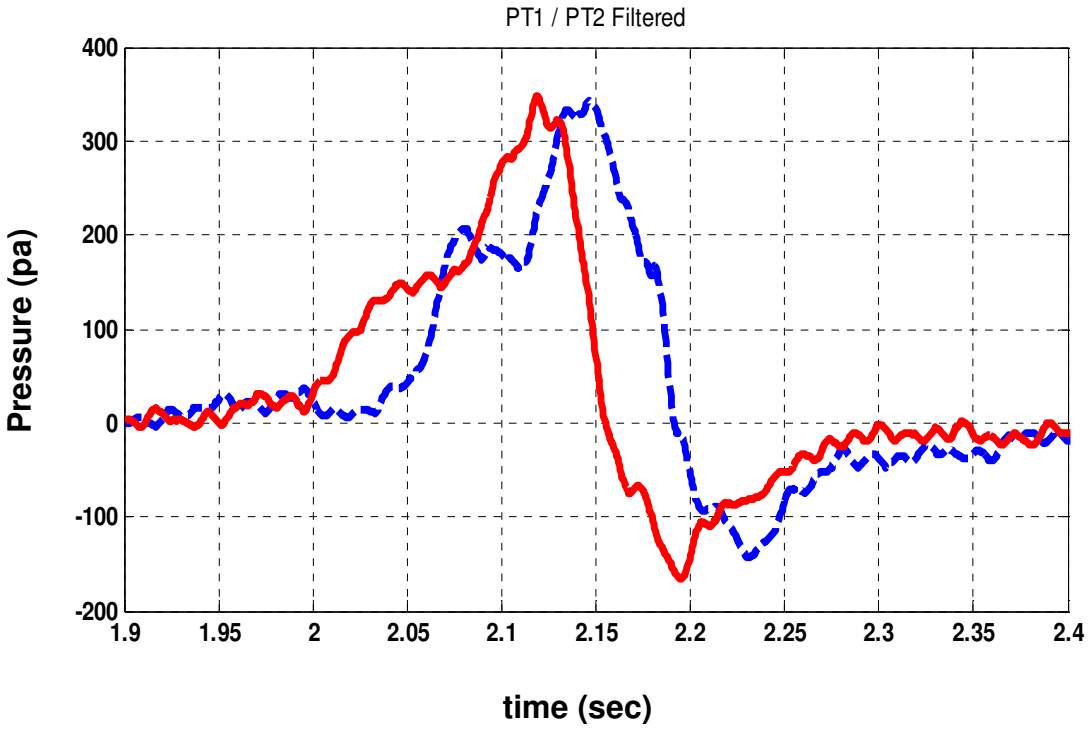


Figure II.4 Signals of pressure obtained by $PT_1$ and $PT_2$ transducers located 20 cm apart in the longitudinal direction.

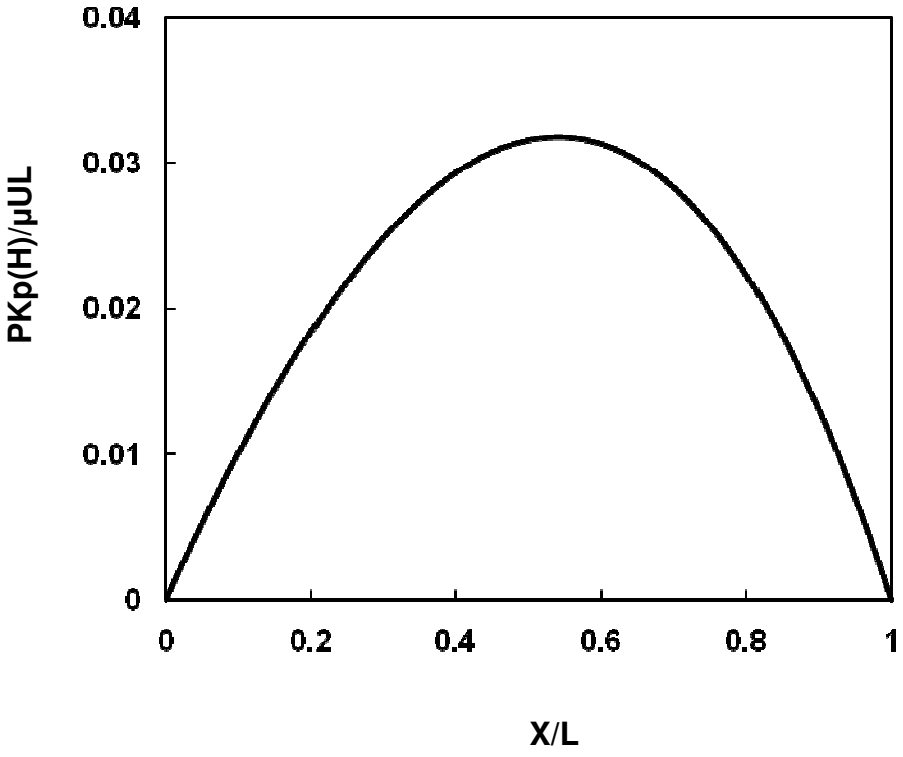


Figure II.5 Dimensionless pressure distribution for k=1.25.

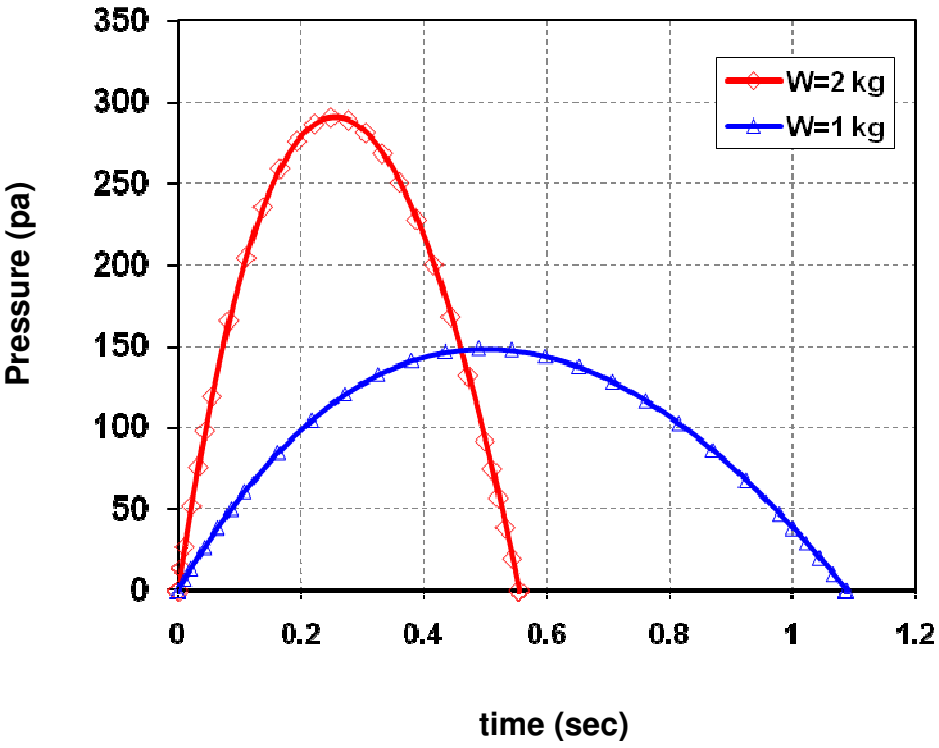


Figure II.6 Predicted pressure signal for two different weights of 1 and 2 kg.

# Appendix III. Programming Part

## III.1 Programming to determine pressure distribution and Kp

```
REAL*8 ALPHA,H,ROU,RF,KP,K,Lf
      INTEGER L,Mt

      OPEN(unit=90, status='unknown',
     1file='Input_EQ.dat')
C     OPEN(unit=98, status='unknown',
C    1file='output_EQ.dat')
      OPEN(22,file='CASE2.txt', status='unknown')


C     ALPHA=0
      X=0
1     L=1.0
C     EPS=0.0000001
C     PRINT*,H1
      Vt=18000
      Mt=116
      ROU=1.39
      RF=0.001
C     L=1.0
      PI=3.1415
      PI=4.0*atan(1.0)

      P0=0.0
      PRINT*,'MOU=',MOU


C    ******************FINDING H(X)***************
      Hold=1.0
      H=0.0
C     K=5
C     H1=H2/K
20    H=H+0.2
C     H=H2-(K-1)/L*H2/K*(L-X)

      PRINT*,'H=',H
      WRITE(22,*)'H=',H
      K=H/Hold
      PRINT*,'COMP RATIO=',K
      WRITE(22,*)'COMPRESSION RATIO=',K

c     PAUSE
C     *****************FINDING Lf*****************

      LF=Mt/(ROU*PI*RF*RF*Vt)
C     PRINT*,'LF=',LF
c     PAUSE
C     *****************FINDING EPS****************
```

```
      EPS=1-PI*RF*RF*LF/(H/Hold)

c     (1-EPS)=PI*RF*RF*LF/(H/H0)
C     PRINT*,PI*RF*RF*LF
      PRINT*,'EPS=',EPS
      WRITE(22,*)'EPS=',EPS
      PRINT*,'1-EPS=',1-EPS
      WRITE(22,*)'1-EPS=',1-EPS
c     PAUSE
      CC=LOG(1-EPS)

C     PRINT*,CC
c     PAUSE
      A=1/(-2*CC-3+4*(1-EPS)-(1-EPS)*(1-EPS))
C     PRINT*,A
C     PAUSE
      B=2/(-LOG(1-EPS)-(1-(1-EPS)*(1-EPS))/(1+(1-EPS)*(1-EPS)))
C     PRINT*,B
C     PAUSE
      G=2*EPS*EPS*EPS/(3*(1-EPS)*(A+B))
C     PRINT*,'G=',G
C     PAUSE
C     PRINT*,'RF=',RF

C    *****************FINDING KP****************

      KP=RF*RF*EPS*EPS*EPS/(4*G*(1-EPS)*(1-EPS))
      PRINT*,'KP=',KP
      WRITE(22,*)'KP=',KP

C     PAUSE
      ALPHA=H/((KP)**0.5)
c     ALPHA=100
      PRINT*,'ALPHA=',ALPHA
      WRITE(22,*)'ALPHA=',ALPHA
c     PAUSE
      C=1/ALPHA
      PRINT*,'C=',C
      WRITE(22,*)'C=',C
      X=0

50    P=ALPHA/H*(X)+101.325*0.0001
      PP=P*(X)*(X)/(1.73*0.000000001*10)
      PRINT*,'X=',X
      PRINT*,'P=',P
      WRITE(22,*)'P=',P
      PRINT*,'PP=',PP
      WRITE(22,*)'PP=',PP

      X=X+0.2
      IF(X.LE.1.1)THEN
      GOTO 50
      ENDIF
c     PAUSE
      IF(H.LE.1.0)THEN
      GOTO 20
c     ELSE
c     Hold=H
```

```
c       GOTO 20
        ENDIF
C       P=ALPHA/H
C       PP=P/(1.73*0.000000001*10)

C       PRINT*,'P=',P
C       WRITE(22,*)'P=',P
C       PRINT*,'PP=',PP
C       WRITE(22,*)'PP=',PP
c       pause

C    *****************FINDING C ****************

C       SUBROUTINE INTEG(F,X)
       IFLAG=1
        EPS1=0.001
        SINTEGOLD=0
        N=10000

2       a1=0
        au=1
        dx=(au-a1)/(N-1)
c      dx=0.2
        sinteg=0
        x=a1
        x=a1-dx
3       x=x+dx
        IF(x.gt.au) goto 4
        call funin(x,Y)
          call funin(x+dx,Y1)
c           call funin(x+2.0*dx,Y2)

        sinteg=sinteg+dx*(y+y1)*0.5

        go to 3

4         continue

        if (iflag.eq.1) then
        sintegold= sinteg

        iflag=0
        dx=dx/2

        goto 2
        end if

        if(abs(sinteg-sintegold).lt.eps1) goto 5

        dx=dx/2
        sintegold= sinteg

5       AA=sinteg
        PRINT*,'AA=',AA
        PAUSE

C       SUBROUTINE INTEG(F,X)
       IFLAG=1
```

```
      EPS1=0.001
      SINTEGOLD=0
      N=10000

22    a1=0
      au=1
c     dx1=(au1-a11)/(N1-1)
      dx=0.2
      sinteg=0
      x=a1
      x=a1-dx
33    x=x+dx
      IF(x.gt.au) goto 44
      call fun(x,YY)
       call fun(x+dx,YY1)
C        call fun(x1+2.0*dx1,YY2)

      sinteg=sinteg+dx*(YY+YY1)*0.5


      go to 33

44      continue

      if (iflag.eq.1) then
      sintegold= sinteg

      iflag=0
      dx=dx/2

      goto 22
      end if


      if(abs(sinteg-sintegold).lt.eps1) goto 55

      dx=dx/2

      sintegold= sinteg

55    BB=sinteg

     PRINT*,'BB=',BB
C     PAUSE

      IF(BB.EQ.0)THEN
      C=0.0
      PRINT*,'C=',C
      ENDIF
C     PAUSE
      C=-(AA)/(BB)
      PRINT*,C
C     PAUSE

C     ****************** PRESSURE DISTRIBUTION**************

C     SUBROUTINE INTEG(F,X)
     IFLAG=1
```

```
      EPS1=0.001
      SINTEGOLD=0
      N=10000

222   a1=0
      M=X
      au=M
C     dx1=(au1-a11)/(N1-1)
      dx=0.2
      sinteg=0
      x=a1
      x=a1-dx
333   x=x+dx
      IF(x.gt.au1) goto 444
      call fun1(x,YYY)
        call fun1(x+dx,YYY1)
C         call fun(x1+2.0*dx1,YY2)

      sinteg=sinteg+dx*(YYY+YYY1)*0.5


      go to 333

444     continue

      if (iflag.eq.1) then
      sintegold= sinteg

      iflag=0
      dx=dx/2

      goto 222
      end if


      if(abs(sinteg-sintegold).lt.eps1) goto 555

      dx=dx/2

      sintegold= sinteg

555   P=sinteg
     PRINT*,'P=',P
      PAUSE


      X=X+0.5
      GOTO 1

      stop
      end


C     ***************SUBROUTINES **************

      subroutine funin(x,y)
      y=(alpha*alpha*cosh(alpha*(2+6*x))-alpha*alpha)/(2*cosh(alpha*
     1  (2+6*x))-2-(2+6*x)*(alpha*sinh(alpha*(2+6*x))))
```

```
      return
      end

      subroutine fun(X,yy)
      yy=alpha*alpha/(H2-(K-1)/L*H2/K*(L-X))
      return
      end

      subroutine fun1(X,YYY)
      YYY=alpha*alpha*(H2-(K-1)/L*H2/K*(L-X)+C)/(H2-(K-1)/L*H2/K*(L-X))
      return
      end
```

## III.2 Programming to determine the Air Force, Solid Force and Velocity U

```
      REAL*4 U,K,h1,h2,Kp2,Fa,W,mou,L,Width,Fs,h0,
     3  La,Lg,Kp1,FR,Ff

      OPEN(22,file='CASE22.txt', status='unknown')

      U=0.0
      Ls=15.0
      L2=20.0
      Lg=10.0
      Mou=1.73*0.00001
h     L=40
      L=30
h     Width=3
      Width=2
h     W=800000
      W=700000
      h0=0.20
      h2=0.20
      h1=0.16
      K=h2/h1
      Dh=h2-h1
      print*,"h1=",h1
      WRITE(22,*)"h1=",h1
      print*,"h2=",h2
      WRITE(22,*)"h2=",h2
      print*,"k=",K
      WRITE(22,*)"k=",K
      print*,"Dh=",Dh
      WRITE(22,*)"Dh=",Dh
c     pause

c     A=3.14*0.0005*0.0005*5949.154*0.1
c     eps=1-((A)/h2)
c     e=1-eps
c     lneps1=1/(-2*log(e)-3+4*e-e*e)
c     lneps2=2/(-log(e)-(1-e*e)/(1+e*e))
```

```
c       Kp2=(3*.0005*.0005)/(8*e*(lneps1+lneps2))*0.0001
c       print*,"Kp2=",Kp2
c       WRITE(22,*)"Kp2=",Kp2

10      Kp2=8*0.0000000001*(h2/h0)**2+3*0.000000001*(h2/h0)-0.0000000001
        print*,"Kp2=",Kp2
        WRITE(22,*)"Kp2=",Kp2


        Kp1=8*0.0000000001*(h1/h0)**2+3*0.000000001*(h1/h0)-0.0000000001
        print*,"Kp1=",Kp1
        WRITE(22,*)"Kp1=",Kp1
c       pause

c       Fa=W
c       Fa=(Mou*L*L*U*Width)/(Kp2*(0.079*log(K)+0.0024))
c       print*,k
c       h2=h1/K
c       print*,h2
c       pause
c       A=3.14*0.0005*0.0005*5949.154*0.1
c       eps=1-((A)/h2)
c       e=1-eps
c       lneps1=1/(-2*log(e)-3+4*e-e*e)
c       lneps2=2/(-log(e)-(1-e*e)/(1+e*e))
c       Kp2=(3*.0005*.0005)/(8*e*(lneps1+lneps2))*0.0001

c        Ps1=117830*(1-(h1)/h0)**5- 133729*(1-(h1)/h0)**4
c   5   + 55751*(1-(h1)/h0)**3- 9584.8*(1-(h1)/h0)**2+
c   6    681.1*(1-(h1)/h0)-1.8904

c       Ps2=117830*(1-(h2)/h0)**5- 133729*(1-(h2)/h0)**4
c   7   + 55751*(1-(h2)/h0)**3- 9584.8*(1-(h2)/h0)**2+
c   8    681.1*(1-(h2)/h0)- 1.8904

        Ps1=152.61*(1-(h1)/h0)-2.0293
        Ps2=152.61*(1-(h2)/h0)-2.0293

        Fs=(Ps1+Ps2)*(L)*width*0.5

        print*,"Ps1=",Ps1
        print*,"Ps2=",Ps2
        print*,"Fs=",Fs
        WRITE(22,*)"Fs=",Fs
c       pause

c       xa=0.0184*(h1/h2)**2.0-0.3668*(h1/h2)+12.4
h       Xa=0.7018*(k)**2.0 - 4.0757*(k) + 23.644
        Xa=0.5263*(k)**2.0 - 3.0568*(k) + 17.733

        print*,"xa=",xa
        WRITE(22,*)"xa=",xa

        La=25.0-Xa
h       La=1.0+Xa-19.0
        print*,"La=",La
        WRITE(22,*)"La=",La
c       pause
```

```
      FFa=-0.0036*k*k+0.0884*k-0.0829
      print*,"AMOUNT FFa=",FFa
      WRITE(22,*) "FFa=",FFa

C     alpha=(h1-h2)/(13.0+L2)
C     print*,"alpha=",alpha

      Fa=(FFa*Mou*L*L*U*width)/kp2
c     U=(Kp2*Fa)/(MOU*(KL1+KL2)*(KL1+KL2)*width*
c    &  (-0.0036*k*k+0.0884*k-0.0829))
      print*,"AMOUNT Fa=",Fa
      WRITE(22,*)"AMOUNT Fa=",Fa

      FR=(Lg*W-Ls*Fs-La*Fa)/L2
Front FR=(W*Lg-Fa*La-Fs*Ls)/L2
      print*,"AMOUNT FR=",FR
      WRITE(22,*) "FR=",FR

c     pause
c     Fa=MOU*L*L*U*width/Kp2*(-0.0036*K*K+0.0884*K-0.0829)
c     print*,"Fa=",Fa
c     WRITE(22,*)"Fa=",Fa
c     pause

      Ff=w-Fs-Fa-FR
Front Ff=W-Fs-Fa-FR
      print*,"amount Ff=",Ff
      WRITE(22,*)"amount Ff=",Ff

c     pause
c     h2=h2+0.0123
c     h1=h1-0.01
      U=U+1.0
      k=k-0.01
c     h2=h1*k
      h1=h2/k
c     K=h2/h1
      Dh=h2-h1

C     L2=(Dh/ALPHA)-LL1
C     KL2=16.0-(KL2*0.0123)
c     KL2=KL2-0.123
      print*,"Dh=",Dh
      WRITE(22,*)"Dh=",Dh
      print*,"h1=",h1
      WRITE(22,*)"h1=",h1
      print*,"h2=",h2
      WRITE(22,*)"h2=",h2


c     pause
      IF(FF<=0.000000001)THEN
      IF(FR<=0.000000001)THEN
c     IF(k<=-2.0)THEN
      GOTO 20
      ENDIF
      endif
```

```
c       endif
        PRINT*,"AMOUNT OF K=",K
        WRITE(22,*)"AMOUNT OF K=",K
        PRINT*,"AMOUNT OF U=",U
        WRITE(22,*)"AMOUNT OF U=",U
        GOTO 10

c20     h2=h2+0.01

c       PRINT*, "***************"
c       WRITE(22,*)"***************"

c       GOTO 5

c       IF(FA<=0.00000001.and.FS<=0.00000001.and.k>10.0)THEN
c       GOTO 33
c       ENDIF
M       PAUSE
m       IF(k<=10.0) then
m       GOTO 5
m       endif

m       PAUSE

c       GOTO 5
20      STOP
        END
```

# Bibliography


1. Adamson, R. H. & Clough, G. 1992 Plasma proteins modify the endothelial cell glycocalyx of frog mesenteric microvessels. J. Physiol. (Lond.) **445**, 473-486.

2. Al-chidiac M., Mirbod P., Andreopoulos Y. and Weinbaum S. 2009 Dynamic compaction of soft compressible porous materials: experiments on air-solid phase interaction. *J. Por. Media,* **12**(11), 1019-1035.

3. Ballinger ML, Nigro J, Frontanilla KV, Dart AM, Little PJ 2004 Regulation of glycosaminoglycan structure and atherogenesis. *Cell Mol. Life Sci.,* **61**, 1296–1306.

4. Biot, M. A., 1941 General theory of three-dimensional consolidation, *J. Appl. Phys*., **12**, 155-164.

5. Biot, M. A. and Willis, D. G. 1957 The elastic coefficients of the theory of consolidation, J. Appl. Mech., **24**, 594-601.

6. Brinkman, H. C. 1947 A calculation of the viscous force exerted by a flowing fluid in a dense swarm of particles. *Appl. Sci. Res*., A 1, 27.

7. Chien, S., Usami, S. & Skalar, R. 1984 Blood flow in small tubes. In Handbook *of Physiology, Circulation. Section on Microcirculation* (edited by E.M. Renkin and C. Michel), pp. 217-249. American Physiological Society.

8. Damiano, E. R. 1998 The effect of the endothelial-cell glycocalyx on the motion of red blood cells through capillaries. *Microvascular Res*., **55**, 77-91.

9. Damiano, E. R. & STACE, T. M. 2002 A mechano-electrochemical model of radial deformation of the capillary *glycocalyx. Biophys., J.* **82**, 1153-1175.

10. Feng, J. & Weinbaum, S. 2000 Lubrication theory in highly compressible porous media: the mechanics of skiing, from red cells to humans. *J. Fluid Mech*., **422**, 288-317.

11. Han, Y., Ganatos, P. & Weinbaum, S. 2005 Transmission of steady and oscillatory fluid shear stress across epithelial and endothelial surface layers. *Phys. Fluids,* **17**, 031508(1-13).

12. Han, Y., Weinbaum, S., Spaan, J. A. E. & Vink, H. 2006 Large-deformation analysis of the elastic recoil of fibre layers in a Brinkman medium with application to the endothelial glycocalyx. J. *Fluid Mech.,* **554**, 217-235.

13. Happel, J. & Brenner, H. 1983 *Low Reynolds number hydrodynamics: with special applications to particulate media* .Springer.

14. Henry, C. B. & Duling, B. R. 1999 Permeation of the luminal capillary glycocalyx is determined by hyaluronan. *Am. J. Physiol.*, **277**, 508-514.

15. Luft, J. H. 1966 Fine structure of capillary and endocapillary layer as revealed by ruthenium red. *Microcirc Symp Fed Proc.*, **25**, 1773-1783.

16. Megens RTA, Reitsma S, Schiffers PHM, Hilgers RHP, De Mey JGR, Slaaf DW, oude Egbrink MGA, van Zandvoort MAMJ 2007 Two-photon microscopy of vital murine elastic and muscular arteries. *J. Vasc. Res.*, **44**, 87–98.

17. Mirbod, P., Andreopoulos, Y. & Weinbaum, S. 2009a On the generation of lift forces in random, soft porous media. *J. Fluid Mech*., **619**, 147-166.

18. Mirbod, P., Andreopoulos, Y. & Weinbaum, S. 2009b An airborne jet train that flies on a soft porous track. *Journal of Porous Media*, **12(11)**, 1037-1052.

19. Nieuwdorp M, Meuwese MC, Vink H, Hoekstra JB, Kastelein JJ, Stroes ES. 2005 The endothelial glycocalyx: a potential barrier between health and vascular disease. *Curr. Opin. Lipidol.*, **16**, 507–511.

20. Pries, A. R., Secomb, T. W. & Gaehtgens, P. 2000 The endothelial surface layer. P*flugers*. *Arch.,* **440**, 653-666.

21. Reitsma S, Slaaf DW, Vink H, van Zandvoort MA, Oude Egbrink MG. 2007 The endothelial glycocalyx: composition, functions, and visualization. *Pflugers Arch,* **454**, 345-359.

22. Roy, B.C. & Damiano, E. R. 2008 On the motion of a porous sphere in a Stokes flow parallel to a planar confining boundary. *J. Fluid Mech*., **606**, 75-104.

23. Sangani, A. S. & Acrivos, A. 1982 Slow flow past periodic arrays of cylinders with application to heat transfer. I*ntl J. Multiphase Flow,* **8,** 193-206.

24. Schlichting, H. 1979 *Boundary layer Theory*, 6th Edn. McGraw-Hill.

25. Secomb, T. W., Hsu, R. & Pries, A. R. 1998 A model for red blood cell motion in glycocalyx-lined capillaries. *Am. J. Physiol.,* **274**, Heart Ciric. Physiol. 43:H1016-1022.

26. Secomb, T. W., Hsu, R. & Pries, A. R. 2001b Motion of red blood cells in a capillary with an endothelial surface layer: effect of flow velocity. *Am. J. Physiol. Heart Circ. Physiol*., **281**, H629-H636.

27. Song, B., Chen, W.W., Dou, S., Winfree, N.A., Kang, J.H. 2005 Computational simulations of the dynamic compaction of porous media International, *J. Impact Engineering,* **31**, 509–521.

28. Terzaghi, K. 1943 *Theoretical Soil Mechanics,* Wiley, New York.

29. Truskey, G. A., Yuan, F. & Katz, D. F. 2004 *Transport phenomena in biological systems,* Prentice Hall.

30. van den Berg BM, Vink H, Spaan JA. 2003 The endothelial glycocalyx protects against myocardial edema. *Circ. Res.,* **92**, 592–594.

31. van den Berg BM, Nieuwdorp M, Stroes ES, Vink H. 2006 Glycocalyx and endothelial(dys) function: from mice to men. *Pharmacol. Rep.,* **58,** *Suppl*., 75-80.

32. van Haaren PM, VanBavel E, Vink H, Spaan JA 2003 Localization of the permeability barrier to solutes in isolated arteries by confocal microscopy. *Am. J. Physiol. Heart Circ. Physiol.*, **285**, H2848–2856.

33. Vink, H. & Duling, B. R. 1996 Identification of distinct luminal domains for macromolecules, erythrocytes and leukocytes within mammalian capillaries. *Circ. Res.,* **71**, 581-589.

34. Weinbaum, S. 1998 1997 Whitaker Distinguished Lecture: models to solve mysteries in biomechanics at the cellular level; a new view of fiber matrix layers. *Ann. Biomedical Eng.*, **26**, 1-17.

35. Weinbaum, S., Zhang, X., Han, Y., Vink, H. & Cowin, S. 2003 Mechanotransduction and flow across the endothelial glycocalyx. *Proc. Natl. Acad. Sci.,* **100**, 7988-7996.

36. Weinbaum, S., Tarbell, J.M. & Damiano, E.R. 2007 The Structure and Function of the Endothelial Glycocalyx Layer. Annu. Rev. Biomed. Eng., **9**, 121-167.

37. Wu, Q., Andreopoulos, Y. & Weinbaum, S. 2004 From red cells to snowboarding: A new concept for a train track. *Physical Review letters,* **93(19)**, 194501-4.

38. Wu, Q., Andreopoulos, Y., Xanthos, S. & Weinbaum, S. 2005 Dynamic compression of highly compressible porous media with application to snow compaction. *Journal of Fluid Mechanics,* **542**, 281-304.

39. Wu, Q., Igci, Y., Andreopoulos, Y. & Weinbaum, S. 2006 Lift mechanics of downhill skiing and snowboarding. *Medicine and Science in sports and Exercises,* **38(6)**, 1132-1146**.**

40. Yu, J.L., Li, J.R. & Hu, S.S. 2006 Strain-rate effect and micro-structural optimization of cellular metals. *Mechanics of Materials,* **38**, 160–170.

41. Yi, F., Zhu, Z., Zu, F., Hu, S. & Yi, P. 2001 Strain rate effects on the compressive property and the energy-absorbing capacity of aluminum alloy foams. *Materials Characterization,* **47**, 417– 422.

42. Zhao, Y., Chien, S. & Weinbaum, S. 2001 *Biophys. J.,* **80**, 1124–1140.